DOT/FAA/TC-16/8

Federal Aviation Administration
William J. Hughes Technical Center
Aviation Research Division
Atlantic City International Airport
New Jersey 08405

Detection and Characterization of Hail Impact Damage in Carbon Fiber Aircraft Structures

September 2017

Final Report

U.S. Department of Transportation
Federal Aviation Administration

NOTICE

Technical Report Documentation Page

1. Report No.	2. Government Accession No.	3. Recipient's Catalog No.
DOT/FAA/TC-16/8		

4. Title and Subtitle	5. Report Date
DETECTION AND CHARACTERIZATION OF HAIL IMPACT DAMAGE IN CARBON FIBER AIRCRAFT STRUCTURES	September 2017
	6. Performing Organization Code ANG-E281
7. Author(s) Stephen O. Neidigk, Dennis P. Roach, Randy L. Duvall, Tom M. Rice	8. Performing Organization Report No.
9. Performing Organization Name and Address Sandia National Laboratories FAA Airworthiness Assurance Center Box 5800 MS-0615 Albuquerque, NM 87185	10. Work Unit No. (TRAIS)
	11. Contract or Grant No. DTFA03-95-X-900002
12. Sponsoring Agency Name and Address U.S. Department of Transportation Federal Aviation Administration 950 L'Enfant Plaza FAA National Headquarters 950 L'Enfant Plaza North, S.W. Washington, DC 20024	13. Type of Report and Period Covered Final Report
	14. Sponsoring Agency Code AFS-300

15. Supplementary Notes

The FAA William J. Hughes Technical Center Aviation Research Division CORs were David Westlund and Dave Galella.

16. Abstract

As the use of advanced composite materials continues to grow in the aviation industry, damage-detection techniques need to be developed and tested. Impact damage on aluminum aircraft structures can be detected from obvious surface indications. This is not the case with composite aircraft structures. Large interply delaminations and substructure disbonding may occur as a result of an impact, often leaving no visual indications of damage. This project investigates the use of various nondestructive inspection techniques to detect hail impact damage in solid laminate aircraft structures ranging from simple flat plate panels to full-scale representative fuselage structures.

17. Key Words	18. Distribution Statement
Nondestructive inspection, Composite, Carbon fiber, Impact damage, Ultrasonic, Delamination, Hail impact	This document is available to the U.S. public through the National Technical Information Service (NTIS), Springfield, Virginia 22161. This document is also available from the Federal Aviation Administration William J. Hughes Technical Center at actlibrary.tc.faa.gov.

19. Security Classif. (of this report)	20. Security Classif. (of this page)	21. No. of Pages	22. Price
Unclassified	Unclassified	149	

ACKNOWLEDGEMENTS

This program is sponsored by the Federal Aviation Administration (FAA) William J. Hughes Technical Center under the direction of the technical monitors, David Westlund and Dave Galella. The approach used in this effort was formulated in concert with the Commercial Aircraft Composite Repair Committee Inspection Task Group. The contributions of this team are gratefully acknowledged.

The authors would like to recognize the data-acquisition support provided by Kirk Rackow and Ciji Nelson at the Sandia Labs Airworthiness Assurance Nondestructive Inspection (NDI) Validation Center. We would like to thank David Westlund and Dave Galella, FAA project managers, and Rusty Jones, an FAA senior technical specialist in NDI and composites, for providing oversight and extensive guidance on this effort.

Additionally, the authors would like to acknowledge Professor Hyonny Kim at the University of California, San Diego and his graduate students—Jennifer Rhymer, Jacqueline Linh Le, and Daniel Whisler—for their significant hail impact testing contributions.

TABLE OF CONTENTS

LIST OF FIGURES

LIST OF TABLES

LIST OF ACRONYMS

CFRP	Carbon fiber reinforced plastic
FBG	Fiber Bragg grating
FO	Fiber optic
FTE	Failure threshold energy
IR	Infrared
LFBT	Low-frequency bond test
LSP	Lightning strike protection
LUS	Laser ultrasonic
MIA	Mechanical impedance analysis
NDI	Nondestructive inspection
OBR	Optical Backscatter Reflectometer
OFDR	Optical Frequency Domain Reflectometry
PA-UT	Phased-array ultrasonic
PE-UT	Pulse-echo ultrasonic
POF	Plastic optical fiber
RDC	Ramp damage check device
SHI	Simulated hail impact
SHM	Structural health monitoring
SWI	Swept wavelength interferometry
TOF	Time of flight
TSR	Thermographic signal reconstruction
TTU	Through-transmission ultrasonic
TWI	Thermal wave imager
UCSD	University of California, San Diego
UT	Ultrasonic

EXECUTIVE SUMMARY

As the use of advanced composite materials continues to grow in the aviation industry, damage detection techniques need to be developed and tested. Impact damage on aluminum aircraft structures can be detected from obvious surface indications. This is not the case with composite aircraft structure. Large interply delaminations and substructure disbonding may occur as a result of an impact, often leaving no visual indications of damage.

This research investigates the use of conventional hand-deployed ultrasonic (UT) inspection techniques and more advanced UT pulse-echo phased-array and resonance-scanning techniques, as well as thermographic laser UT and other methods to detect and characterize damage in solid laminate aircraft structures. It also examines embedded and bonded methods of deploying an in situ fiber optic swept wavelength interferometry strain sensing system for damage detection.

To assess the various methods of nondestructive inspection used in this study, simulated hail impact (SHI) damage was generated on flat plate panels—with severities ranging below the failure threshold energy to barely visible impact damage. The SHI testing was conducted on the panels using a high velocity gas gun with varying diameter ice balls. The ice impact tests were performed in collaboration with the University of California, San Diego. In this study, 81 flat plate panels—which included 8-, 16-, and 24-ply panels—were impact tested. The damage induced included interply delamination, matrix cracking, and some backside fiber breakage.

In addition to the flat plate panels, two fuselage panels representative of structures seen on advanced composite transport category aircraft were fabricated and impact tested. They each measured approximately 56″ x 76″. The structural components consisted of a 16-ply skin, co-cured hat-section stringers, fastened shear ties, and frames. They were fabricated using the same carbon T800 unidirectional carbon pre-preg as the flat plate specimens. In addition to the SHI testing, 2″ diameter spherical tip steel impacts were conducted to simulate impact damage introduced during heavy ground maintenance operations.

The extent of 16-ply skin damage induced on the panels ranged from less than 1 $in.^2$ to 55 $in.^2$ of interply delamination. Substructure damage on the panels included shear tie cracking, delamination of the built-up pad sections behind the fastened shear ties, and stringer-to-flange disbonding. Substructure damage away from the site of high-energy ice impact was often not detected with hand-deployed UT; this can be attributed to failure to inspect far enough away from the impact site. This additional damage was detected using more advanced scanning techniques, including ultrasonic and resonance C-scan.

1. INTRODUCTION

As the use of advanced composite materials continues to grow in the aviation community, methods of damage inspection and detection have become increasingly more important. There is a greater need to understand the response of composite structures to various types of impacts. The typical composite aircraft structure that is vulnerable to an impact event is not a simple, single-element structure. These assemblies often consist of skins, co-cured stiffeners or stringers, fastened shear ties, and frames. Unlike metallic aircraft structures that often dent and deform during an impact event, carbon fiber aircraft structures leave little to no visual indication of damage on the external surface of the aircraft. Depending on the type of impact event experienced by a composite structure, significant widespread substructure damage, interply delamination, and disbonding may occur.

Until recently, the typical inspections used to detect damage in solid laminate composite aircraft structure have primarily consisted of visual inspection and hand-deployed pulse-echo ultrasonic (PE-UT) techniques. Today, more advanced technologies are capable of inspecting large areas and presenting inspection results as two-dimensional images, which minimize the use of single-point measurement signals. This work seeks to assess the use of conventional and advanced nondestructive inspection (NDI) techniques to detect simulated hail damage and steel, spherical-type impact damage in varying thickness flat plates, and full-scale aircraft fuselage composite structures. It also investigates the use of fiber optic (FO) based distributed strain-sensing systems used to detect and locate damage.

To investigate a variety of inspection and damage-detection techniques, as well as assess impact damage characteristics in carbon fiber aircraft structure, eighty-one 12″ x 12″ flat plate panels and two full-scale composite fuselage sections representative of structure seen on advanced transport category aircraft were fabricated. Each of the flat plate panels varied in thickness from 8-ply to 16–24 ply. The full-scale panels measured approximately 56″ x 76″ and consisted of a 16-ply skin, co-cured stringers, fastened shear ties, and frames. Simulated hail impact (SHI) testing was conducted on both the flat plate and large panels using a high-velocity gas gun that shoots ice balls. Damage was mapped onto the surface of the panels using conventional hand-deployed ultrasonic (UT) inspection techniques as well as more advanced UT and resonance scanning techniques. In addition to the SHI testing performed on the panels, 2″ diameter spherical steel tip impacts were conducted on one of the full-scale panels to simulate impact damage introduced during heavy ground maintenance operations. The damage type and extent were characterized and documented at each impact location.

NDI is typically used to inspect for damage based on required scheduled inspections or when an event of concern happens to the aircraft. Aircraft maintenance depots must consider unreported impact damage to an aircraft. For example, a baggage-handling conveyor is bumped into the fuselage near the cargo loading door. In situ damage detection techniques are desirable for impact detection that may occur between scheduled inspections. In addition to the NDI performed on the two full-scale panels, methods of deploying an FO strain detection system were investigated.

1.1 OUTLINE OF THE REPORT

Section 2 of this report begins by providing background information and a literature review on impact damage in composite structures, NDI methods for damage detection in composites, and

strain-sensing techniques using FO. It also discusses the difference between NDI and structural health monitoring (SHM).

Section 3 provides details on the experimental methods and describes the NDI techniques and FO strain-sensing system used in the study. This section also describes the fabrication of the flat plate and two full-scale carbon fiber fuselage panels as well as the methods used to deploy the FO sensors. It also includes details regarding the SHI and spherical tip impact testing performed on the panels.

Section 4 describes the results obtained from hand-deployed UT inspections, UT pulse-echo scanning, and resonance scanning techniques. It also describes how damage characterization was performed using the NDI and details the types of damage associated with ice and steel spherical tip impacts. It then goes on to describe the challenges associated with embedded FO strain sensing and provides results obtained from the multiple FO deployment methods tested.

Finally, sections 5 and 6 detail the conclusions drawn. These conclusions are based on the experimental impact testing conducted and subsequent inspections performed. Recommendations for future work are also discussed.

2. BACKGROUND AND INTRODUCTION

2.1 INTRODUCTION

This section provides a review detailing composite materials and manufacturing practices; impact damage and damage tolerance in composite structures; and an introduction to SHM, NDI, and FO sensing along with their relationship to composite structures. This section begins by providing an overview of composite materials and introduces some of their mechanical properties and failure modes. It continues with a review of work associated with hail-induced impact damage as well as other impact threats and how they relate to aircraft. It then provides an introduction to SHM and discusses the differences between SHM and NDI. Conventional methods of NDI are presented along with applications to composite materials. Finally, methods of using FO for damage sensing are discussed and a history of the technology is reviewed.

2.2 COMPOSITE MATERIALS

Composite materials such as fiber reinforced polymers (FRP) are commonly being used in applications that require low weight and high strength and stiffness. These materials are being used in applications ranging from military and commercial aircraft, satellite, automotive, and civil structures. Composite materials are comprised of multiple materials, each with its own unique structural properties that work together—resulting in a combined material with global properties that are superior to the individual materials of which it is comprised. Advanced FRP materials used in the aircraft industry differ from conventional composite materials in that they are constructed using advanced fiber reinforcements such as Kevlar®, carbon, and high strength treated polymer fiber. Dorworth [1] describes typical applications of advanced composites in the transport industry, including:

- Large components of commercial aircraft, such as the Boeing Company's 777 and 787 Dreamliner and the Airbus A330/340 and A380
- Large primary structures on military aircraft, such as the Airbus A400 and the Boeing C-17 transports, B-2 Spirit Stealth Bomber, and V-22 Osprey tilt-rotor
- Many other components on modern airliners, such as radomes, control surfaces, spoilers, landing gear doors, wind-to-body fairings, and interiors
- Large marine vessels and structures, including military and commercial vessels as well as composite masts
- Primary components on helicopters, including rotor blades and hubs. Composites make 50%–80% of a rotorcraft's airframe by weight

The matrix in a composite laminate acts to bond the structural fibers together, allowing them to share loads applied to the composite. The matrix is typically an epoxy, vinyl ester, or polyester resin system [1], but other resins used to fabricate composites can be seen in table 1. The matrix in an FRP also protects the fibers from moisture ingress, ultraviolet and environmental degradation, abrasion, and impacts. Without the matrix, a composite structure would be nothing more than a sheet of fibers, with little to no shear strength, resisting only tensile loads. Thermoset resins are primarily used for highly loaded structures because of their high strength, availably, and ease of processing compared with other resin systems [2]. When high toughness and/or impact resistance is desired, thermoset resins are commonly used. They are also commonly used in high-volume production applications. Other types of composites can be fabricated using metallic and ceramic matrices, but these are primarily considered in high temperature applications such as brake pads on race cars [3].

Depending on the application for a composite structure, there are many different types of reinforcing fiber that can be integrated into a lay-up. Common fibers include glass, carbon, aramid, polyethylene (PE), polyphenylene benzobisoxazole (PBO), and other ceramic fibers. The Composite Materials Handbook [4] shows other fibers that can be used in composite fabrication. Some of these are listed in table 1.

Table 1. Fiber and matrix materials that can be used for composite fabrication [4]

Fiber Systems	Matrix Materials
Alumina	Bismaleimide
Aramid	Cyanate Ester
Boron	Epoxy
Carbon	Fluorocarbon
D-Glass	Phenolic
E-Glass	Polyamide-Imide
Glass	Polybenzimidazole
Graphite	Polyetheretherketone
Lithium	Polyetherimide
Polyacrylonitrile	Polyethersulfone
Polybenzothiazole	Polyimide
Quartz	Polyphenylene Sulfide
Silicone	Polysulfone
Silicone Carbide	Silicone
S-Glass	Thermoplastic Polyester
Titanium	
Tungsten	

In addition to strength and other mechanical property tailorability, Clemson University is producing and researching cross-sectional-shaped fibers [5]. Similarly, Sang-Yong produced differently shaped cross-sectional carbon fibers prepared from melt-spinning [6]. The mechanical properties of conventional carbon fiber laminates and laminates made using various-shaped fibers were investigated. It was shown that the tensile strength of carbon composites increased as the ratio of fiber perimeter to cross-sectional area increased. It was found that an x-shaped fiber made a composite five times stronger than a composite made with circular fiber. A challenge associated with shaped fiber composites is fully wetting the fiber material with resin and manufacturing the shaped fibers.

2.3 IMPACT DAMAGE IN COMPOSITE MATERIALS

Impact damage can occur on aircraft structures from a variety of different objects. The causes can range from occurrences of low-velocity, high-mass impact caused by baggage-handling vehicles and dropped equipment during maintenance to high-velocity lightweight hail impacts and runway debris. Figure 1 and table 2 show where impact damage can occur on an aircraft during maintenance, what can cause the impact damage, and what level of energy may be imparted to the structure [7]. A significant impact event can occur on the fuselage while heavy equipment is being mounted to the aircraft. Additionally, it can be seen that the range of impact energy which can be delivered to an aircraft from hail can range from 37–95 joules.

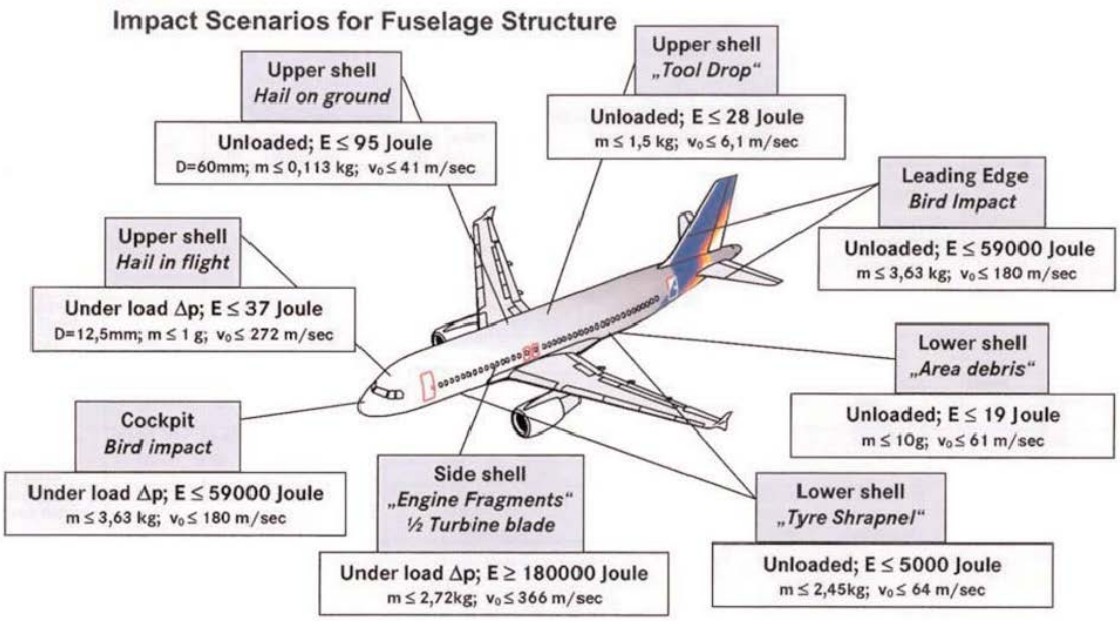

Figure 1. Impact scenarios and energy levels [8]

Impact damage caused by hail has been known to severely cripple a fleet of aircraft. Recently, American Airlines had 80 airplanes removed from service as a result of damage caused by hail in a storm at Dallas Fort Worth Airport [9]. It was reported that more than 100 aircraft were damaged by baseball-sized hail, causing at least 500 flight cancelations [10]. Although baseball-size hail is not a common occurrence, an understanding of the effect and detectability of this type of damage in solid laminate composite structures will assist engineers with estimating what damage will occur to an aircraft in this type of event.

Table 2. Impact threats to aircraft structure [7]

Section/Area		Impact Risk	Energy (J)	ft·lb
Upper Wing Skin: near fuselage		Falling Tools	4	5.4
	(inboard)	Aircraft Lifting Equipment	20	27.1
		Refueling by Gravity	20	27.1
Lower Wing Skin: Outboard		Falling Tools	4	5.4
	Outboard+Inboard	Hail Impact	30–35	40.7–47.4
	Outboard	Loading of Pylons	16	21.7
Rear Fuselage:	Inboard	Runway Debris	12–22	13.2–29.9
	Top	Mounting of:		
		1. Fin	57	77.3
		2. Rudder	10	13.6
		3. Hyd. Reservoir	29	39.3
		4. Hyd. Accumulator	28	38.0
		5. Air Break	6	8.1
		6. Precooler	62	84.1
		Engine Lifting Equipment	44	59.7
		A/C Lifting Equipment	57	77.3
	Sides	Ramming of Service Platform	19	25.8
		Mounting of:		
		1. Hyd. Reservoir	5	6.8
		2. Precooler	11	14.9
		3. Air break	6	8.1
		Engine Lifting Equipment	8	10.8
		A/C Lifting Equipment	20	27.1

The maximum hailstone size that reaches the ground is estimated to average slightly more than 1″ in. diameter in the most severe month of the year, with a 10% chance of exceeding 2″. A 3″ in. diameter hailstone has a 10% probability of reaching the ground at a terminal velocity of around 50 meters per second. For flights at a 10,000–20,000 ft. altitude, over an area of the United States with the most severe hail, there is a 0.1% chance an aircraft will encounter hailstones as large as 1.9″ in diameter in a 100-mile span and 2.4″ in 200 miles [11]. Impact velocity at higher altitudes can reach 200–250 meters per second.

The terminal velocity of a hailstone is dependent on several variables, including the density and size of the hail, the coefficient of drag, and the air density. The terminal fall speed of a sphere is:

$$V = \left(\frac{4g\rho_{hail}D}{3C_d\rho_{air}}\right)^{\frac{1}{2}} \quad (1)$$

where g is the acceleration due to gravity, ρ_{hail} is the density of the hail, D is the size of the hail, C_d is the drag coefficient, and ρ_{air} is the air density. Figure 2 shows the terminal fall speeds of

varying diameter hailstones that were calculated using varying coefficients employed in several different studies [12].

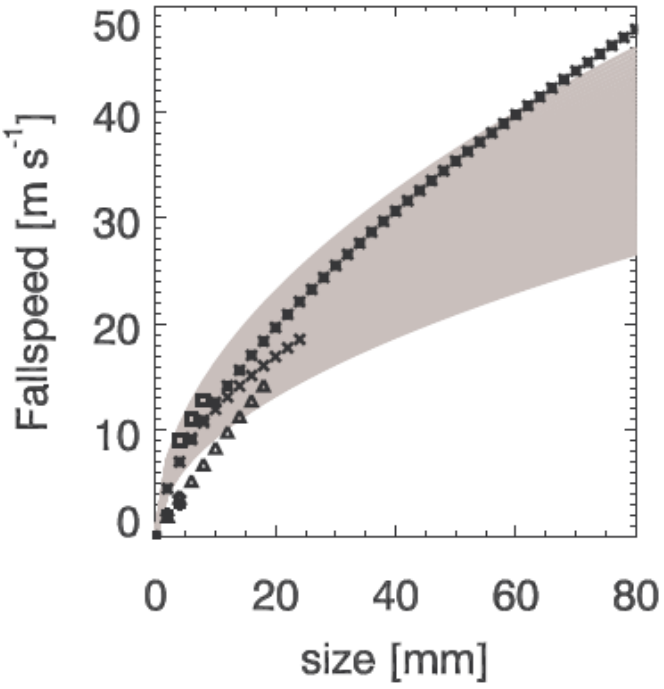

Figure 2. Terminal fall speed of hail

The size and fall speed of a hail ball are not the only considerations that should be taken into account when investigating the damage associated with impact damage. Glancing blows can occur when an aircraft is taking off and landing and can result in significantly higher impact velocities, as described by Field [12].

> In general terms, aircraft that are stationary on the ground are subject to perpendicular hail impacts from above, whereas, for aircraft in flight, higher velocity impacts usually occur to forward-facing structures, such as the nose and wing leading edges while the top skins experience relatively low-impact velocities. If only the velocity vectors are considered, then the worst case is normal impact to the front-facing sections of the aircraft during horizontal flight when aircraft speeds reach their maximum because the vertical component from falling hailstones is comparatively minor. Primarily because of stringent bird strike requirements, these forward-facing structures are tough and research has shown them to be sufficiently damage-tolerant to hail impact. However, if an aircraft starts to climb at an angle during a hailstorm, then the vertical component of the aircraft velocity begins to contribute more to the hail impact velocity (ignoring the effects of up and down draughts). Glancing impacts have been found to act as normal impacts with an effective velocity equal to the normal component of the projectile's true velocity (Kim, 2003). Most in-flight impacts are of a glancing nature. There may be a possibility that an aircraft that is climbing may be subject to more severe hail impact loads, particularly when considering the upper wing skins, which generally are not

required to be as damage-tolerant as the lower wing surfaces. This could give rise to an impact velocity of approximately 200ms-1 on the top skins, which would clearly result in severe damage.

When a foreign object impacts a composite structure, several damage modes can occur, including delaminations, disbonds, fiber breakage, matrix cracking, and several other mixed-failure modes. The damage mode that is most prevalent depends on the parameters of the impactor and the material properties of the composite [13]. Composites made with fiberglass or carbon are more susceptible to damage during impact because of their brittle characteristics, as opposed to Kevlar®, which can absorb significant amounts of energy [13].

Damage resulting from impact in composite materials consists of multiple fracture modes which combine to produce a complex three-dimensional pattern. Experiments indicate the existence of a failure threshold energy (FTE), which is the impact energy level at which damage is first produced in a composite laminate. Impacts below this energy threshold do not produce damage. Impacts above the FTE level produce matrix cracks generated by shear or tensile flexural stresses around the indentation area. They develop mainly in the intermediate and back face layers [14]. Matrix cracks are then followed by interface delaminations growing from the crack tips. Delaminations occur between plies of different orientations and are elongated along the fiber direction of the lower layer interface, with the largest delaminations developing between layers with the highest orientation mismatch. As impact energy is increased, superficial fiber fractures initiate at the tensile side of the impacted sample and may propagate through the remaining layers, leading to total perforation of the laminate [14].

Impact damage of high-velocity hail on woven carbon/epoxy composites was studied by Kim [15]. Spherical, simulated hail balls were created using a spherical split mold. They were fired from a high-velocity gas gun, at speeds ranging from 30–200 m/s and varying angles of 90, 45, and 20 degrees, at carbon composite plates held in an aluminum picture-frame fixture. Numerous panels were tested and some were tested multiple times following a no-damage test result. It was found that the FTE of composites scaled linearly with the panel thickness. It was also found that small-diameter simulated hail produced a lower FTE than larger simulated diameter hail because of the more localized impact area. A damage mode progression for high-velocity ice impact was provided by Kim and can be seen in figure 3. The figures show that internal damage (not visual) can be caused by much lower impact velocity and be more severe than damage created at much higher impact velocity that penetrates the structure.

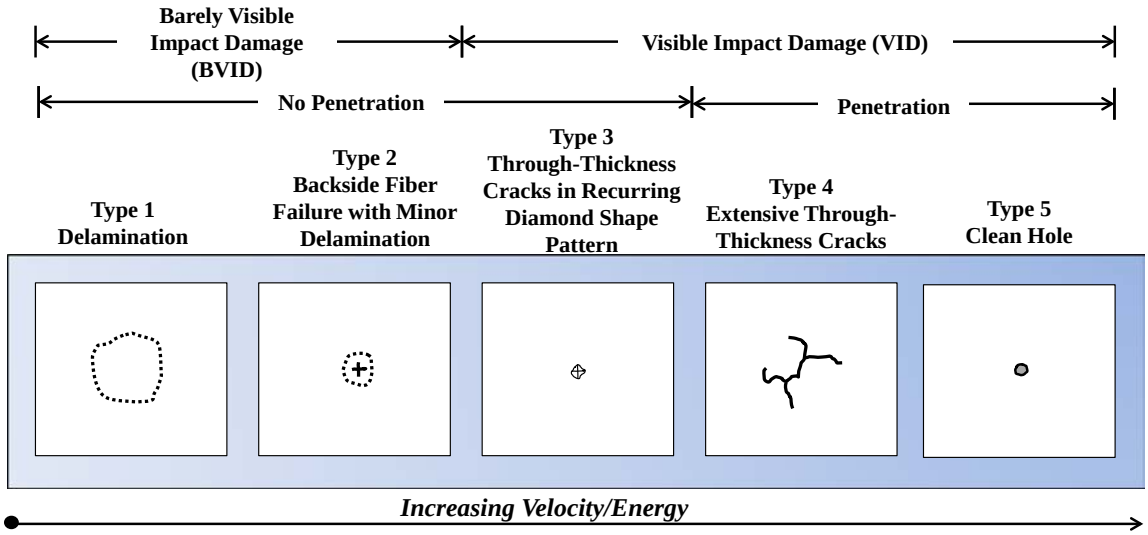

Figure 3. Damage mode progression for high-velocity ice impacts [15]

More recently, Rhymer determined the FTE of 12″ x 12″ square composite laminates fabricated using T800/3900-2 carbon/epoxy pre-preg tape instead of woven fabric [16]. The study employed a high-velocity gas gun and used three different diameter ice balls (38.1, 50.8, and 61.0 mm.) as well as three different thicknesses of composite panels. Table 3 shows the FTE values for 8-, 16-, and 24-ply laminates. To determine the FTE, a panel was first impacted at an energy level where no damage was expected. The specimen was then inspected in situ with a UT inspection method—and, if no damage was detected, the panel was impacted a second time at a higher energy level at which damage may occur. If no damage was detected, the process was repeated, increasing the energy by roughly 10% each time. The impact energy was calculated using the mass of the simulated hail and velocity measured just before impact using equation 1.

$$\boldsymbol{E = \frac{1}{2} m v^2} \tag{2}$$

A comparison of the data was performed using woven fabrics, with similar results [15, 16]. This showed that the failure threshold of the two materials was almost the same.

Table 3. The SHI FTE on T800 carbon tape panels

Panel Type (Thickness)	Ice Ball Diameter (mm)	Mean FTE Value (J)	FTE Value (10% threshold) (J)	FTE Value (10% threshold) (m/s)
8-Ply (1.59 mm)	38.1	211	172	115
	50.8	259	258	91
	61	226	223	65
16-Ply (3.11 mm)	38.1	369	311	154
	50.8	456	456	121
	61	507	489	96
24-Ply (4.66 mm)	38.1	415	413	178
	50.8	736	733	154
	61	938	865	127

2.4 DAMAGE TOLERANCE OF COMPOSITE STRUCTURES

As defined by the FAA in its Advisory Circular 25.571-1D [17] for transport aircraft, damage tolerance is: “The attribute of the structure that permits it to retain its required structural strength for a period of use after the structure has sustained a given level of fatigue, corrosion, or accidental or discrete source damage.” It is the ability of an aircraft structure to sustain damage, without catastrophic failure, until such time that the component can be repaired or replaced.

The effect of impact damage on the strength of composite structures, also known as damage tolerance, has been extensively studied. It was shown that impact damage ranging in size from 200 mm^2–300 mm^2 in 3 mm thick carbon fiber reinforced plastic (CFRP) panels (approximately 16 plies of uniaxial tape) decreases the strength of the laminate by approximately 30% in compression loading [18] applications. Typically, the larger the damage size in a composite structure, the more significant the decrease in ultimate strength and durability of the structure.

Detectable damage size and damage-tolerant design go hand-in-hand. A critical flaw that significantly decreases the strength of a structure should be within the detectable limits of the inspection technology being used. Alternatively, the damage tolerance of the structure needs to be increased so that the damage of concern can be reliably detected by NDI methods. The relationship between damage detectability and accidental impact energy can be seen in figure 4 [19]. Damage falling in Zone 1 is undetectable, lower-energy damage and the component must be able to withstand ultimate load for the life of the structure. Damage falling in Zone 2 is detectable at scheduled inspection intervals and must be able to withstand the design limit load (considered ultimate). Damage in Zone 3 is undetectable, higher-energy damage, such as blunt ground vehicle impact.

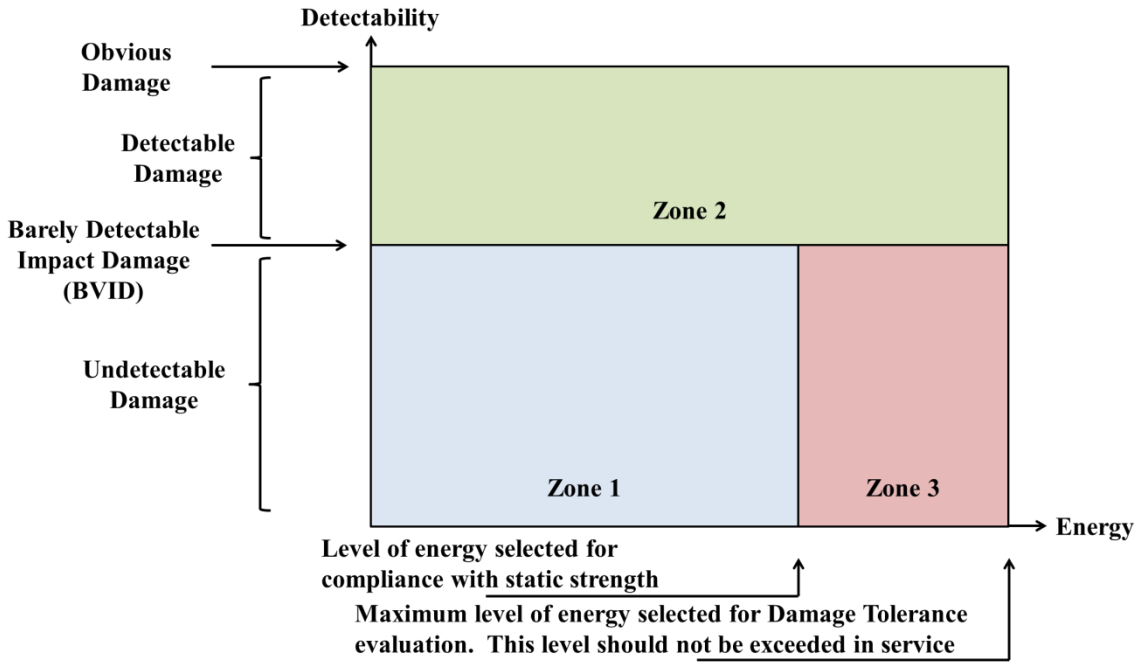

Figure 4. Damage-tolerant design [19]

2.5 SHM – INTRODUCTION

SHM, which is often closely associated with NDI, but uses in situ sensors instead of human-deployed inspection devices, has been defined in a wide variety of ways. A definition of NDI is provided below along with a definition of SHM to provide a basis of comparison.

NDI is the examination of a material to determine geometry, damage, or composition by using technology that does not affect its future usefulness. It involves the following:

- A high degree of human interaction
- Local, focused inspections
- Requires access to area of interest
- Is applied at select intervals

The use of in situ sensors for real-time health monitoring of aircraft structures can be a viable option to overcome inspection impediments stemming from accessibility limitations, complex geometries, and the location and depth of hidden damage.

SHM is the use of in situ, mounted, or embedded sensors and analysis to aid in the assessment of structural or mechanical condition or system operation, including the direct detection of structural flaws. Parameters to be monitored could indicate flaws directly or could be physical properties, such as load, strain, pressure, vibration, or temperature from which damage,

malfunction, mechanical problems, or the need for additional investigation can be inferred [20]. Potential benefits that SHM offers regarding aircraft maintenance and operation include:

- Reduction of inspection time
- Early flaw detection to enhance safety and allow for less drastic and less costly repairs
- Overcoming impediments associated with accessibility limitations, complex geometries, and the depth of hidden damage
- Ensuring safety by identifying problems (aircraft operations, diminished structural integrity) that could threaten airworthiness
- Minimized human factors concerns due to automated, uniform deployment of SHM sensors and automated data analysis

Fiber-based composites have been a desirable application for SHM because of the need for wide-area monitoring and the unique range of failure modes associated with composite structures, including delamination, fiber fracture, matrix cracking, and environmental degradation. Moreover, fiber-based composite structures are primary candidates for embedded sensors because they are laid up using multiple plies of fiber material and then infused or pre-impregnated with resin.

2.6 NDI OF COMPOSITE STRUCTURES

Damage assessment in aircraft composite structures is critical to ensure their safe operation. The size and location of damage must be accurately determined to decide the type and size of repair that needs to be performed. If the size of damage is overestimated, the amount of the material removed from the structure may exceed what is necessary. Visual inspection is typically the first and most rapid type of inspection performed after a suspected impact. The smallest damage size likely to be found visually is discussed by Armstrong [21]. Using a number of experienced and inexperienced operators, viewing the surface from a distance of approximately 2 meters and using a flashlight to illuminate the area, surface damage with an area of 1.4 mm^2 and a depth of 0.3 mm was readily detectable with a probability of 95%. Visual inspection is not only dependent on the distance and amount of light available during an inspection but also the angle of the light glancing off of the part under interrogation.

Traditional tap tests—for which a small metal hammer or coin is used to tap the structure under investigation and variations in pitch are detected by the inspector—and UT-based inspection methods have been commonly used to inspect composite structures.

2.6.1 NDI Techniques

Recently, alternative methods have increased the number of available inspection options. Over the last several years, a series of experiments, designed and implemented by Sandia National Laboratories, have been employed to assess how well both conventional and advanced NDI techniques can detect anomalies in composite aerospace structures [22].

The following NDI sources were identified and/or participated in NDI activities with the FAA/Airworthiness Assurance NDI Validation Center in composite flaw detection experiments:

- Computer-Aided Tap Testing (CATT) System [23]—designed to significantly improve the classic tap testing method by eliminating reliance on the technician's auditory interpretation skills. The impact duration of an instrumented tapper is measured and fed into a spreadsheet to produce two-dimensional images that reveal structural flaws
- Mobile Automated Scanner (MAUS)—a portable, scanning inspection system that integrates UT (pulse-echo, through-transmission, or shear wave) via resonance, pitch-catch, or mechanical impedance; with single- and dual-frequency eddy current inspection [24]. The system can achieve inspection speeds of up to 100 ft^2 (9.3m^2) per hour
- Motionless Laminography X-Ray System (MLX)—unlike conventional x-ray systems, the MLX is capable of capturing 1000 x-ray slices, each 1 mil thick, with a single exposure [25]. It reportedly produces fog-free, high-resolution digital images even with low-density materials such as composites. Large-area inspection can be performed without moving the object, detectors, or x-ray source
- Evisive Scan—a microwave nondestructive examination technology [26]. Microwaves are radiated from a transducer to the test specimen. A detectable signal is returned at each interface where the dielectric constant changes (e.g., where there are defects). The transducer may be moved at any speed. Data are displayed as a digitized image
- Terahertz Composite Inspection System—a nonionizing submillimeter microwave radiation technique (wavelengths between 0.1 mm and 1 mm) in the electromagnetic spectrum between 300 gigahertz and 3 terahertz [27]. Radiation at these wavelengths can penetrate composites, returning a signal that can establish a baseline for accurately fingerprinting a variety of anomalies
- Digital Acoustic Video (DAV)—an ultrasound imaging modality. The system features an ultrasound camera technology that generates real time images that are said to eliminate the uncertainty associated with conventional ultrasound [28]. The hand-held camera-type device is coupled to the part being inspected and a two-dimensional UT scan is viewed with a monitor
- High-Speed Laser Shearography—a system that detects changes in test part surface deformation down to 5 nm [29]. The device applies small stress changes, such as a 1° increase in temperature or 1 psi/0.07 bar increase in pressure. This alters the structure's surface displacement uniformly over pristine, uniform structure, but changes over defect areas. It detects these changes in real time as phases shift in the reflected light
- Laser UT Technology (Laser UT)—uses laser energy to detect defects in composite materials and is reportedly 10 times faster than water-coupled UT inspection machines [30]
- Woodpecker Automated Tap Testing Device—uses a solenoid hammer to produce a controlled impact on a structure's surface, while built-in sensors gauge the differences in the speed of the hammer rebound and use that data to display quantified information about defects [31]
- AIRSCAN—an air-coupled UT technology. For structures that cannot tolerate water, it overcomes attenuation issues by using specialized transducers, with frequencies from 50–400 kHz, to produce two-dimensional scans in either through-transmission or pitch-catch modes [32]
- RapidScan2 is a phased-array ultrasonic (PA-UT)—a system that is capable of generating high-resolution scans in a fraction of the time required when compared with single-element UT techniques [33]. The device uses a wheel probe that contains an array of up to 128

elements, each typically 4″ long, which enables the user to scan larger areas more efficiently

- Thermographic Signal Reconstruction (TSR) (pulsed thermography)—in its simplest terms, observes an object with an infrared (IR) camera while subjecting the object to a heat impulse. Variations in the IR radiation are sensed by the camera and converted to a video image, which maps the laminate interior [34]. A very short uniform pulse of light is used to heat the sample surface
- Rapid Damage Detection Device (RD3)—uses a lightweight hammer and an accelerometer that measures the speed at which the hammer bounces back (slower bounces occur on relatively softer structures, which can indicate damage) [35]. The device is cable-linked to a liquid crystal display, where numeric readouts correlate to flaws

2.7 FO SENSING

FO work on the principal that light can be guided by an interface between materials of different indices of refraction. The components of an FO line consist of a core with a higher index of refraction surrounded by a cladding with a lower index of refraction. The differences in the index of refraction in the core and the cladding cause light to be guided through the core.

As early as the 1980s, FO sensors were used to measure strain fields embedded in composite structures. Udd used a single mode optical fiber integrated into a carbon epoxy coupon to take strain measurements with a Sagnac interferometer [36]. These early tests were performed to monitor strains developed in composites during and after curing. In early tests using embedded fibers, the fibers were coated with an epoxy acrylate jacket that did not properly transfer strain to the optical fiber. Other tests on stripped fibers were performed. This method of embedding fibers provided adequate strain transfer to the fiber, but careful attention had to be taken during stripping and handling the fiber to keep the fiber from being damaged. It was discovered that a fiber coated with a polyimide material that has properties similar to resins found in organic composite materials properly transferred strain and protected the fiber during handling.

Also discussed by Udd is the response of the FO sensor to post-curing strain in a woven composite part. Depending on the fiber's diameter, placement, and orientation relative to the composite fibers, FO sensors could be used to determine the interply strain state of varying tow sizes [37]. Cross sections of FO sensors were also taken to determine how they affect the composite structure. It was determined that when an optical fiber was embedded perpendicular to the fiber tows, a resin pocket formed into an eye pattern that was a structural concern, which may result in the onset of failure. Many tests were conducted by multiple institutions and it was concluded that the fibers could, under certain conditions, be placed perpendicular to the fiber tows without affecting the overall strength of the part.

Fiber Bragg grating (FBG) sensors and interrogation systems have come a long way since early testing in the 1980s. Gupta presents an airworthy FBG-based SHM system that was used to monitor the health of unmanned aerial vehicles [38]. The SHM instrumentation consisted of an FBG interrogator, an onboard computer, a battery, electrical and FO connectors, and mounting fixtures. The system had the capability to interrogate the sensors and store the data. In validation testing, it passed multiple vibration, shock, and temperature tests. An artificial neural network was

developed to estimate flight loads during different flight regimes. The system was flight tested and successfully demonstrated the ability to monitor 16 FBG sensors, starting from launch to recovery.

In addition to using local FBG sensors with narrow gage length, Optical Frequency Domain Reflectometry (OFDR) can be used to interrogate distributed strain sensors that return strain values as a function of the linear position along an optical fiber. Murayama developed a distributed strain-sensing system using long-length FBGs based on OFDR [39]. In this work, 100 mm sensing length was achieved by serially cascading long-length FBGs. This resulted in spatial resolution of less than 1 mm. To demonstrate the system in an SHM application, single lap joint aluminum plates were investigated. The long-length FBG was set in a V-shaped grove within the bonded joint and used to measure the strain distribution along the interface between the adherend and the adhesive. The sample was then subjected to tensile loading and was failed. Strains were successfully measured and correlated well with finite element analysis. The system was also demonstrated on the 6-meter composite wing box shown in figure 5.

Figure 5. Composite wing box (right) and structural testing equipment used by Murayama

Multiple long-length FBGs were bonded along the length of the wing box structure and effectively used to measure the overall deformation of the wing box during loading.

Another example of OFDR-distributed sensing being used to monitor structural fatigue in a full-scale test is described by Duncan [40]. Optical fibers containing high-density FBG sensors were applied to the surface of a Lockheed Martin P-3C Orion full-scale fatigue test article. The purpose of the test was to assess the long-term structural damage detection and monitoring of the system and investigate unique 3-D visualization tools composed through wide area strain mapping. Results indicated good agreement with conventional resistance-based strain gages and the test demonstrated the potential for supplementing conventional NDI with the FO SHM technique.

Swept wavelength interferometry (SWI) is another method to measure Rayleigh backscatter as a function of length in a telecom-grade single-mode optical fiber. This can then be used to measure strain and temperature [41]. A sensor element is formed by transforming a spatial segment of the Rayleigh backscatter pattern into the optical frequency domain and measuring the induced shift in the reflected spectrum.

FBGs are commonly used tools to assess strain in FO, but they are not the only method. By using OFDR and standard poly (methyl methacrylate) plastic optical fiber (POF), strain can be measured by evaluating local backscatter within a fiber, as demonstrated by Liehr [42]. Using baseline scans, the authors were able to show that strained fiber sections could be detected with a special resolution of a few centimeters by evaluating the backscatter increase of POF fiber with increased strain. By applying a cross-correlation algorithm to the backscatter signal of the fiber, a length change occurring in the fiber relative to a reference measurement could be measured with a resolution better than 1 mm. The interrogation and evaluation techniques provide a reliable distributed strain sensor with a maximum measurement of more than 500 meters.

In addition to directly measuring strain to detect damage using optical fibers, a coil of fiber can be used as an acoustic sensor to collect UT waves produced by piezo-actuators [43]. Testing was conducted on a 1585 x 790 x 2.8 mm^3 CFRP quasi-isotropic plate, placing the piezo-actuators on one side of the plate and the FO sensors on the other. Waves generated by the actuators were picked up by the FO sensors. If a defect was in the path of the UT waves, they were deflected or attenuated when detected by the FO sensors, causing a change in response. It was shown that impact damage can be detected and located in CFRP plates, but with less clarity than in aluminum plates. Signal attenuation in composites, which is higher than in metallic structures, is an issue still being addressed.

Brillouin optical correlation domain analysis is another method of using optical fibers for damage sensing. This measurement technique is based on the principal that when a strain is applied to the fiber, the fluctuation of density changes the acoustic wavelength, thus making the Brillouin frequency change [44]. Bearing damage tests were conducted around holes drilled through quasi-isotropic 16-ply laminates to determine if Brillouin frequency shifts (BFS) could be monitored to detect the onset of damage during tension loading. Microdamage, such as out-of-plane shear cracking and interlaminar delamination, was detected by the BFS distribution changes.

3. EXPERIMENTAL METHODS

3.1 NDI TECHNIQUES USED

3.1.1 Single-Element UT Inspection

Conventional single-element UT inspection uses a piezoelectric transducer with a specific frequency to transmit UT waves into the part being inspected. Probe frequency is selected based on the attenuation, UT velocity of the material being inspected, and size of the defect intended to be detected. The relationship between frequency, velocity, and wave length are shown in equation 3.

The minimum defect detectable is half the wavelength:

$$\boldsymbol{f} = \frac{\boldsymbol{v}}{\boldsymbol{\lambda}} \tag{3}$$

$$\boldsymbol{d} = \frac{\boldsymbol{\lambda}}{\boldsymbol{2}} \tag{4}$$

where f is the frequency, v is the UT velocity of the material being inspected, λ is the wavelength, and d is the minimum detectable defect size.

The UT waves propagate through the part and reflect off of the back wall or are interrupted by discontinuities within the part. A UT inspection can be performed with a single send and receive transducer, also known as pulse-echo, or separate sending and receiving transducers, also known as pitch-catch or through-transmission. In most UT-based techniques, a coupling medium needs to be used to transmit the UT waves into the part. As an inspection is being performed, the inspector typically monitors the amplitude and position of the returned sound waves. This is done at a single point with an A-scan—or a two-dimensional, wide area C-scan, where a position encoding device is used to track the position of the transducer. A color pallet associated with high and low amplitude is used to produce an image of the part.

Example A-scans and a C-scan of a carbon fiber laminate impacted with simulated hail can be seen in figure 6. The peak in the A-scan shown on the left side of figure 6 represents a point measurement on a good area of the plate where the reflection is seen at the back wall. The second A-scan on the left represents a point measurement over a region that has an interply delamination. This flaw produces a new reflection, which shows up earlier in time in the A-scan than in the back wall reflection. A-scans show signal amplitude (*y*-axis) versus time of signal travel (*x*-axis) at the point of transducer placement. The red horizontal bar in the two A-scans is a gate that was set at the time location corresponding to the back wall of the part. The C-scan in the center is produced by the set of the maximum amplitude measurements under the gate at every point on the panel. In this particular scan, red or orange colors are high amplitude and blues, yellows, and greens are low amplitude.

In addition to amplitude C-scans, time of flight (TOF) or the position of the reflected signal can be tracked to inspect for changes in thickness. The A-scan taken at the good area in the figure is an example of a full-thickness measurement. As the transducer is moved over the delaminated area, the reflected sound signal shifts to the left, indicating a decrease in thickness.

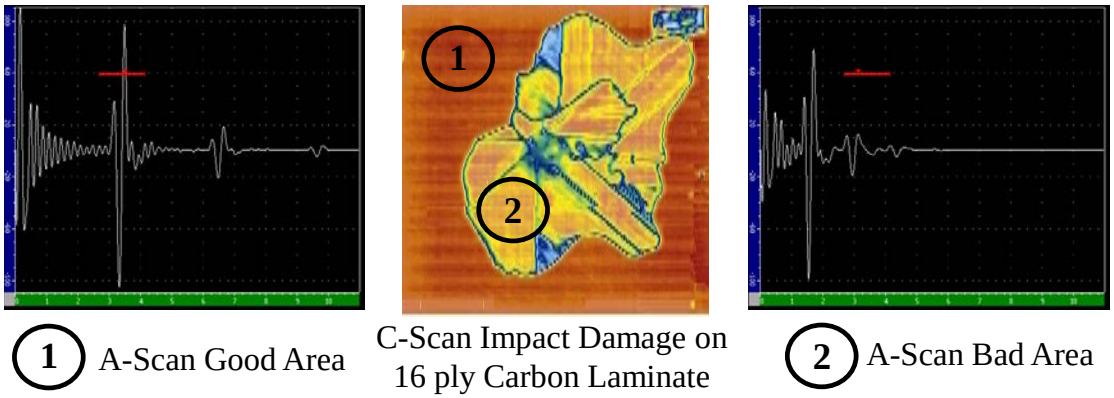

Figure 6. Examples of an A-scan over a good area, C-scan, and an A-scan over a bad area on a 16-ply carbon composite plate

3.1.2 Through-Transmission UT

Through-transmission ultrasonic (TTU) pass a beam of sound energy through a component under test. Instead of interpreting the returned wave as pulse-echo UT does, it uses the signals transmitted through the test piece. The TTU method requires the use of two transducers: one transmitting the UT wave, the other acting as a receiver. Figure 7 shows a TTU UT inspection system. The transducers must be accurately aligned with each other on opposite sides of the component under test. Disbonds, delaminations, or porosity in the test piece will prevent all or part of the transmitted sound from reaching the receiver transducer. As in pulse-echo UT, the TTU inspection and data interpretation can be improved through the use of C-scan systems. The C-scan records the echoes from the internal structure of the test part as a function of the position of each reflecting interface within the composite material boundaries. A detailed map of the part and flaws are shown as a plan view. Both flaw size and position within the plan view are recorded; however, flaw depth is not recorded when using TTU.

To perform an inspection using TTU, both sides of the test piece must be accessible. A water medium is used to provide the UT coupling. Inspections are performed with the test piece immersed in a water tank or positioned between water jets (UT squirter setup). When using the immersion method, the part and the transducers are submerged in water. The squirt method employs dynamic water columns that are squirted at the part while the transducers and the part are suspended (figure 7). The transducers, which are not normally in contact with the inspection surface, are mounted on fixtures that automatically maintain alignment while scanning the entire test piece.

Because of the efficient UT coupling and associated ability to optimize the amount of energy introduced to the test piece, automated, laboratory TTU immersion tanks or squirter systems are more accurate and sensitive than fieldable, hand scanning devices. The primary disadvantage is the need for parts to be removed from the aircraft for them to be inspected. Since this technique requires the sending-receiving transducer pair to be located in front and back of the structure being inspected, accessibility and deployment issues severely restrict the field application of TTU techniques. The motion of the transducer pair must be linked and water coupling to the structure, through complete immersion of the part or through focused water jets, is necessary. This further

complicates field deployment and affects the size of the structure that can be inspected. However, TTU is a very accurate NDI technique and was used primarily to establish a basis of comparison for other, more fieldable techniques.

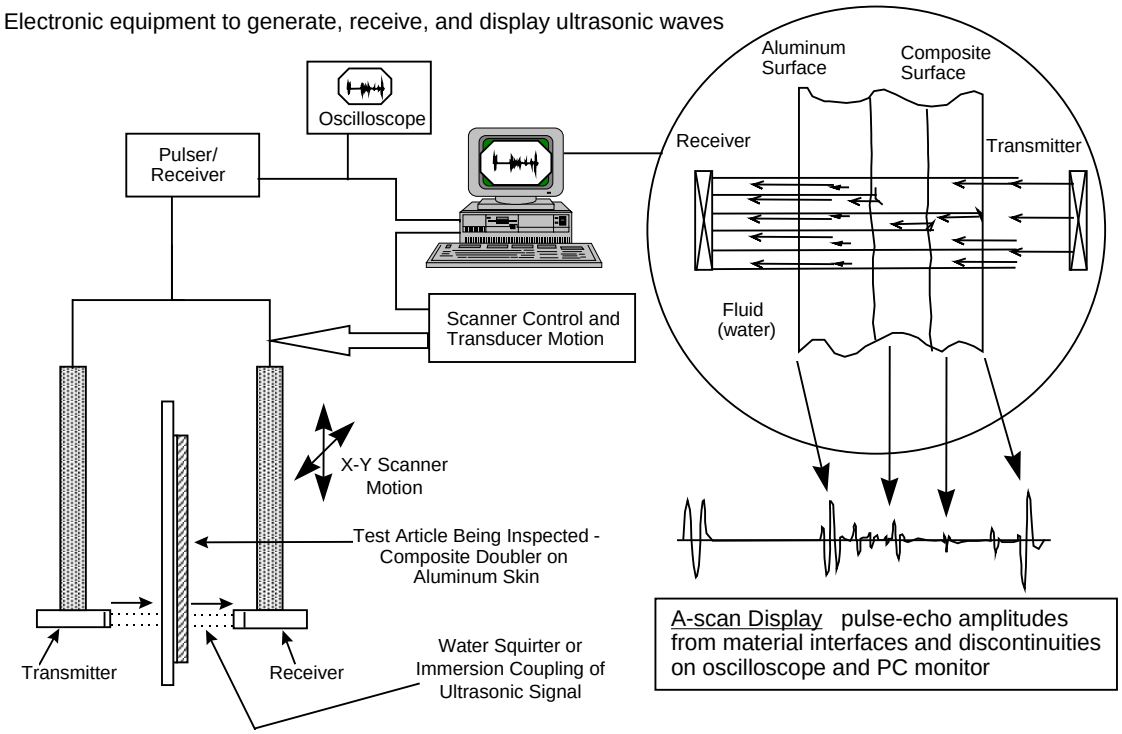

Figure 7. Through-transmission UT test setup

3.1.3 Phased Array UT Inspection

Conventional UT transducers for NDI commonly consist of either a single active element that both generates and receives high-frequency sound waves or two paired elements—one for transmitting, the other for receiving. Phased-array probes, however, typically consist of a transducer assembly with 16 to as many as 256 small individual elements that can each be pulsed separately. A phased-array system will also include a sophisticated computer-based instrument that is capable of driving the multi-element probe, receiving and digitizing the returning echoes, and plotting that echo information in various standard formats. Unlike conventional flaw detectors, phased-array systems can sweep a sound beam through a range of refracted angles or along a linear path—or dynamically focus at a number of different depths, thus increasing both flexibility and capability in inspection setups. The main difference between a phased array and linear array is that linear arrays are not capable of steering the sound beam at different angles or focusing the beam. Thus, the sound waves stay parallel to each other regardless of the depth.

PA-UT involves the use of multiple signals from a contained series of transducers (phased arrays) to produce diagnostic images in the form of UT C-scans. The operation is similar to hand-held UT; however, the simultaneous use of multiple sensors allows for rapid coverage and two-dimensional images from which to assess structural integrity. A linear array of UT sensors is placed within a single, scanning probe. The width of the linear probe array determines the swath of the inspection

scan as the probe is moved along the surface. A compression wave beam is electronically scanned along the array at pulse repetition frequencies in excess of 10 KHz. The response of each individual sensor is monitored and assessed using the UT wave analysis approaches described above. High-speed pulsing combined with rapid data capture permit the linear array to be quickly moved over the structure. The individual responses from each UT sensor are integrated to produce a real-time, C-scan image of the covered area. An example of a PA-UT inspection device, deployed by Sonascan in a rolling wheel arrangement, is shown in figure 8. The physics of how the UT array works is shown in figure 9. By carefully controlling the generation of UT signals and data acquisition from select elements in the array, it is possible to produce customized focusing of the array to improve the sensitivity of the inspection. Electronic focusing permits optimizing the beam shape and size at the expected defect location, thus further optimizing the probability of flaw detection. The ability to focus at multiple depths also improves flaw sizing of critical defects in volumetric inspections. Focusing can significantly improve the signal-to-noise ratio in challenging applications and electronic scanning across many groups of elements allows for C-scan images to be produced very rapidly.

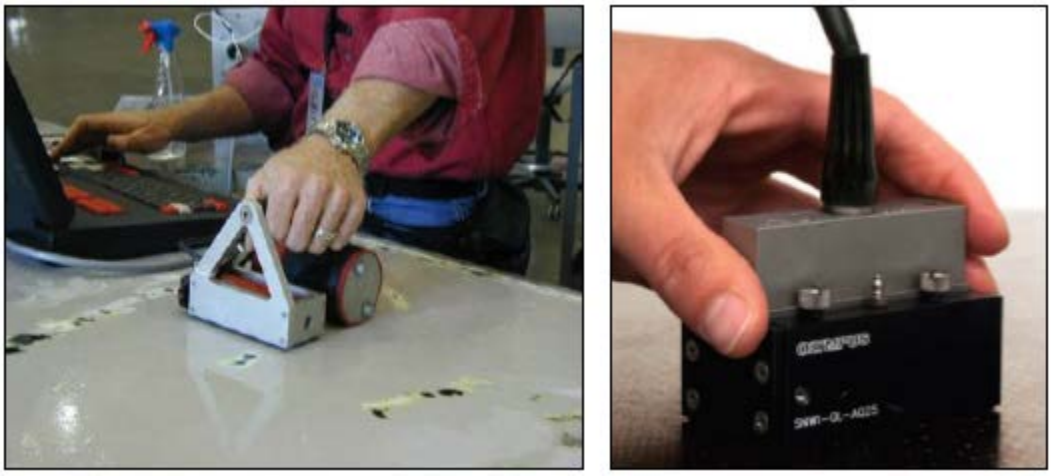

(a) **(b)**

Figure 8. PA-UT (a) deployed in a rolling wheel mechanism and (b) contained in a single probe housing

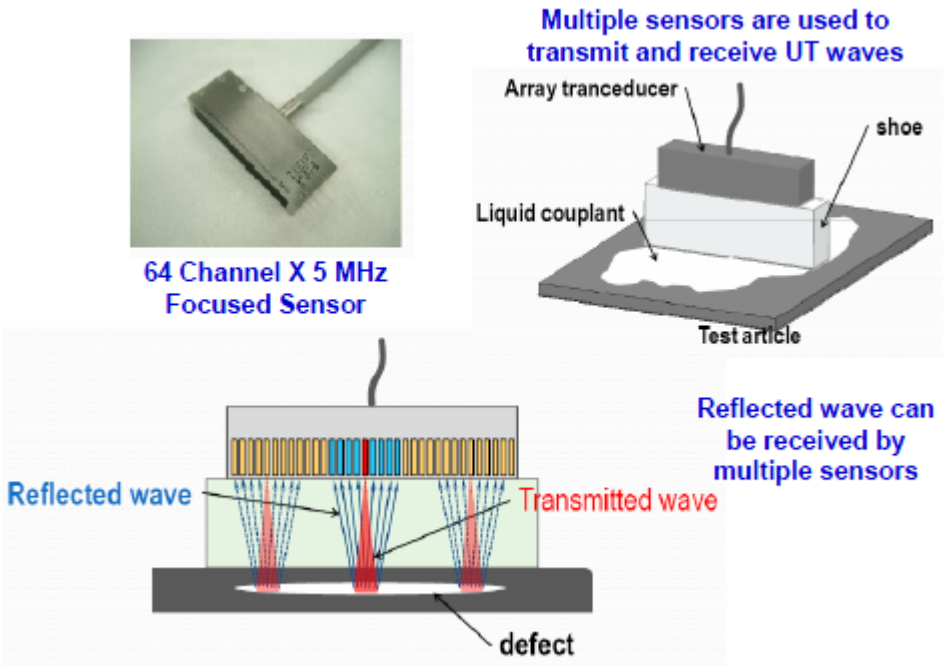

Figure 9. Operation of a UT array that allows for the generation and acquisition of multiple UT signals

3.1.4 UT Resonance Inspection

Resonance testing is also known as high-frequency bond testing. It is similar in application to conventional UT testing in that a resonance transducer is acoustically coupled to the sample being inspected using liquid couplant. Resonance testing uses special narrowband frequency transducers that can be excited at their natural resonant frequency by an oscillator in the instrument [45]. When the transducer is coupled to the test article, it produces a tuned, continuous standing sound wave in the material. The test material, in turn, provides a mass loading on the transducer, thus increasing the transducer bandwidth—which, in turn, changes the transducer's resonant frequency. Flaws in the material or changes in the material thickness result in significant changes to the transducer loading that cause changes in the transducer's resonant frequency. These changes are subsequently detected as differences in phase and amplitude. A flying dot or curser is displayed on the resonance testing unit on an X-Y plot. The X-axis corresponds to the signal amplitude, the Y-axis to the signal phase. The magnitude of the amplitude and phase is tracked and position data can be collected using a scanner.

To use resonance testing, the probe needs to be calibrated in an area where there is no defect. The probe is then nulled, or zeroed, to establish a baseline signal. If it is not possible to locate an area with no defect, the probe can be nulled in air for the starting point. The scan is then performed.

Figure 10 shows an example of resonance inspection results performed on a 24-ply carbon laminate impacted with a steel, 2″ diameter impactor. The figure shows an A-scan taken at a pristine location on the panel along with an A-scan at a large damage (A) area, a small damage (B) area, and a medium damage (C) area. The flying dot chart to the right of each resonant frequency

plot shows the magnitude of the phase and amplitude change at each location in an X-Y chart. The two C-scans at the top of the figure show the changes in the amplitude and phase.

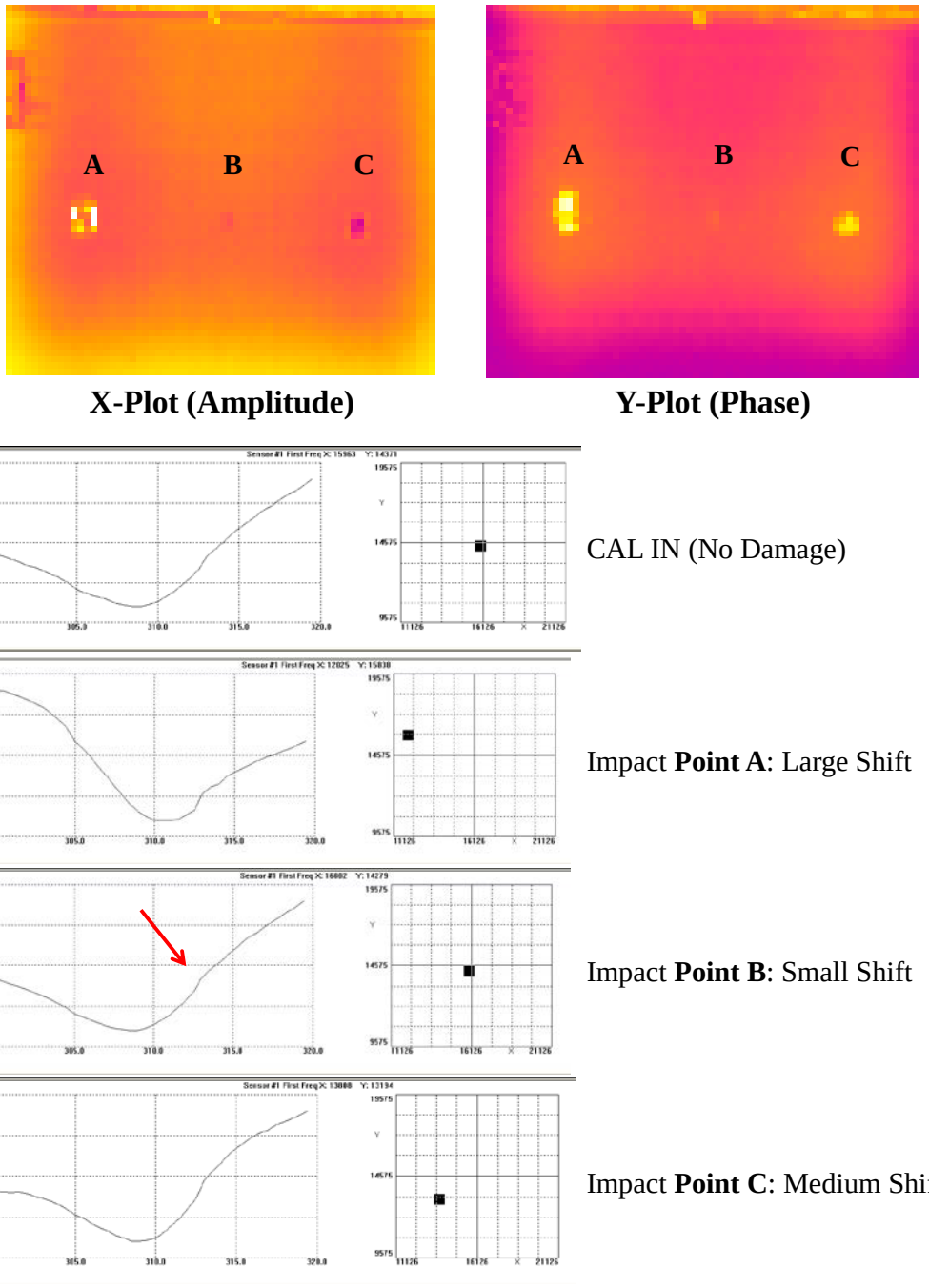

Figure 10. Resonance testing results for a 24-ply impact damage panel showing amplitude and phase shift plots (C-scans and A-scans)

3.1.5 Ramp Check Devices

Recently, two similar UT-based devices were released for possible use by airline personnel. These two pieces of equipment, shown in figure 11, are named the "Bondtracer" and "Ramp Damage Checker." Both are simplistic versions of standard PE-UT equipment, which, when properly calibrated on undamaged structure, can provide "Go"/"No Go" information regarding the presence of flaws in composite structures. One of the projected uses of this equipment is at airport gates, where non-inspectors with proper airline training could use these devices to determine if visual scuff marks (or other indicators, such as possible impact from equipment) are associated with actual damage to the composite laminate. Rather than displaying an A-scan signal as conventional PE-UT devices do, these devices internally compare the calibration signal from a representative composite laminate with the current inspection signal to determine if the change in the inspection signal is sufficient to indicate damage. The Bondtracer changes its lights from green to red to indicate damage, while the Ramp Damage Checker changes its screen readout from "good" to "bad" (figure 11) to indicate the presence of damage. These devices are intended to be used in local inspection scenarios only when visual clues or other events occur that warrant additional inspection of a small region.

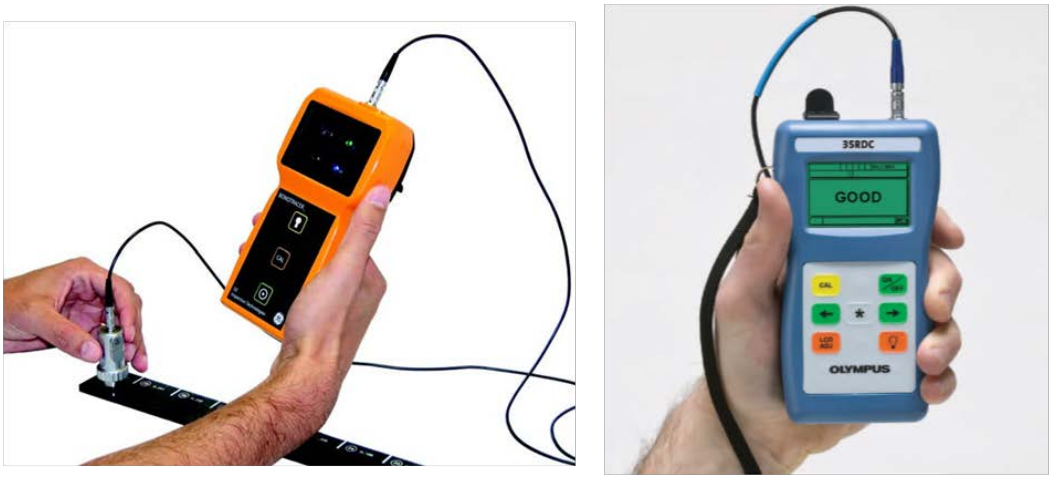

General Electric –
"Bondtracer"

Olympus –
"Ramp Damage Checker"

Figure 11. UT devices with "Go"/"No Go" capabilities used to detect hail impact damage in this study

3.1.6 Laser Ultrasonic Testing

Laser ultrasonic (LUS) is generally defined as a technology in which one laser generates UT displacements [46–48]. There are four main issues that have limited the adoption of LUS for the inspection of composites: 1) the lack of reliability of various prototypes used to validate the technology for production, 2) the high acquisition cost of the LUS equipment, 3) the small but significant differences between conventional and LUS signals, and 4) gantry-based LUS systems for production environments have demonstrated excellent results, but a fieldable (portable) system is not available for use in hangar environments.

3.1.6.1 LUS Deployment

LUS is a non-contact technique that uses a scanning laser beam to quickly move across the part in a uniform coverage pattern (figure 12). Ultrasound is generated by pulsing the laser beam, causing the surface layer to rapidly expand and contract through thermal expansion. The absorbed laser energy is converted into heat in the top 10–100μm of the surface. The resultant temperature rise creates a local expansion of the material in the frequency of ultrasound (1–10 MHz). Thus, a longitudinal UT wave is introduced into the part. Echoes from this wave, when they again reach the surface, are sensed by a coaxial detection laser and converted to images proportional to the echo strength. Laser light scattered off the surface is analyzed by an interferometer to extract the UT signals that are imprinted on the laser as phase and frequency modulations caused by the moving surface. The UT signals that are extracted are basically the same as those obtained with conventional UT systems. The two laser beams can be indexed over the material with a scanner to produce standard C-scan images [47].

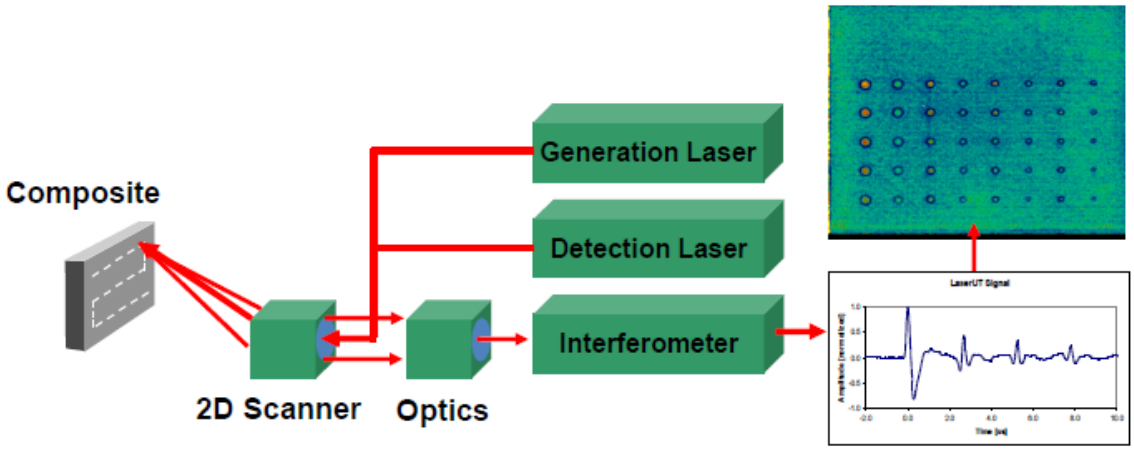

Figure 12. Laser UT system operation

This data transmission and acquisition does not require the laser beam to be deployed perpendicular to the structure as in other UT methods. Thus, it is possible to scan complex parts without detailed contour following. Ultrasound propagates perpendicular to the surface, regardless of the laser incident angle (up to + 45°). Currently, laser UT systems are deployed using a gantry system, which provides a high-speed, two-dimensional optical scanner to index the beams over the part. This allows for rapid inspections and generation of the C-scan images. Hand scanning using UT can be slow and tedious, leading to human factors concerns regarding coverage and human diligence. In addition, water-coupled UT can be difficult and time-consuming to implement on complex shaped parts. Figure 13 compares traditional UT inspections to a laser UT interrogation [47]. The first LUS systems mounted on robots [48] used gantry-type robots. Optical alignment of the CO_2 laser beam in the optical scanner must be precisely maintained to obtain valid UT results. The CO_2 laser cannot be efficiently transmitted by optical fibers. Therefore, the most obvious solution is to move the CO_2 laser along with the optical scanner. This approach requires gantry robots because only this type of robot can move equipment as large and heavy as an industrial CO_2 laser. Gantry robots present several disadvantages, the most important being their high cost. The gantry robot is typically the single most-expensive element of a LUS system that

includes such a robot. Several different deployments of the laser UT inspection technique and a schematic showing the ability to inspect parts without maintaining a perpendicular inspection orientation are shown in figure 14.

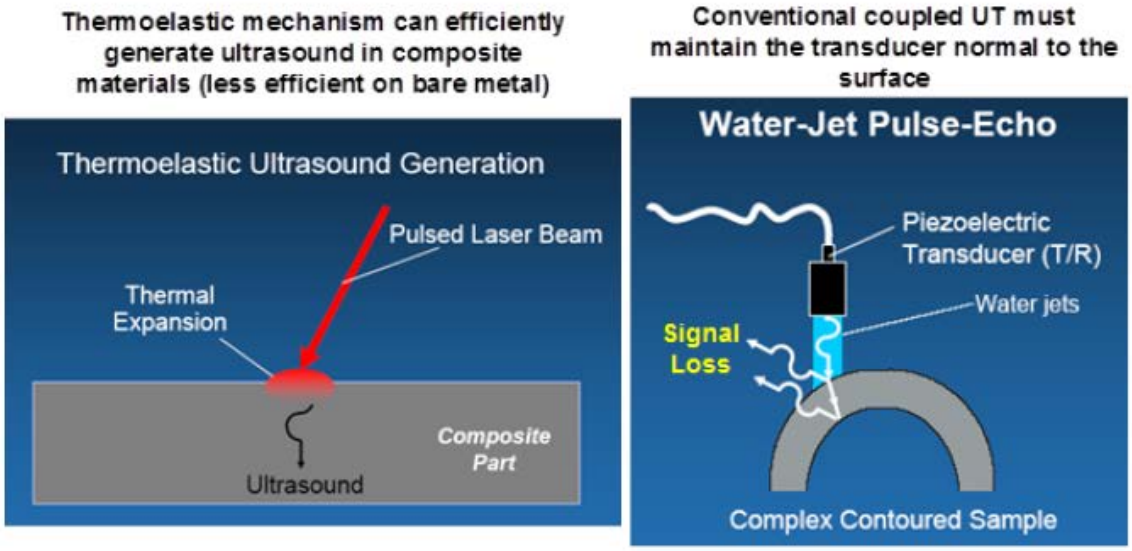

Figure 13. Comparison of conventional and laser UT interrogation of components

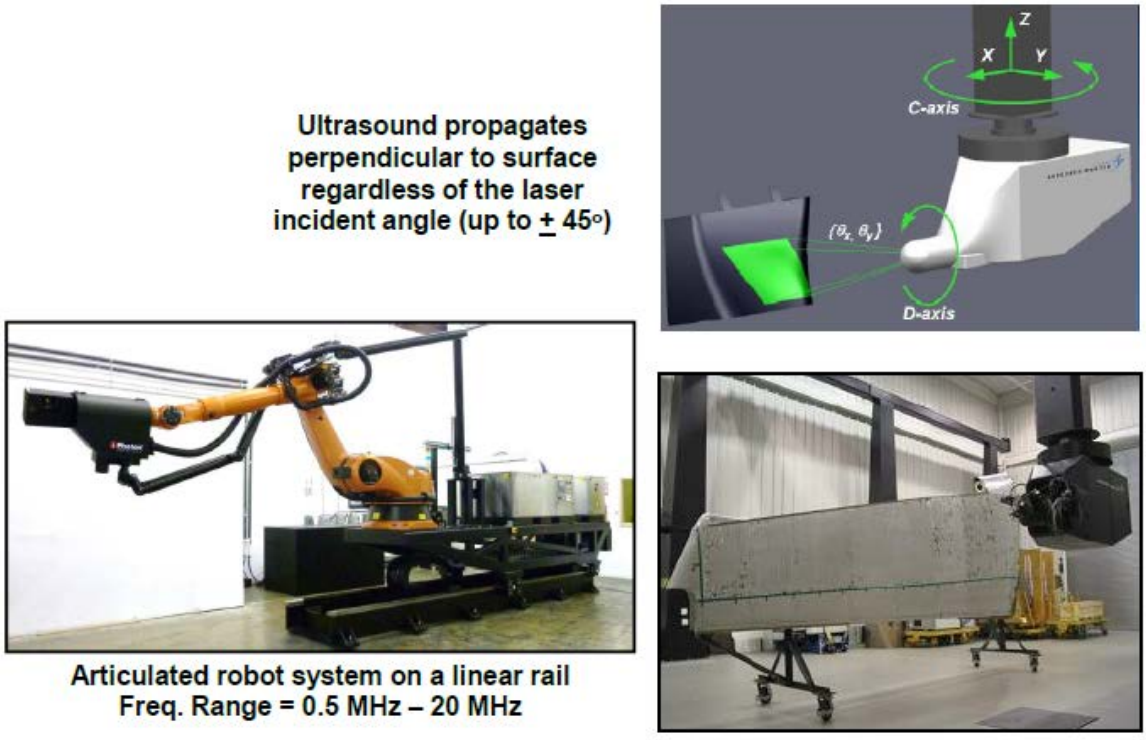

Figure 14. The laser UT method and deployment in gantry system and rail system

3.1.6.2 iPhoton Laser UT System

The iPhoton LUS concept, called iPLUS, was used to conduct the LUS inspections detailed in this report. An iPLUS III system is shown in figures 14 and 15. It uses a beam delivery system mounted on an articulated robot. To increase the working envelope, the robot, beam delivery system, and CO_2 laser are mounted on a linear rail. The linear rail provides an almost unlimited working envelope to the iPLUS system in one direction. Articulated robots provide flexibility not possible with gantry-based approaches. Some applications require the inspection of composite substructures inside larger structures, such as stringers inside a fuselage. Therefore, the iPLUS configuration was developed as a response to these applications. In the iPLUS III systems, the beam delivery system is composed of two standard beam delivery systems joined together on axis 3 of the robot. This approach, combined with a cantilevered linear rail, provides more than 6 m of penetration inside a structure (e.g., fuselage). For the inspection of parts, the iPLUS scan head is positioned using the articulating robot. Once the scan head is in position, the scanning is carried out by moving the laser beams along the surface of the sample using only the two mirrors of the scanner. The scan area is defined by the angular movement Θ_x and Θ_y of the two scanner mirrors. This process is illustrated in figures 14 and 15. When the scanning of one area is completed, the robot moves the scan head to the next pose to scan the next area.

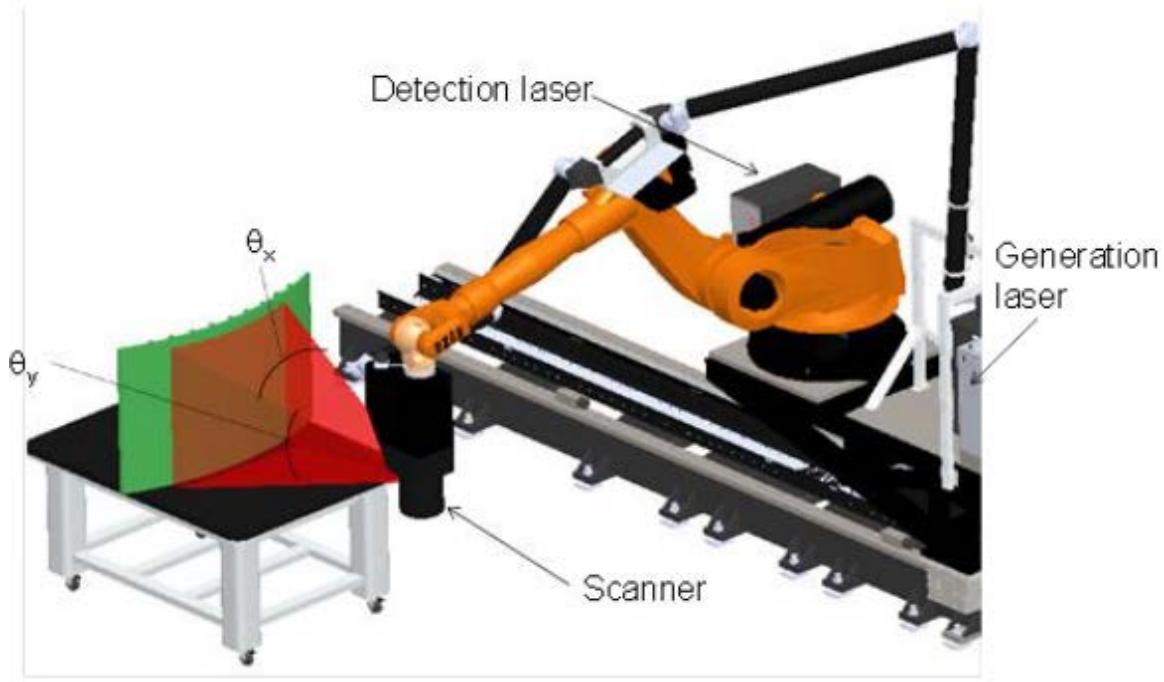

Figure 15. Inspection of a part using the iPLUS scan head and articulating robot

Figure 16 shows the iPLUS LUS results from a 16-ply 12″ x 12″ composite laminate panel that was damaged by SHI. The top left and top right are the amplitude and TOF C-scan images, respectively. The bottom graphics show an A-scan and B-scan corresponding to the red line in the top C-scans.

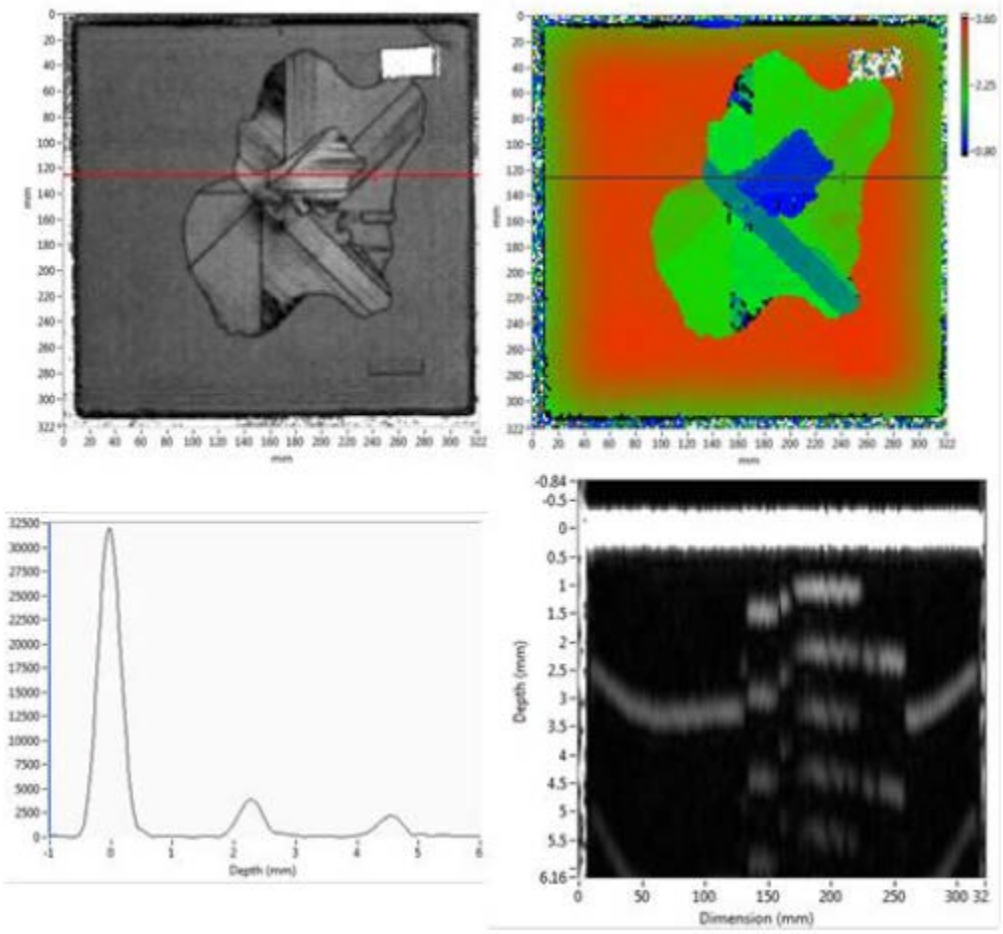

Figure 16. iPLUS laser UT scan of a 16-ply composite laminate with impact damage

3.1.7 Thermography

Thermography is an NDI method that uses thermal gradients to analyze the physical characteristics of a structure, such as internal defects. This is done by converting a thermal gradient into a visible image by using a thermally sensitive detector, such as an IR camera [49, 50]. Flash thermography relies on the heat absorption characteristics of the structure to indicate the presence of defects. In thermographic NDI, part of the IR band of the electromagnetic spectrum is used to map the surface temperature of an inspected item. The temperature distribution on a structure can be measured optically by the radiation it produces at IR wavelengths. Many defects affect the thermal properties of materials. Examples are corrosion, disbonds, cracks, impact damage, panel thinning, and fluid ingress into composite or honeycomb materials. In general, a source of energy is used to create a temperature difference between the specimen and the surrounding environment. Variations in the structure or material properties result in variations in heat flow and surface temperature, which are

recorded by the IR camera. Figure 17 shows a thermographic inspection system and highlights the physics of flaw detection.

Thermographic inspection is accomplished by using high-power flash lamps or another heat source, an IR video camera, and image-processing hardware and software—all of which are controlled by a personal computer. Through the judicious application of external heat sources, common aircraft defects can be detected by an appropriate IR survey. The heat source, such as flash lamps, is used to raise the surface temperature of the structure. The subsequent heat transfer into the material is affected by any defects that may be present. The resulting temperature distribution is then recorded by the IR camera and displayed on the computer monitor. As the heat diffuses through the structure, the surface temperature is monitored for a period of time by an IR camera. In practice, the computer actually obtains several images at progressively later times after each flash. Areas that appear hotter than normal may indicate the presence of a delamination or disbond beneath the surface that is preventing heat diffusion into deeper layers. By using a computer to analyze and manipulate the IR data captured over time, subtle variations can be enhanced in the image. Typical computer enhancements include analysis of the first and second derivatives of the heat versus time signatures at each point in the time sequence to produce images showing rates of change. Through the use of temperature versus time images produced by the thermography system, it is possible to determine the depths of disbonds, delaminations, and other flaws in a structure. Typical gantry-based and hand-held thermographic inspection systems are shown in figure 18.

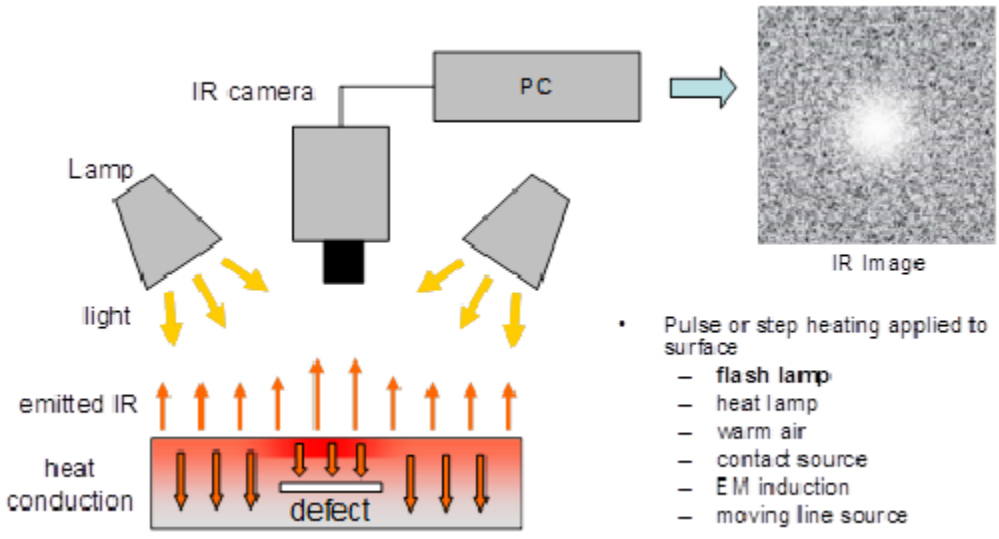

Figure 17. Principle of active pulsed thermography

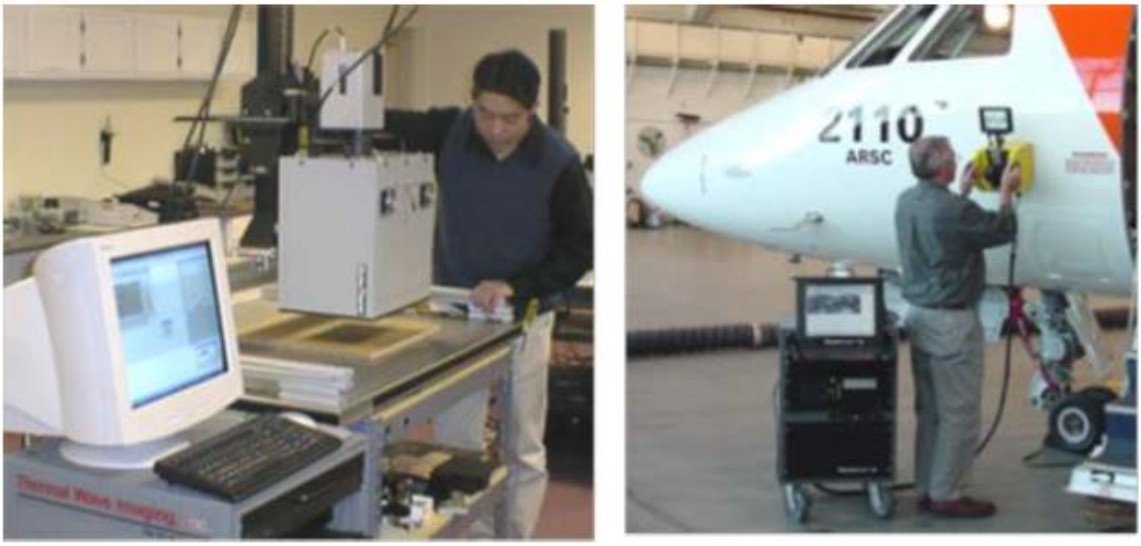

Figure 18. Laboratory thermal wave imaging system inspecting composite flaw-detection panels and portable field system inspecting an aircraft fuselage

Thermographic inspection procedures on aircraft parts can be used to detect certain local changes in materials that occur in homogenous parts. These may typically be considered (but not exclusively) as voids, inclusions, disbonds, fluid ingress or contamination, foreign objects, and damaged or broken structural assemblies. Thermographic inspection can be carried out on almost every type of material used in the construction of aircraft. The means of excitation, detection method, and inspection parameters can be varied depending on the material and flaws to be detected.

The advantages of the thermography inspection method include the following: 1) thermography can be performed without physical contact with the surface; 2) single images can include relatively large areas (1–2 ft^2), allowing for rapid inspections of large surface areas; and 3) two-dimensional images of the inspected surface help the operator visualize the location and extent of any defect. The primary disadvantages of thermography are: 1) it is often necessary to apply a high-emissivity coating during inspections to obtain an acceptable image; steps have been taken to minimize the labor time associated with this task and 2) damage to layers deep within a structure are more difficult to detect than damage in surface layers because the larger mass of material tends to dissipate the applied heat energy.

3.1.7.1 Thermal Wave Imaging EcoTherm Thermography Inspection System

For the hail impact detection study, a turn-key thermography inspection system, the thermal wave imager (TWI), was used to assess the merits of thermography to detect impact damage in solid laminate composites. Figure 19 shows a photo of this inspection device and example applications on aircraft. The TWI ThermoScope and EchoTherm NDI systems are designed for in-service applications and are integrated hardware and software systems designed for analyzing and measuring physical properties of materials using pulsed thermography. The system includes the TWI's TSR processing technique, which increases spatial and temporal resolution of thermogram sequences.

Figure 19. Thermal wave imaging system equipment and an inspection being conducted on an aircraft

Figures 20 and 21 show sample results from thermographic inspections on bonded tear straps and composite honeycomb structure, respectively. Figure 20 shows how a disbond between an aircraft skin and the substructure tear strap affects the thermographic image by changing the heat transfer in that local region. Similarly, the IR image in figure 21 shows the various flaws that were engineered into a honeycomb panel.

One of the limitations of thermography is the depth of penetration of the inspection: For composite laminates, the inspection depth limit is approximately 0.2″. Only flaws that manifest themselves as variations in the surface temperature of the structure can be readily detected by the IR camera. Ancillary heating methods are currently being used to infuse higher levels of heat energy into the structure improve the detection of deeper flaws.

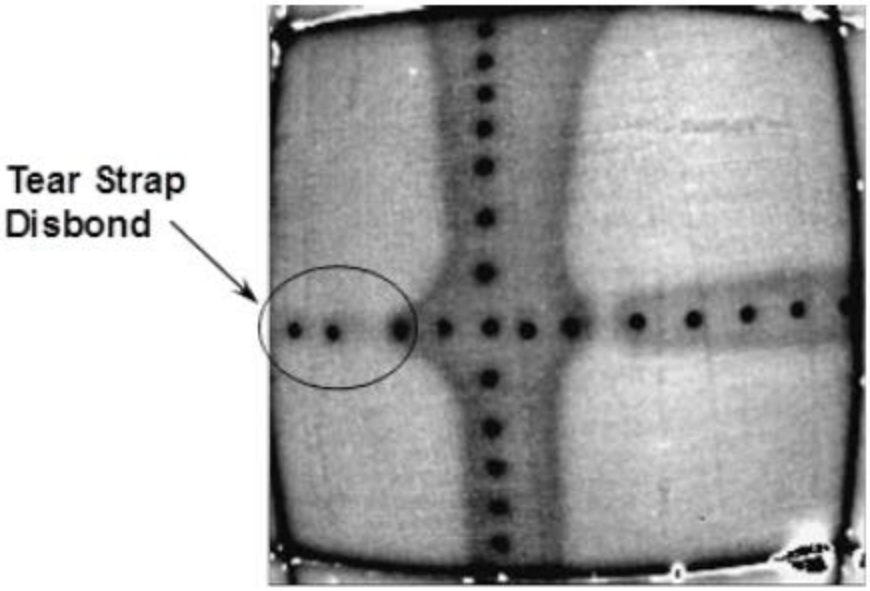

Figure 20. Sample thermography image showing a disbond in an aluminum fuselage tear strap structure

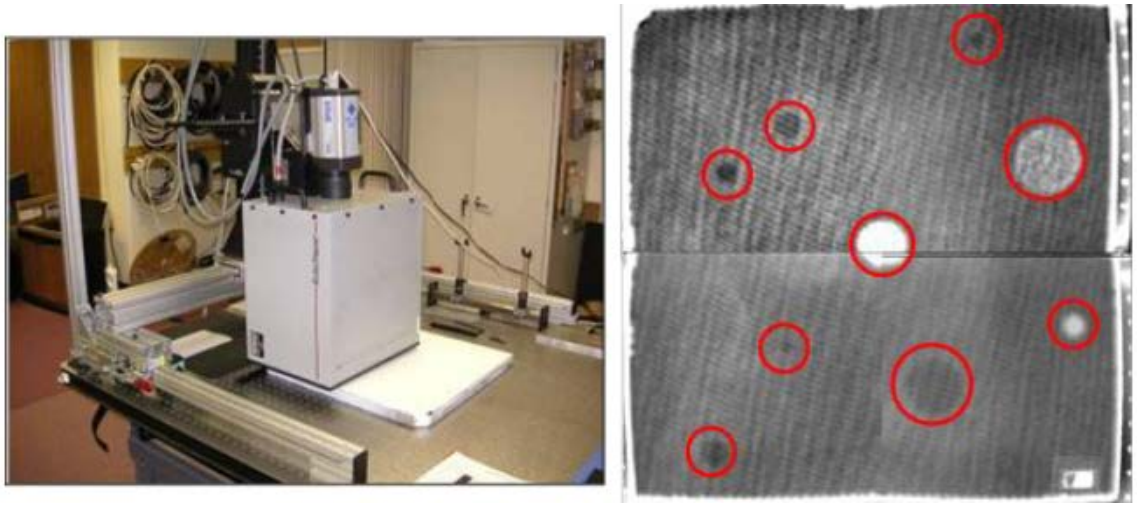

Figure 21. Flir A40 uncooled camera inspecting the honeycomb test panels. A sample IR image from a fiberglass panel

3.1.8 Swept Wavelength Interferometry Distributed Strain Sensing

Luna Innovations' Optical Backscatter Reflectometer™ (OBR), shown in figure 22, was used in this study to measure the strain in FO bonded and embedded in the full-scale panels. The OBR uses SWI to measure the Rayleigh backscatter as a function of length in optical fiber. An external stimulus (like a strain or temperature change) causes temporal and spectral shifts in the local Rayleigh backscatter pattern. The OBR measures these shifts and scales them to give a distributed temperature or strain measurement. The SWI approach enables robust and practical distributed temperature and strain measurements in optical fiber, with sub-centimeter-scale spatial resolution

of up to 70 meters of fiber with strain and temperature resolution as fine as 1 μstrain and 0.1°C [51].

Figure 22. Luna Innovations' Optical Backscatter Reflectometer™

Rayleigh backscatter in an FO is caused by random fluctuations in the index profile along the fiber length [41]. The scatter amplitude as a function of distance is a random but static property of an individual fiber and can be modeled as a long, weak FBG with a random period. Changes in the local period of the Rayleigh scatter caused by an external stimulus (like strain or temperature) in turn cause shifts in the locally reflected spectrum. These local spectral shifts can then be calibrated and assembled to form a distributed strain or temperature measurement [41].

3.2 COMPOSITE PLATE TEST SPECIMEN FABRICATION

The 12″ x 12″ impact panels produced for this study were fabricated in accordance with aerospace specifications and in conjunction with the University of California, San Diego (UCSD) [16]. The target panels were made from the Toray T800/3900-2 carbon/epoxy unidirectional prepreg tape (Boeing specification BMS8-276N) material system. The basic material properties are listed in table 4 [52]. This material has a cured ply thickness of 0.195 mm and is used in numerous aerospace applications, including the Boeing 787 fuselage and Boeing 777 rear empennage. To

make the specimens representative of aircraft laminates, an additional 0.05 mm thick Toray glass/epoxy plain weave (Boeing specification BMS8-331) ply was placed on the impact side of the panel (i.e., aircraft exterior surface). Approximately half of the panels also had a layer of aircraft standard epoxy paint applied by trained technicians at a United Airlines repair depot.

All manufactured panels were 304 mm square, or approximately 12″ x 12″ with three thicknesses (not including woven glass cover ply): 8 plies (1.59 mm), 16 plies (3.11 mm), and 24 plies (4.66 mm), having quasi-isotropic layup [0/45/90/-45]s, [0/45/90/-45]2s, and [0/45/90/-45]3s. Figures 23–26 show the ply orientation and quasi-isotropic layups for the three thicknesses discussed.

After every four plies were laid up in the laminate, the assembled plies were debulked under vacuum bag pressure for 10–15 minutes. Figure 27 shows an example of a panel layup and two panels under debulk. All plies were cut and laid up as individual 304 mm square panels in preparation for autoclave curing under 620 kPa pressure at 179°C, with a hold time of 130 minutes. Because the material was a no-bleed system, 304 mm square caul plates were wrapped in release film and placed on top of each panel, providing a smooth surface on both sides of the panel. Small holes were made near each corner of each panel to allow gas to be released during the cure. This cure cycle was in accordance with the cure cycle specifications provided by Toray. A total of 81 flat plate test specimens were fabricated to support the hail impact study detailed in this report.

Table 4. T800/3900-2 carbon fiber material properties [52]

	T800/3900-2 (tape)
Young's modulus	
E_{11} (GPa)	160
E_{22} (GPa)	8.97
E_{33} (GPa)	8.97
Poisson's ratio	
ν_{12}	0.28
ν_{13}	0.28
ν_{23}	0.36
Shear modulus	
G_{12} (GPa)	6.21
G_{13} (GPa)	6.21
G_{23} (GPa)	3.45
Strength	
Longitudinal tensile (MPa)	2843
Longitudinal compressive (MPa)	1553
Transverse compressive (MPa)	166
Mode II strain energy release rate (J/m^2)	2100

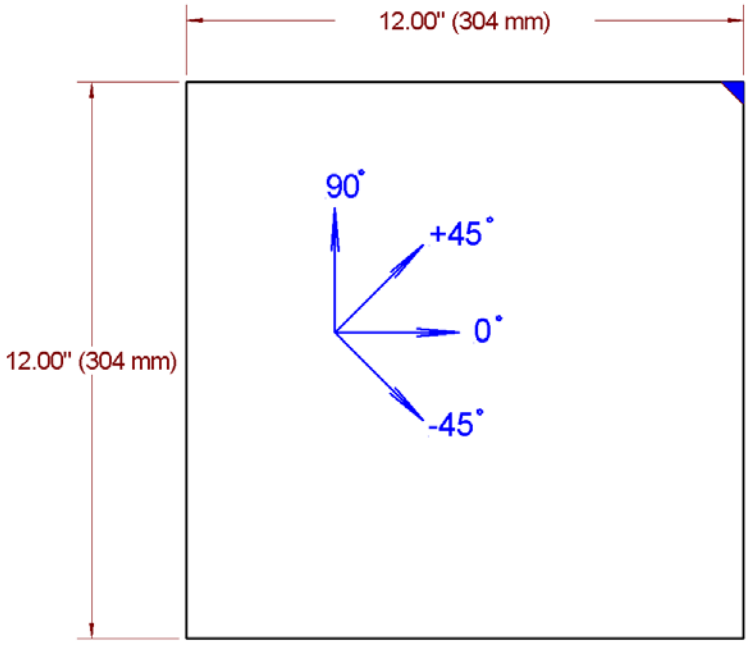

Figure 23. Ply orientation for all flat plate panels

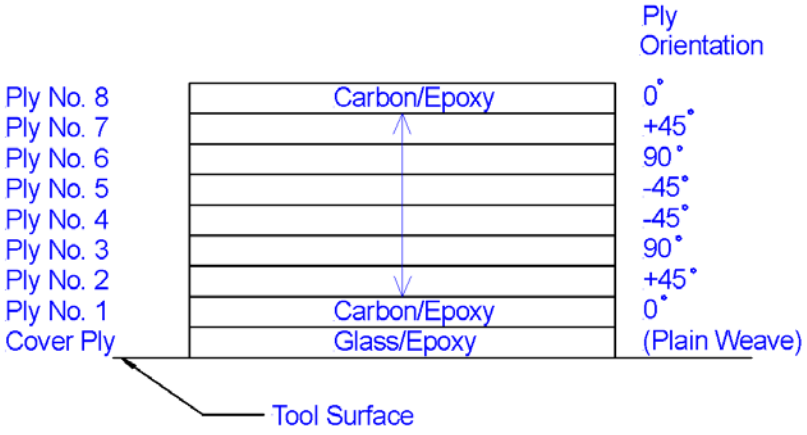

Figure 24. An 8-ply quasi-isotropic layup [0/45/90/-45]s

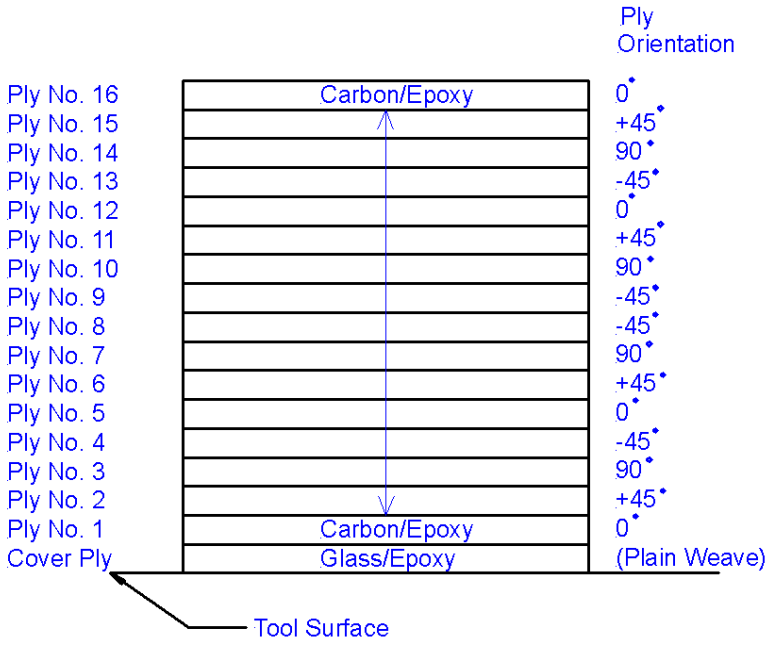

Figure 25. A 16-ply quasi-isotropic layup [0/45/90/-45]2s

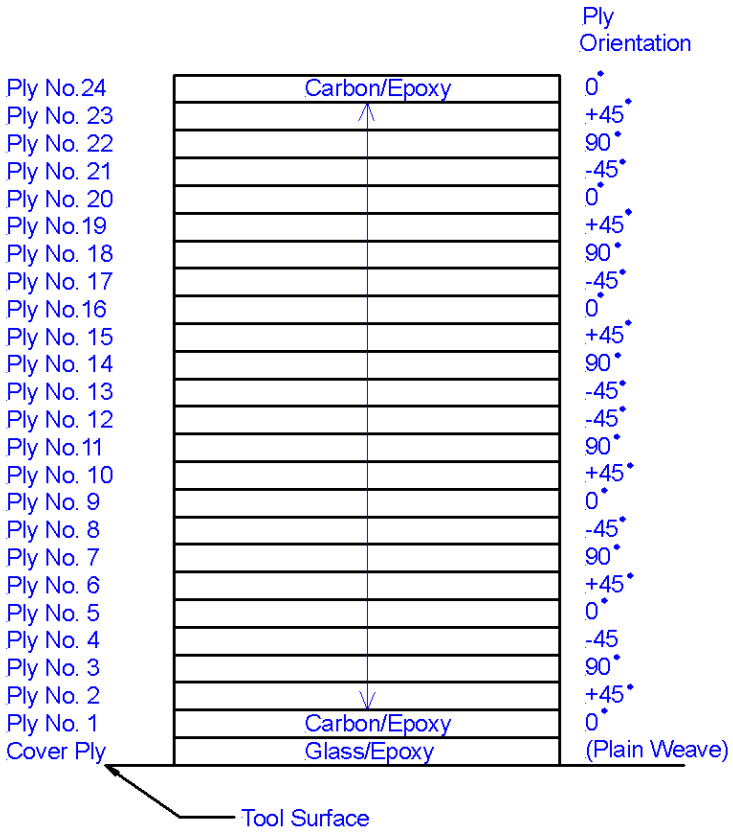

Figure 26. A 24-ply quasi-isotropic layup [0/45/90/-45]3s

Figure 27. Panel layup and vacuum bag setup for panel debulking

3.2.1 Effect of Lightning Strike Protection on Inspection Results

A limited number of flat plate panels with engineered defects were fabricated to assess the effect of lightning strike protection (LSP) on subsequent NDI. There were two panels fabricated: an 8-ply panel and a 16-ply panel. Half of each panel was covered with a copper mesh LSP layer embedded one ply under the fiberglass cover ply. Figure 28 shows that each side of the LSP test panels had identical flaw profiles embedded mid-depth in both the 8- and 16-ply panels. The engineered defects used in these panels included pillow inserts, Teflon inserts, pre-preg backing material, graphite foil inserts, grease contamination, and hollow carbon spheres.

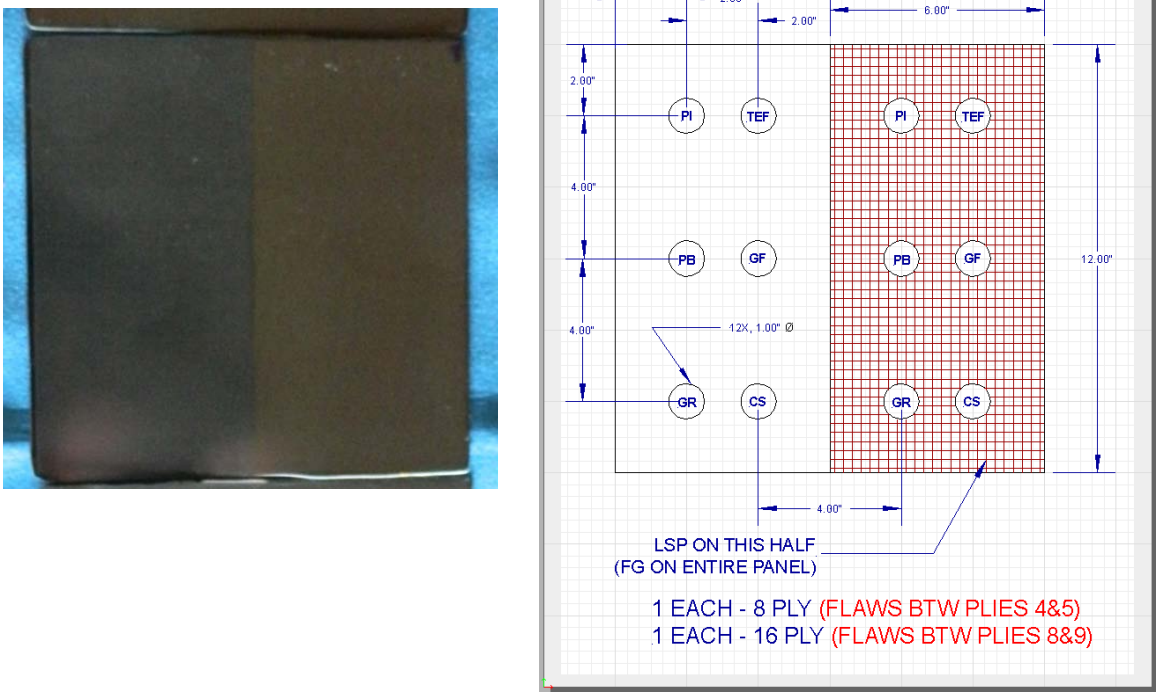

Figure 28. Lightning strike protection test panel design

The copper mesh used in the LSP test panels was an Astrostrike® product fabricated by Astroseal Products Mfg. Corp. It was a 0.015 lb/ft^2 (73 grams/m^2) copper mesh treated with a corrosion-resistant coating and selected based on what is currently being used on composite fuselage structures on aircraft.

The MAUS V scanning system was used to inspect the LSP panels in both UT and resonance modes. For the UT inspection, a 0.5″ diameter 5 MHz single-element UT transducer was used. The C-scan inspection results in figure 29 show that the LSP had very little effect on the inspection results—other than a slight decrease in UT amplitude over the LSP—in both the 8- and 16-ply panels. Figure 30 shows inspection results from the resonance inspection applied to the LSP test panels. Similar to the UT inspection results, the LSP had little effect on flaw detection using resonance. Of note, differentiation between the LSP and non-LSP sides of each panel was not possible using resonance. This is because the LSP layer was not substantial enough to vary the phase or amplitude of the reflected resonance signal.

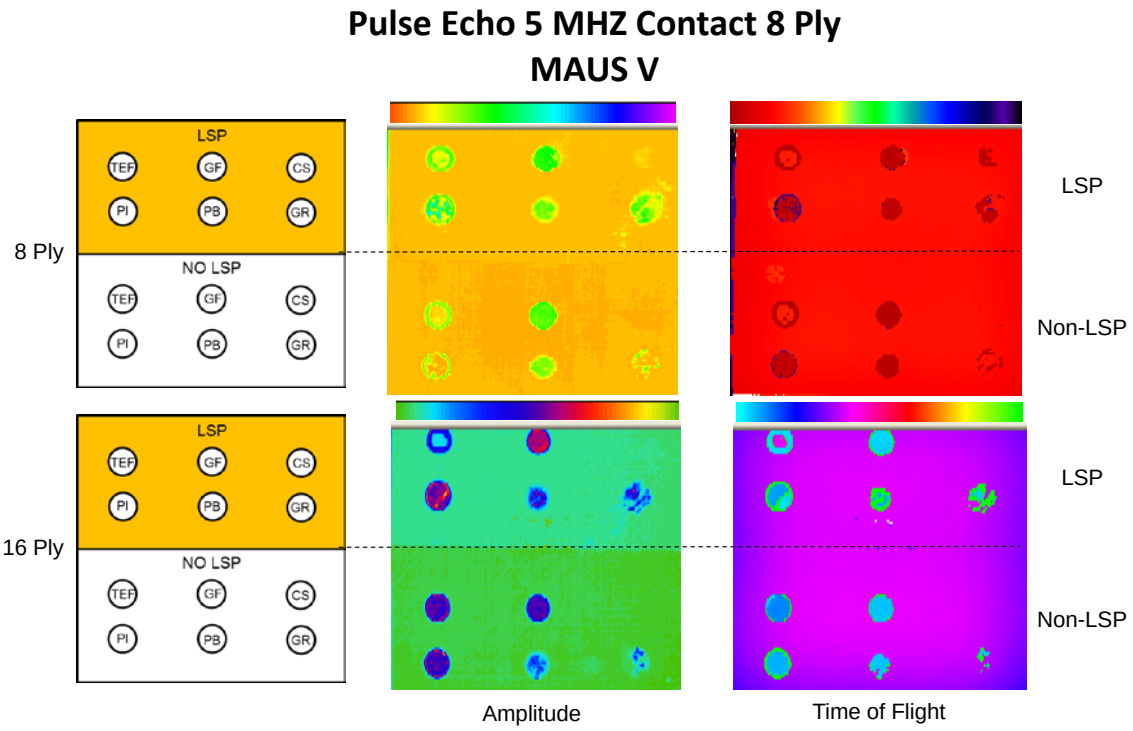

Figure 29. The UT C-scan inspection results of lightning strike protection test panels

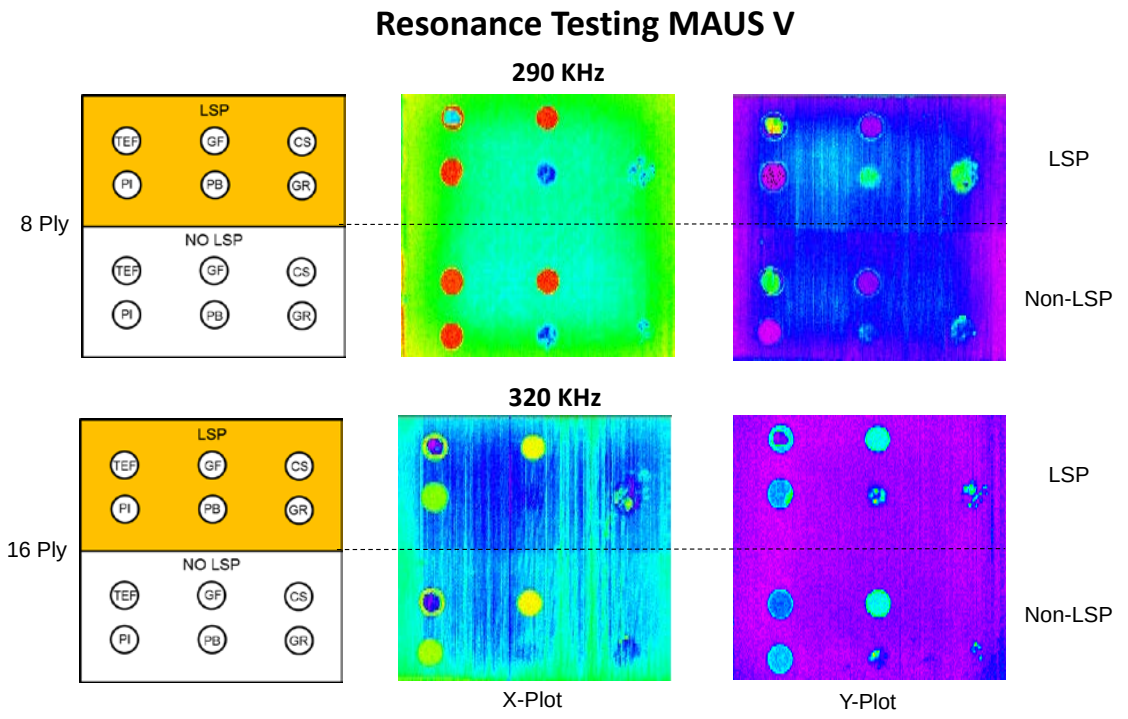

Figure 30. Resonance C-scan inspection results of lightning strike protection test panels

3.3 SHI TEST SETUP FOR COMPOSITE PLATES

High velocity SHI testing was performed in collaboration with UCSD. Figure 31 shows a schematic of the UCSD gas gun test facility. The gas gun was used to fire varying diameter ice balls into the panels at high velocity. The hail velocity to be considered was the relative velocity of the hail, or speed of the airplane plus the speed of the hail. Glancing blows were not considered in this testing.

The test facility consisted of the following (see figure 31's labels):

1. Gas gun composed of high pressure gas tank filled with nitrogen to a specified pressure, depending on the intended ice ball velocity; helium actuated pneumatic ball valve; breach; and barrel

2. Nitrogen gas storage tanks

3. Laser diode and photo detector in trajectory path of projectile to trigger lights and high-speed camera measurements

4. Sabot stopper used to disengage the sabot from the ball of ice prior to impact

5. Two laser diodes and photo detector contained in an aluminum housing, whose laser path was interrupted by the projectiles' trajectory as a means to measure the ice balls' velocity

6. High-speed cameras used to measure velocity and determine if the ice ball was still intact at time of impact

7. Panel being tested, secured with a frame constructed with 80/20 aluminum structure

8. Luna Innovations' OBR FO interrogator

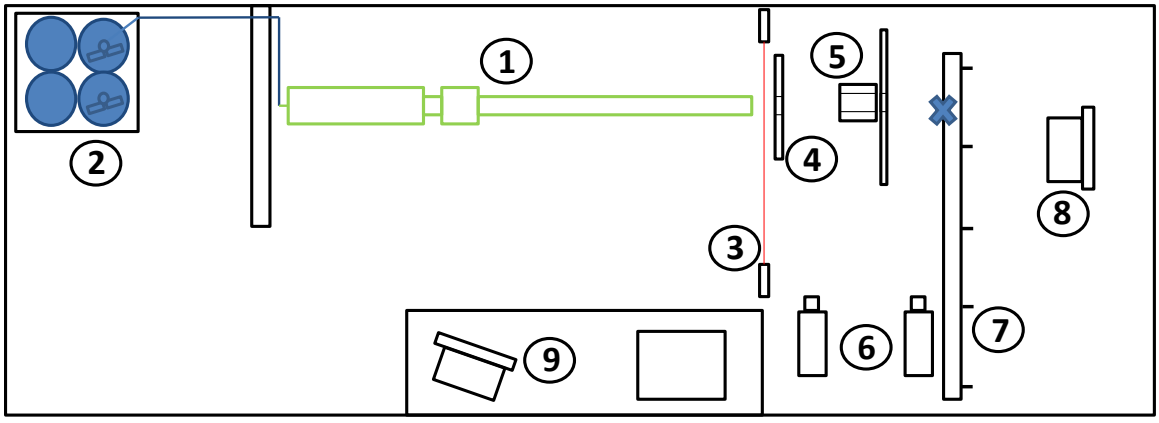

Figure 31. The UCSD gas gun test facility

The nitrogen propellant gas was used to fill the high-pressure storage tank on the gas gun. Based on previous testing data, a tank pressure versus exit velocity chart was used to determine the pressure level needed to achieve a desired impact velocity. Simulated hail balls were placed in sabots and then inserted into the breach. To launch the simulated hail, helium gas was used to actuate the ball valve, which then opened and released gas from the propellant gas tank. The gas expanded and exerted pressure onto the sabot and projected the ice ball and sabot through the 79.300 mm φ x 2286 mm (3.122 in. φ x 90 in.) barrel. After exiting the barrel, the sabot hit a stop plate and was dislodged accordingly from the ice ball as it continued its trajectory through the laser velocity measurement system and high-speed cameras before impact with the target. The gas gun is shown in figure 32.

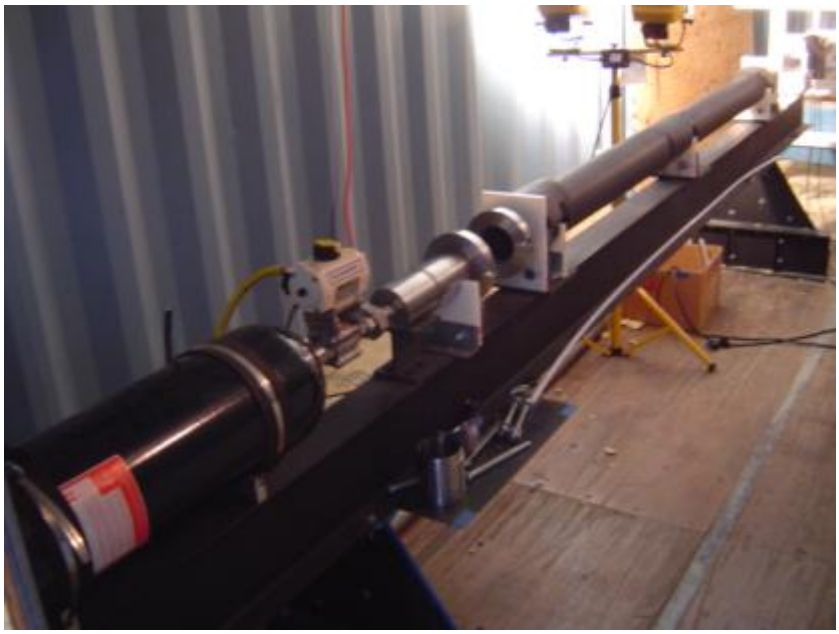

Figure 32. Gas gun used for high-velocity ice ball impact testing. Depicted are the high-pressure gas tank, pneumatic actuator, breach, and barrel

To secure the flat plate test panels during hail impact testing, an aluminum “picture frame” fixture was used. The test plates were secured around the outside perimeter and tightly clamped. The aluminum fixture used to secure the panels and a cross section schematic are shown in figure 33. All impact tests were directed at the center of each panel.

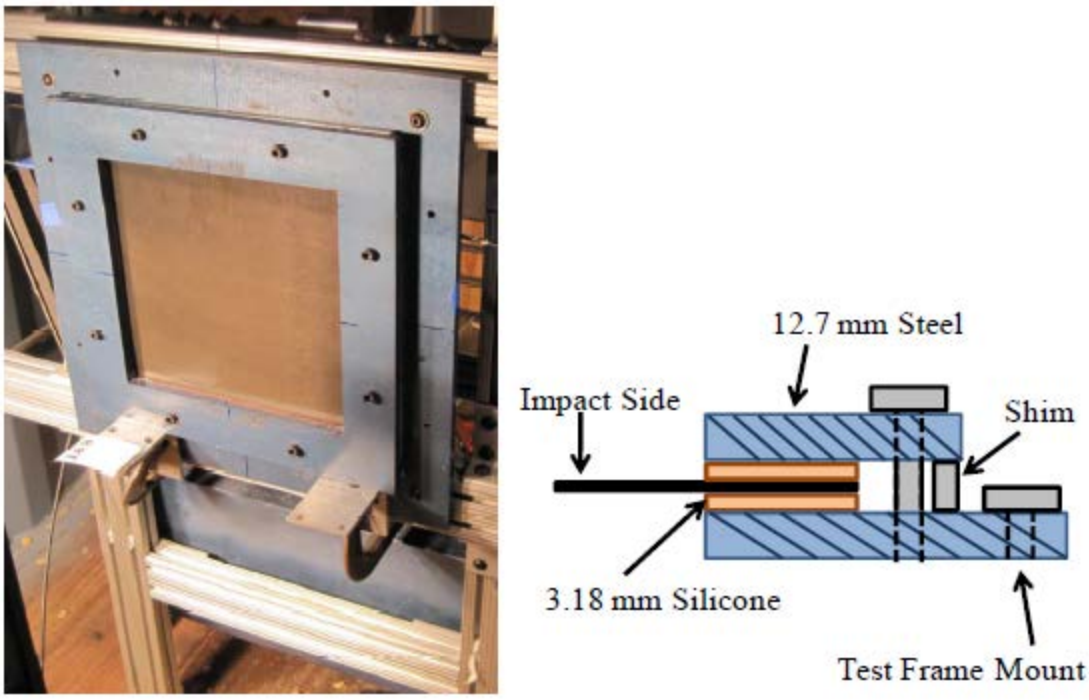

Figure 33. Test fixture used to secure flat plate test specimens during impact testing

3.4 CARBON FIBER FUSELAGE PANEL FABRICATION

This report seeks to assess the use of conventional and advanced NDI techniques to detect simulated hail damage and hardened, spherical type impact damage in full-scale aircraft composite structure and investigate the use of an FO strain sensing system to detect and localize damage. To test the FO strain sensing system and various NDI techniques to detect damage, in addition to the flat plate panels, two full-scale carbon fiber fuselage sections were fabricated. They consisted of skin, co-cured stringers, fastened shear ties, and frames. The composite panels were painted using an aircraft-grade epoxy primer and JetGlo Express paint and were instrumented with bonded or embedded FO. Figure 34 shows the 56″ high x 76″ long carbon fiber fuselage sections after fabrication. The panels were designed to be representative of structures found on large, advanced composite commercial transport category aircraft. The intention was to generate varying levels of impact damage in the panels to assess the sensitivity of various NDI techniques and the FO system. Because testing was focused on localized impact damage, the normal carbon fiber frames used in an actual aircraft were replaced with aluminum frames with similar global stiffness properties. These are not shown in the figure.

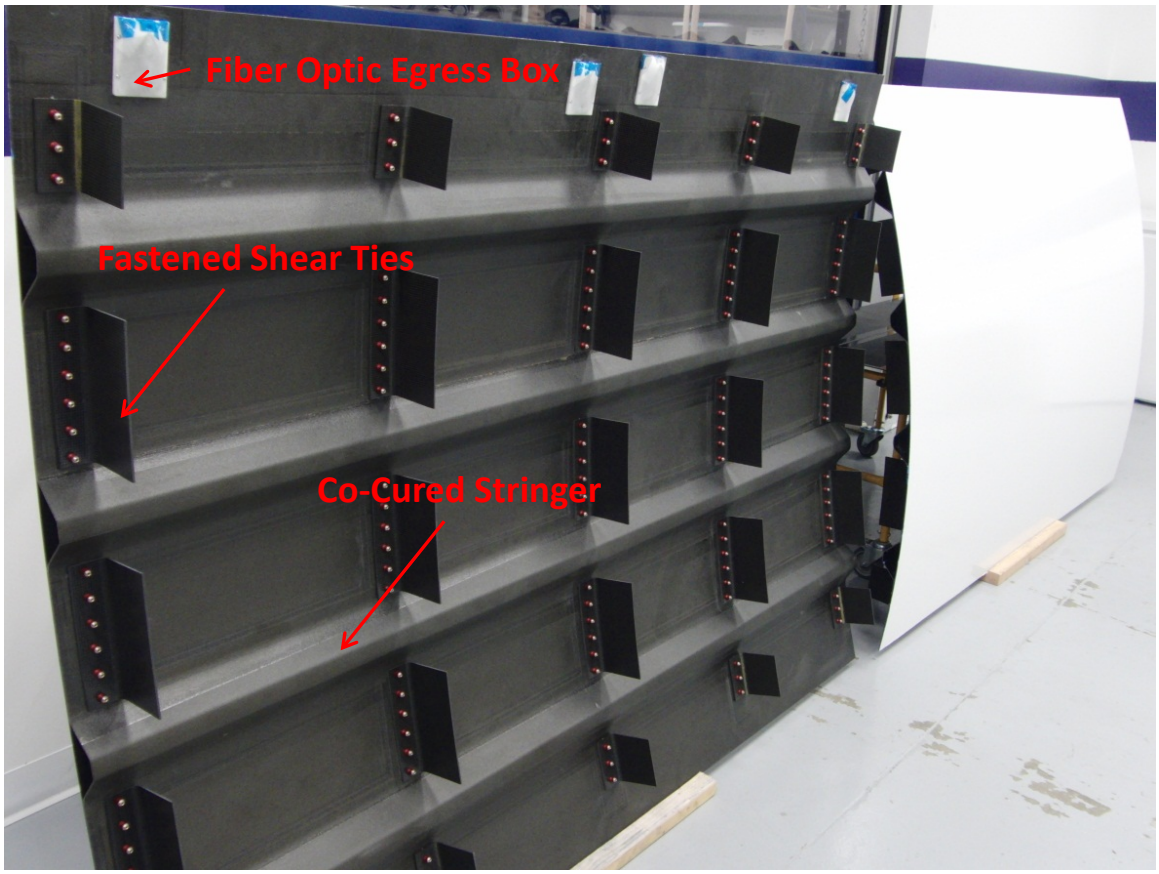

Figure 34. Backside and frontside views of carbon fiber fuselage sections

The skin layup of the panels was a 16-ply quasi-isotropic, symmetric $[0,45,90.-45]_{2s}$ layup with a fiberglass cover ply. The material used for the skin, stringers, and shear ties was T800 unidirectional pre-preg tape with a 3900 series resin system made by Cytec (Boeing specification BMS8-276). The layup for the skin of the panel can be seen in figure 35. The glass cover ply material was a thin woven bidirectional glass, also with a 3900 series pre-preg resin system (made by Cytec). All edges of the unidirectional taper were butt spliced with a maximum allowable gap of 0.020″. A curved aluminum caul plate was custom designed and fabricated to construct representative fuselage curvature.

3.4.1 Embedded FO

The FO used for the embedded and bonded panels was an 80-micron polyimide clad telecom grade fiber. The FO was embedded 11 plies deep in the 16-ply skin, which is approximately three quarters the depth of the skin thickness. This location was selected because the fiber would have less of a chance of being crushed near the surface of the skin when impacted and has a higher chance of maintaining residual strain after impact because it is on the other side of the neutral axis, or the mid-plane, of the skin.

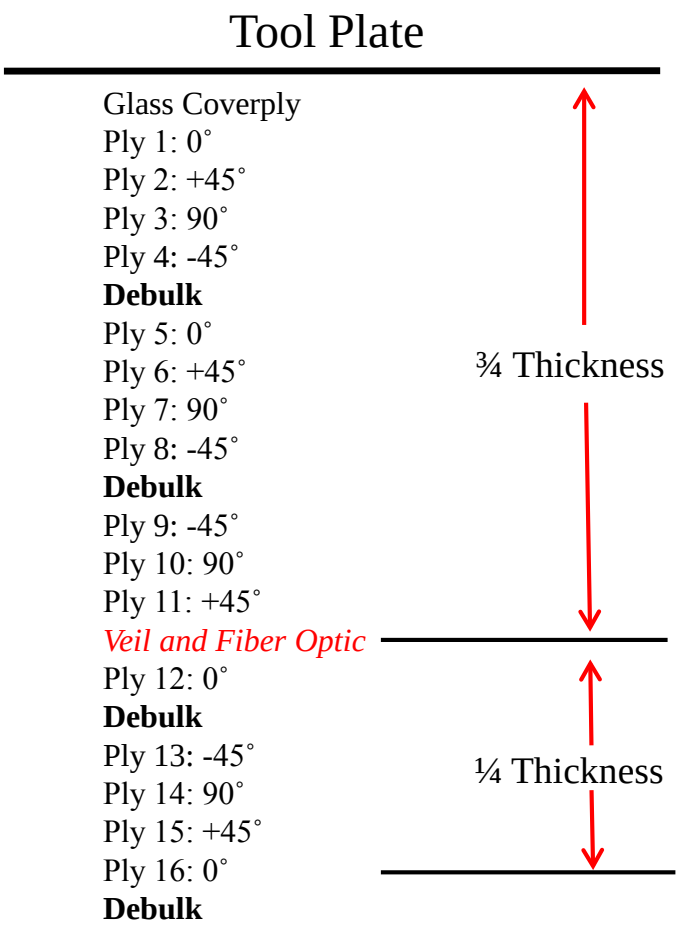

Figure 35. Skin layup showing where in the skin the FO was embedded

To embed the FO in the panel during fabrication, an FO layout was designed to provide some redundancy if a fiber were to break during testing, which would also avoid the areas where the shear ties would be fastened to the skin of the panel. The fiber was attached to a thin veil made of carbon weave, enabling it to easily be laid out onto the layup during manufacturing.

3.4.2 Effect of FO Carrier on NDI

To determine whether the veil material would have an adverse effect on the structural integrity of the fuselage skin, a section of veil material with a short section of fiber was embedded in half of a 12″ x 12″ carbon T800 layup and laid up and processed in the same way as the full-scale panels. A picture of the test panel with the layout of the veil and FO can be seen on the left side of figure 36. The veil/FO side is shown in red. Also in the figure are UT C-scans of the test panel showing little change in UT amplitude between the veil and non-veil sides of the panel. The center scan was taken using the Boeing MAUS V system with a 5 MHz contact probe. The right UT C-scan was taken using a 5 MHz TTU probe in an immersion tank. The contact probe test indicated some areas of decreased amplitude, but the TTU did not. This discrepancy was caused by surface demarcations on the panel that allowed the contact probe to rock and lose contact with the part.

There were no disbonds or resin flow issues shown in the NDI that indicated that the veil/fiber was an impediment to subsequent inspections.

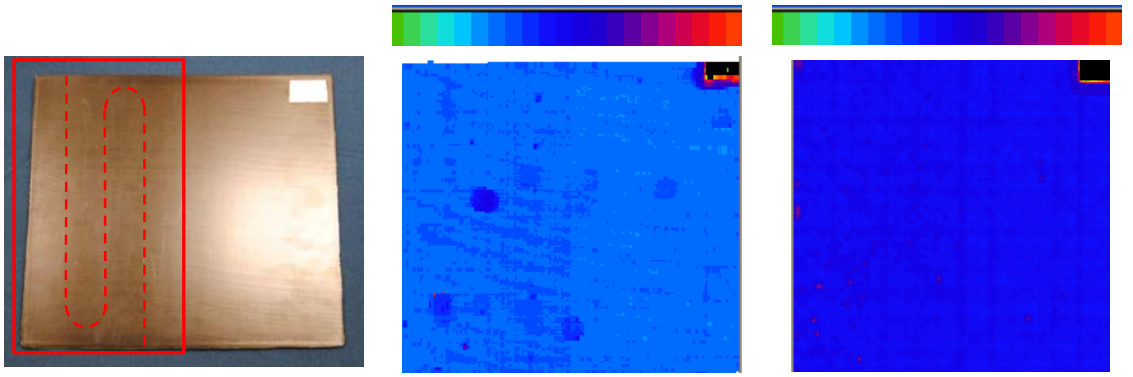

Tool Side

Ultrasonic Amplitude C-Scan (5 MHz Contact Probe)

Ultrasonic Amplitude C-Scan (5 MHz Through Transmission)

Figure 36. Embedded veil and FO NDI test panel with contact and through-transmission C-scans

In addition to UT C-scans, conventional A-scan amplitudes were compared on the NDI test panel. Representative A-scans from the veil and non-veil sides of the panel can be seen in figure 37. The scans indicate that there was very little loss of amplitude caused by the veil, but there was an additional signal reflected by the veil layer. This may have been caused by the lower fiber density and higher resin content in the layer.

A-Scan 1 – Veil Side

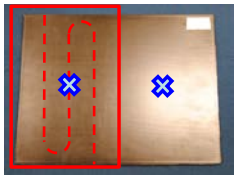

A-Scan 2 – No Veil Side

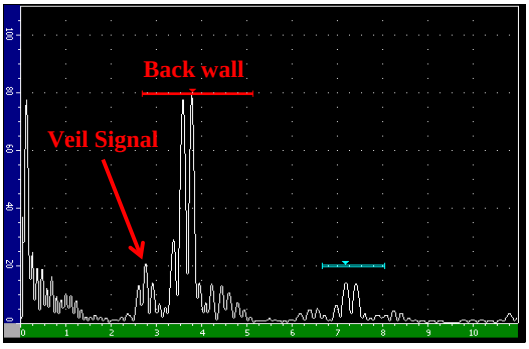

Fiber Optic-79% Amplitude

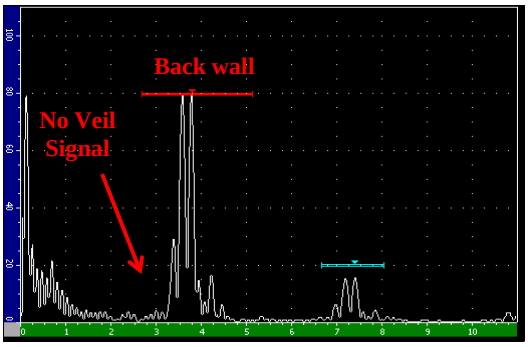

Non-Fiber Optic-80% Amplitude

Figure 37. A-scan showing amplitude of veil and non-veil side of test panel

Two fibers were embedded in one of the two full-scale fuselage panels. Each fiber had two egress points. The fiber layout can be seen in figure 38. Initially, the spatial resolution of the system was not known in these conditions. It was also unclear how large of a permanent residual strain change would be maintained in the carbon after impact and whether the impact would occur in the vicinity of a fiber. Because of this unknown, a 2″-spaced serpentine pattern of the fiber was used. There were approximately 130 ft. of FO embedded in the panel. Two egress locations on each fiber were used so that the fiber could be interrogated from either side in case there was a break in the fiber due to an impact or if a connector failed.

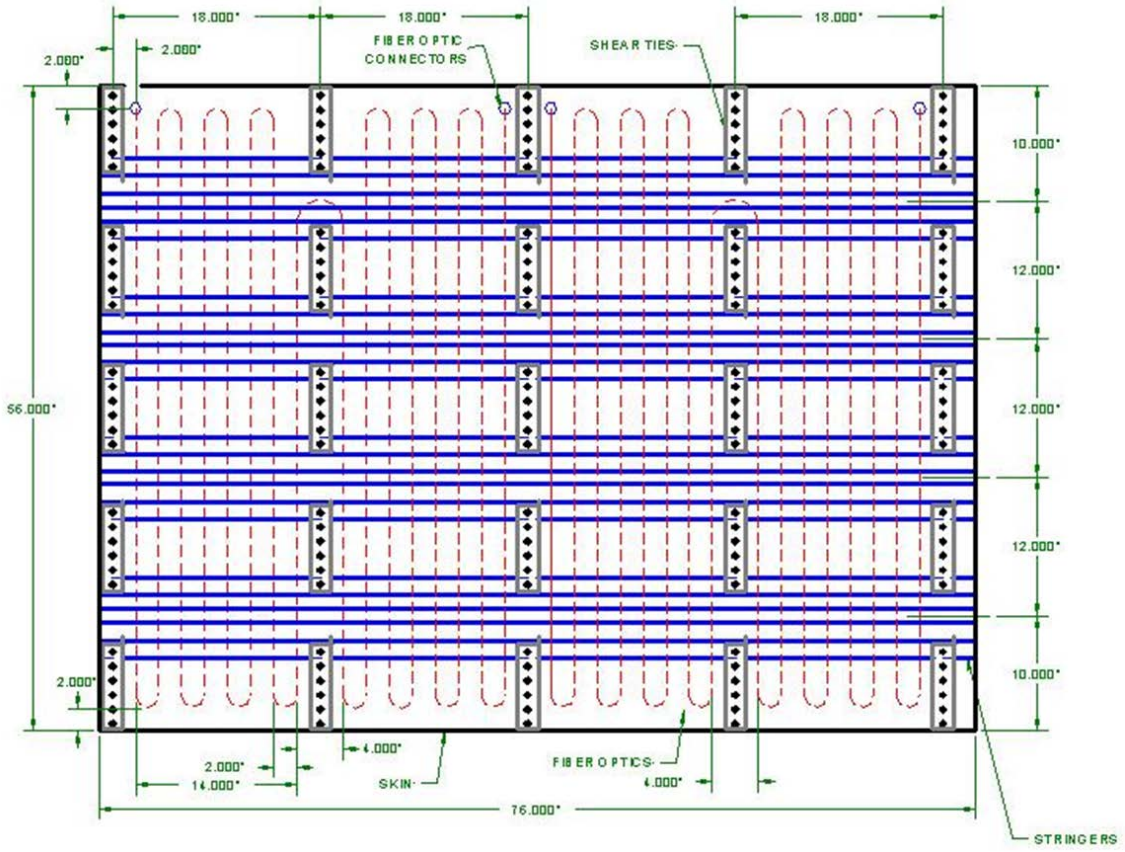

Figure 38. Embedded FO layout showing location of embedded fibers in panel A

To begin fabrication of the skin of the panel, the custom aluminum caul plate was cleaned and the first fiberglass cover ply layer laid down. The layup shown in figure 35 was then followed until the 11th ply was placed. Then, the veil with the FO attached was set in place. Figure 39 shows the carbon pre-preg being laid up on the caul plate to construct the skin.

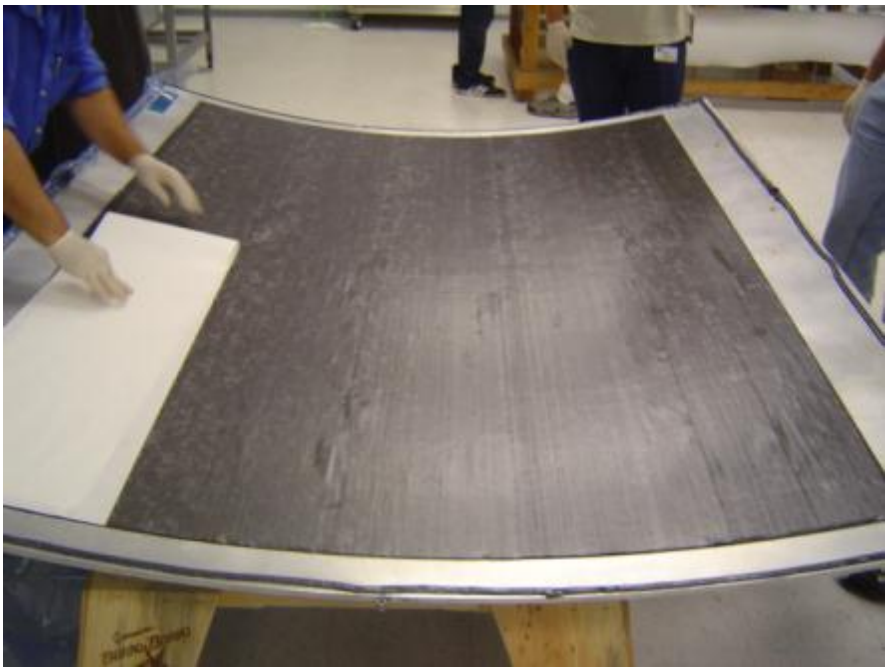

Figure 39. Carbon pre-preg skin plies being laid up on caul plate

The veil material was rolled out and pressed by hand to the room temperature. The position of the FO was verified and subsequent layers (plies) of carbon were placed. The two fibers, each attached to their own veil, are shown being placed on the layup in figure 40.

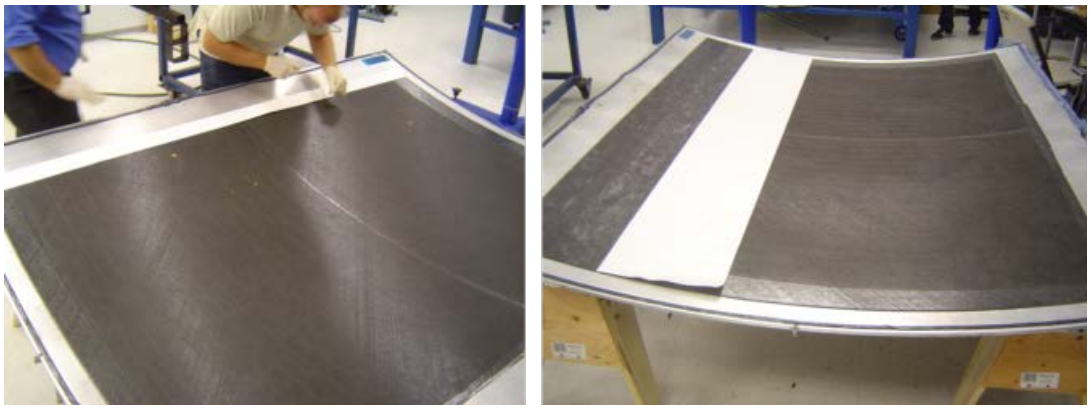

Figure 40. FO placed on skin layup and subsequent layer of carbon being applied

As described in the layup schematic of the panel, a vacuum debulk was performed each time four plies of carbon were placed. Release film was positioned over the pre-preg and then a layer of breather to properly distribute the vacuum pressure. At each debulk, approximately 506.5 Torr (20 inHg, 67.5 KPa) was applied for 20 minutes. The debulk process can be seen in figure 41.

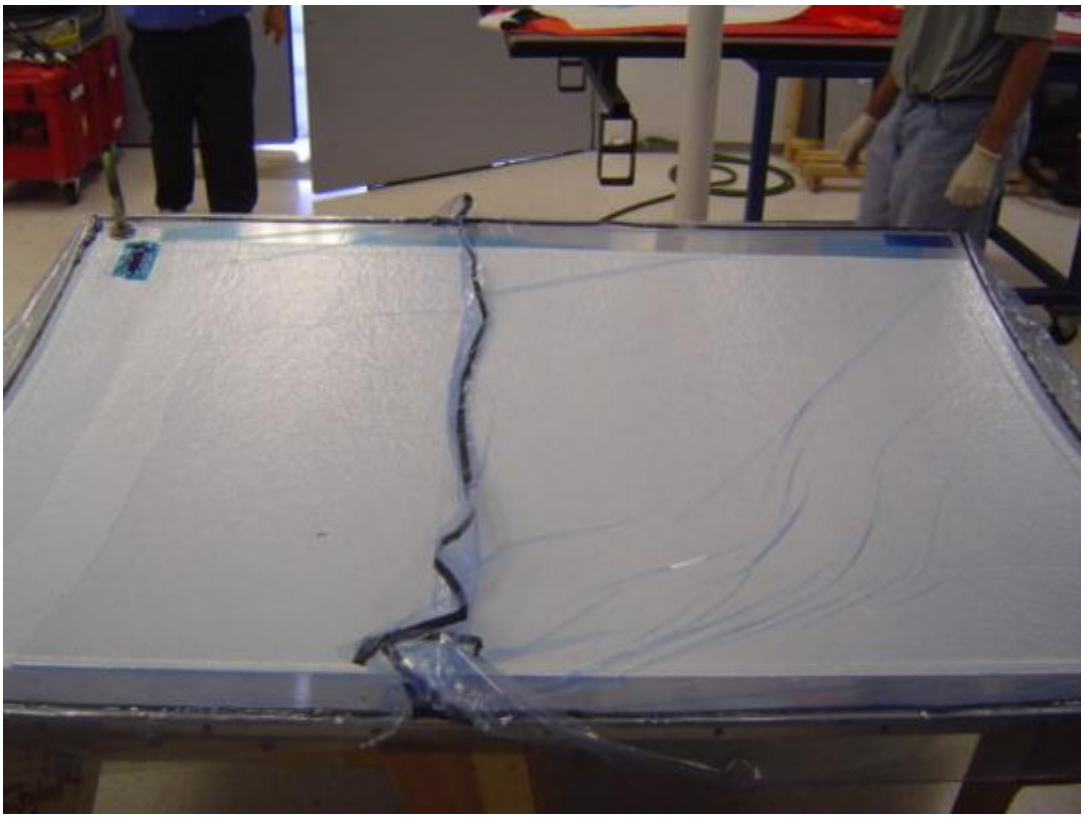

Figure 41. Skin layup bagged and being debulked

When all 16 plies of the skin were in place and debulked, silicone molds for the hat section stringers were placed. One of the silicone molds used for the hat section stringers (figure 42) is shown in figure 43. Four stringers, each 12″apart, were cured to each panel. The flange portion of the stringer was co-cured to the skin. The flange was 1.5″ long and tapered at a ply drop rate of two plies per 0.02″. Tapered stringers are used to provide better stress distribution at the stringer-to-skin interface, decreasing the chance of disbonding. They also help to minimize the shear stress that develops in the skin when an impact occurs near the edge of a stringer. There is also a tapered, built up section in the skin, under each shear tie, that consists of 12 additional plies. This is known as a pad build-up; it provides more material for fastening the shear ties to the skin.

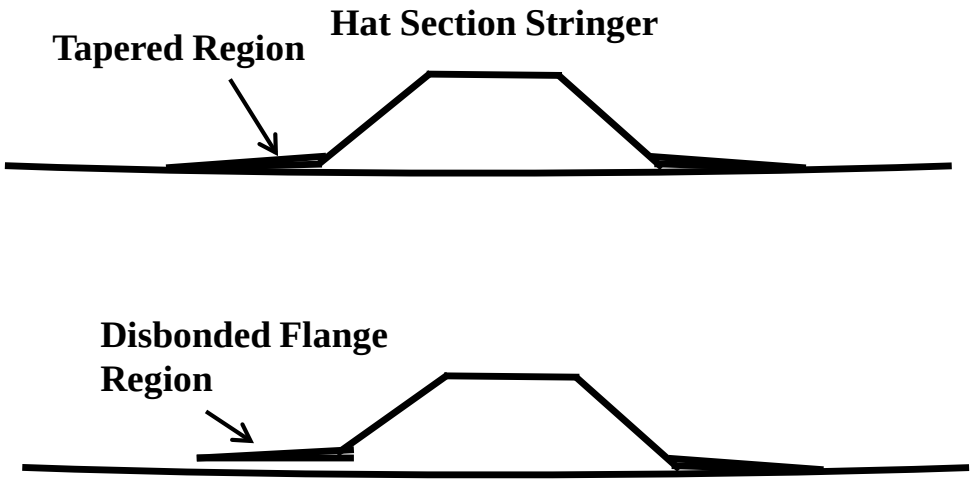

Figure 42. Tapered hat section stringer geometry and disbonded stringer flange example

Once the full layup was complete, a vacuum line was attached to the bagged part in a similar process to that which occurred during the debulk. A vacuum was applied to the panel and it was loaded into an autoclave (figure 43). A cure profile was then programed into the autoclave, which consisted of a heating and pressurization ramp. The temperature in the autoclave was raised 5°F per minute until a final temperature of 350°F was reached. This temperature was held for 2 hours and 20 minutes. Simultaneously, a pressure ramp was applied to reach a max external pressure of 90 psi, at which time the vacuum pressure within the bag was released to the atmosphere.

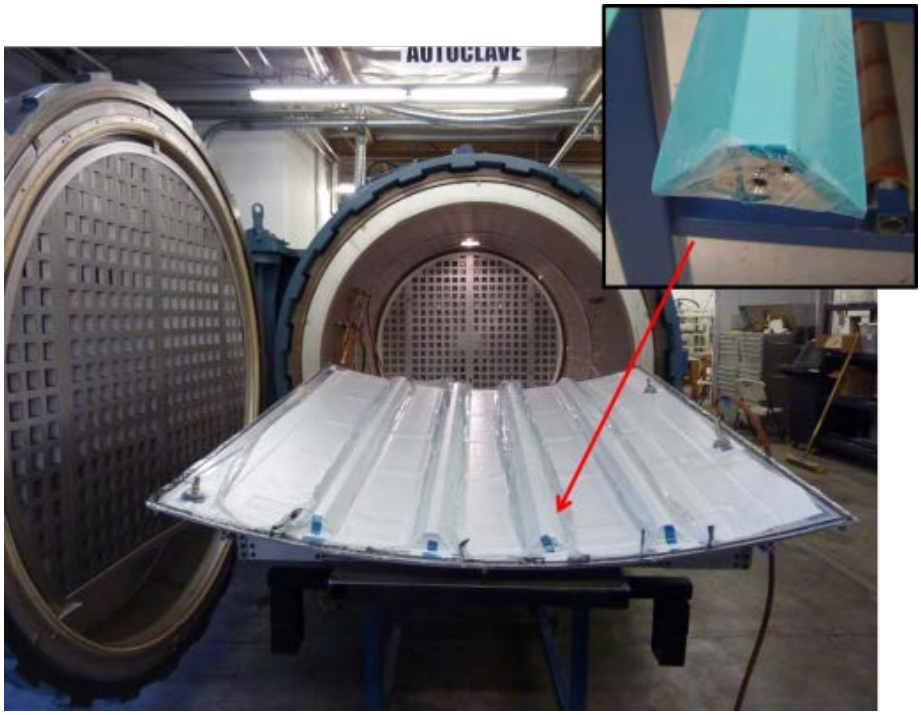

Figure 43. Autoclave and silicone stringer molds used to cure panels

3.4.3 Bonded FO

Two different methods of deploying FO strain sensing to the panels were investigated in this work: embedded and bonded. Embedding an FO in any composite structure would have to be performed during the manufacturing of the composite part. Also, embedding sensors or any type of material in the skin of an aircraft would have to be accompanied by stringent certification tests to show that the sensors do not degrade the structural integrity of the aircraft or affect any other part of the structure. For this and manufacturing reasons, applying sensors to the inside skin of the aircraft by means of surface bonding has more potential in the near future than embedded sensors. To bond the FO to the backside of the panel, three orientations of fiber layout were investigated:

1. Bonded to the panel perpendicular to the stringers with the fiber being bonded to each skin and stringer. This fiber had the same orientation and layout as the embedded fiber and was applied to all bays on panel B

2. Bonded to the backside of the panel to only the skin and parallel to the stringers (Bays 1 and 2 on panel A)

3. Bonded to the backside of the panel perpendicular to the stringers, but not bonded to the stringers, only the skins (bays 3 and 4 on panel A)

The surfaces of the backside of the panels were prepared and cleaned for bonding. When the panels were cured under high pressure in the autoclave, the breather material left a slight, rough indention pattern on the backside of the panels. This was lightly sanded down with 240 grit sandpaper to remove the bumpy cured resin. The surface was sanded, conditioned with M-Prep conditioner-A, then neutralized using M-Prep Neutralizer 5A. The process of conditioning and neutralizing on the sanded panel is shown in figure 44. The FO was then carefully laid out onto the prepared surface and taped with small pieces of Kapton tape to hold the fiber flush to the surface. To lay out the fiber on the backside of the panel, short lengths of fiber were unrolled from the spool and taped into place until the full serpentine pattern was laid out. M-Bond GA-2 strain gage adhesive was placed under the fiber with a syringe and squeegeed smooth around the fiber with a sponge.

Figure 44. Conditioning and neutralizing the backside of the panel for bonding FO lines

Figure 45 shows the fiber taped in place with a thin line of adhesive squirted under the fiber. The adhesive is being smoothed out with the sponge, removing any excess adhesive. Many small pieces of tape were needed to keep the FO in close contact with the surface of the panel. Laying out the fiber and bonding it to the surface in the three different orientations was a time-consuming and tedious process.

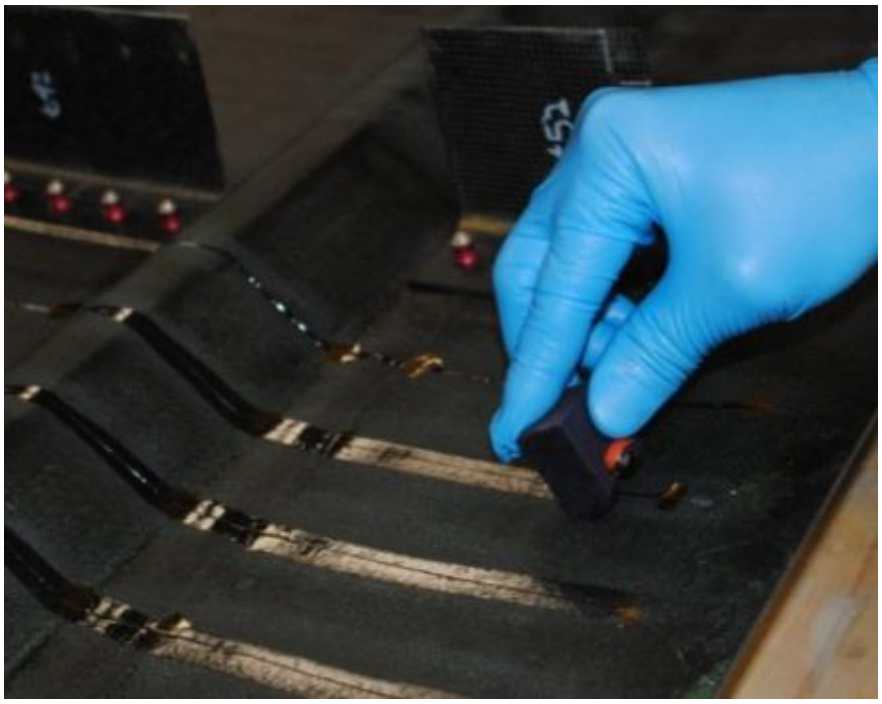

Figure 45. Thin line of M-bond GA-2 adhesive being squeegeed smooth around FO

Both the embedded and bonded FO needed to have connectors mated to the bare fiber. The process of splicing two fibers together involved using an FO cleaver to cut a flat end face perpendicular to the longitudinal axis of the sensing fiber. An FC connector with a short length of fiber already attached to the connector was cleaved and spliced to the sensing end. To join the two ends of cleaved fiber, a Fujikura Arc Fusion Splicer was used. After each splice was performed, the splicer unit analyzed the light attenuation loss based on the geometry of the splice. If this loss was greater than 0.1 dB, the splice had to be redone. The hardware used for these steps is shown in figure 46.

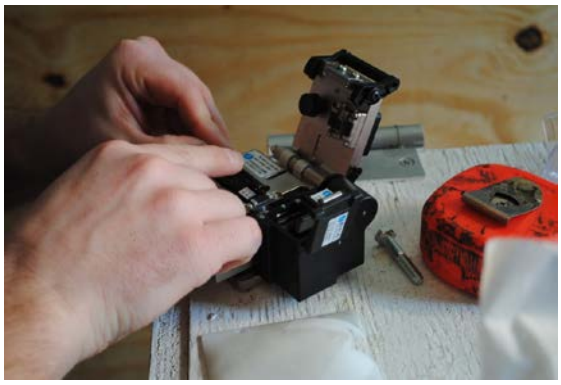

Figure 46. FO cleaver and Fujikura Arc Fusion Splicer

3.5 SHI TEST SETUP FOR THE FULL-SCALE PANELS

The impact test facility described in section 3.3 was used to impact test the full-scale test panels. First, the impact location of interest was identified and the panel lifted into place with a jack and set against the frame. The desired impact location was marked on the surface of the panel and a laser was shined down the barrel of the gun and matched with the marking on the panel. Clamps were used to secure the panel to the frame by clamping the frame sections of the panel to the support frame. A digital level was used on the face of the panel to ensure that the panel was perpendicular in both the horizontal and vertical directions to the trajectory of the simulated hail. Figure 47 shows a backside view of the panel clamped to the frame and ready for impact. The "X" in the figure indicates the impact location on the front side of the panel.

Figure 47. Panel supported with frame being prepared for impact test

Multiple impact scenarios were tested with high velocity simulated hail. Impact areas of interest are shown in figure 48 and consisted of:

- Mid-bay impact between shear ties and stringers (1)
- Stringer impact at start of stringer flange (2a)
- Stringer impact at center of stringer flange (2b)
- Stringer impact at end of stringer flange (on flange closest to mid stringer) (2c)
- Mid-stringer (between flanges under hat section) (3)

- Shear tie impact (4)

After each impact was induced, a visual inspection of the front and backside of the panel was performed. During the visual inspection, signs of damage to the surface of the panel—such as denting, chipping, and marring—were identified. On the backside of the panel, disbonding of the stringer flange-to-skin interface was inspected.

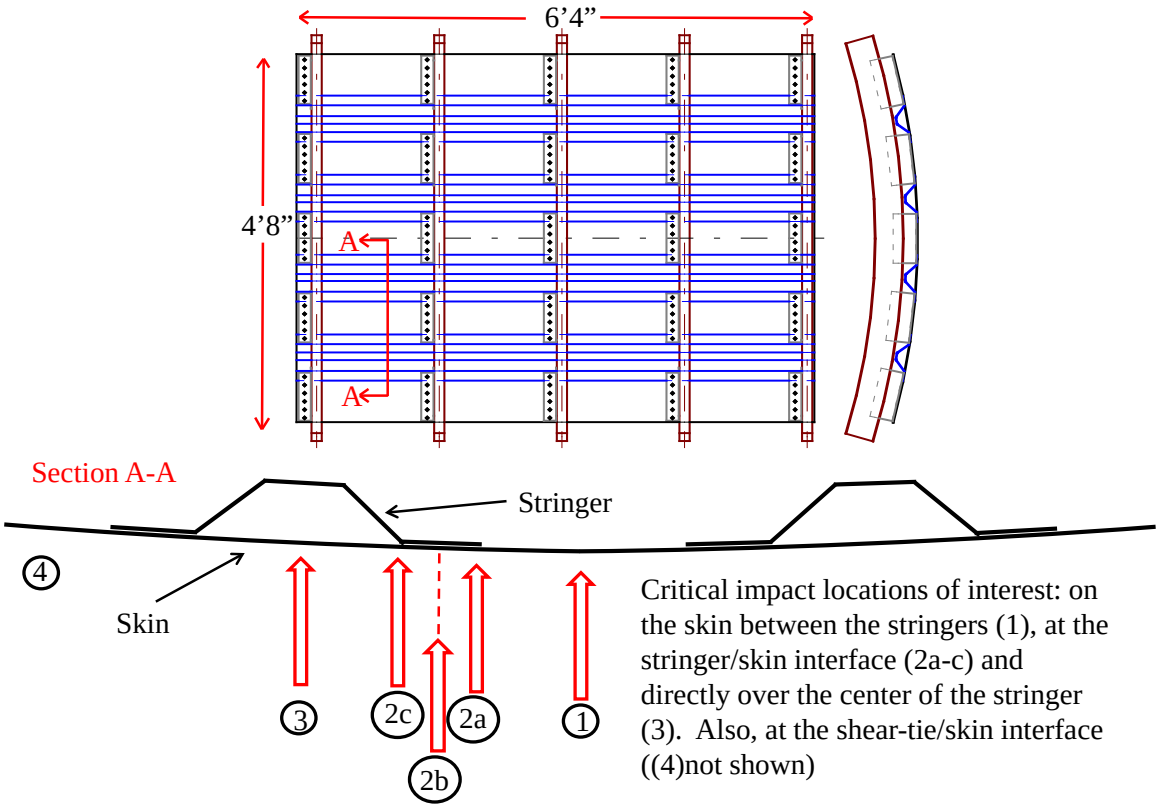

Figure 48. Panel showing impact areas of interest

To determine wheather the ice ball stayed intact during its trajectory, high-speed video was taken. Example high-speed images of an ice ball prior to and during impact are shown in figure 49.

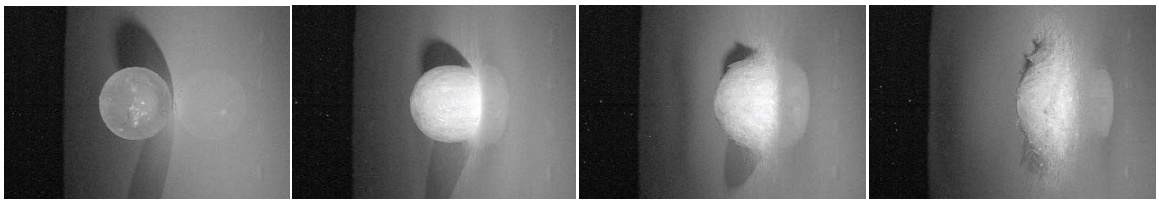

Figure 49. High-speed image of simulated hail impacting fuselage panel

After the visual inspection, a UT A-scan unit was used to determine the extent of damage, as shown in figure 50.

Figure 50. A manually deployed UT A-scan inspection being performed after impact to determine damage extent

There were 22 different locations on the two panels where ice impact testing was performed. The 13 ice impact locations that were conducted on panel A are shown in figure 51. The 14 ice impact test locations on panel B are shown in figure 52. The naming convention used to describe each impact is discussed in section 3.6.

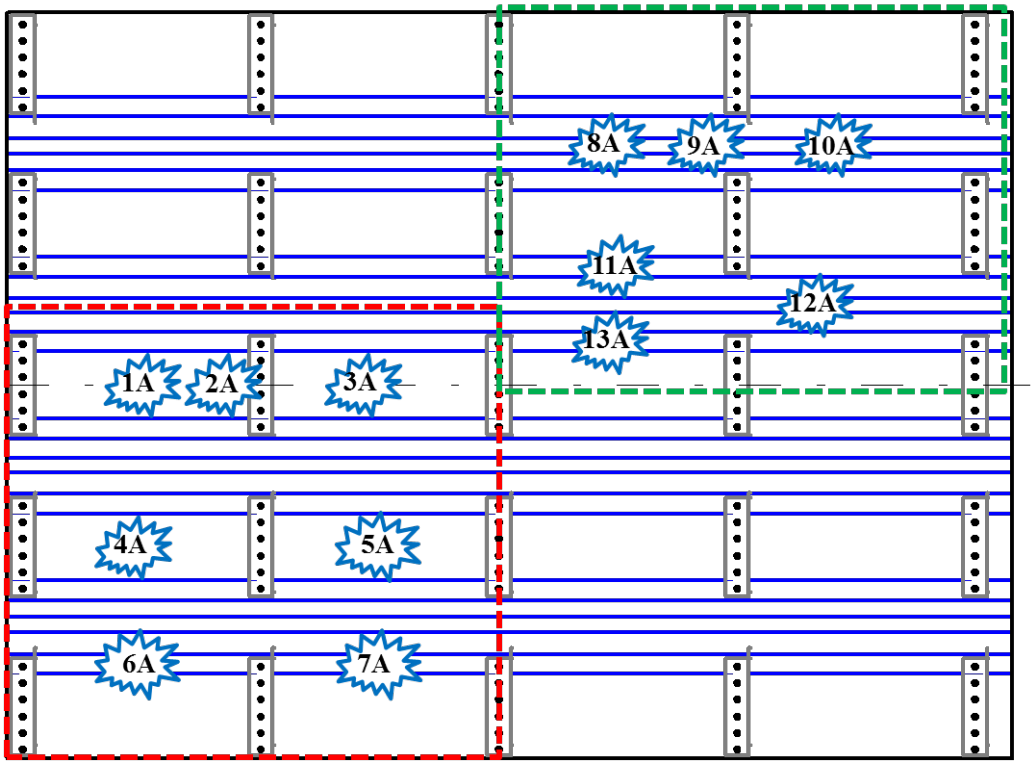

Bays 1&2 Ice Impacts

1A – B1-SK3-ST0-I1
2A – B1-SK3R-ST0-I1
3A – B2-SK3-ST0-I1
4A – B1-SK4-ST0-I1
5A - B2-SK4-ST0-I1
6A - B1-SK5-ST4-I2a
7A - B2-SK5-ST4-I2a

Bays 3&4 Ice Impacts

8A – B3-SK0-ST1-I3
9A – B3/4-SK0-ST1-I3
10A - B4-SK0-ST1-I3
11A - B3-SK2-ST2-I2b
12A – B4-SK0-ST2-I3
13A –B3-SK3-ST2-I2b

Figure 51. Ice impact test locations on panel A

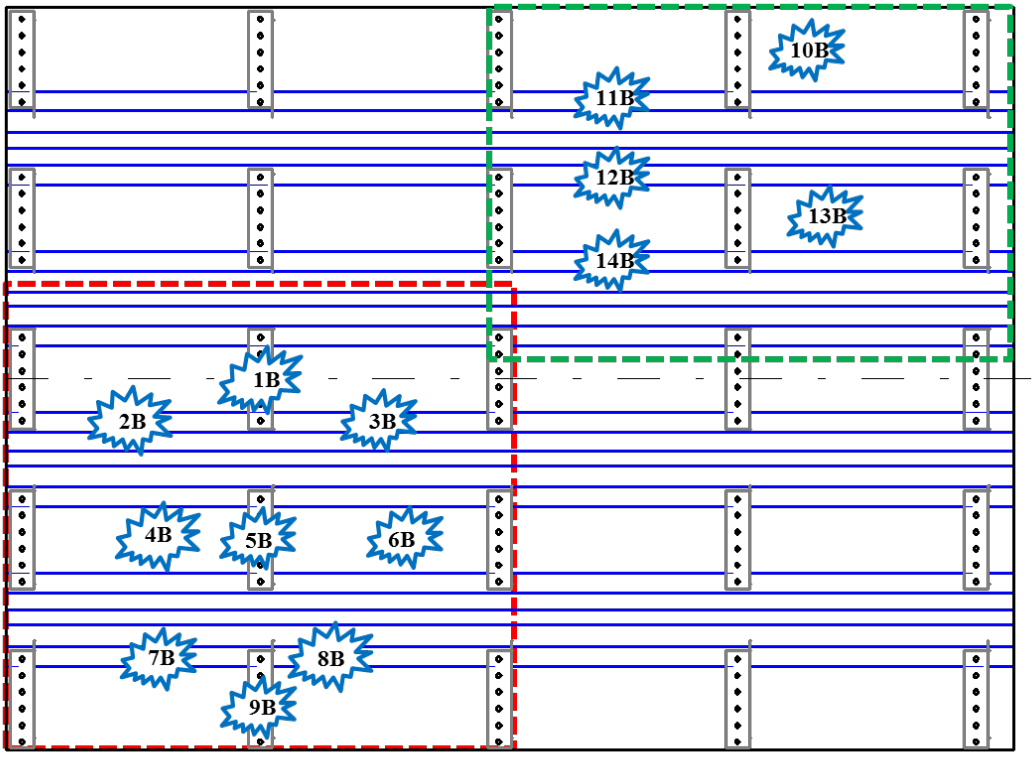

Bays 1&2 Ice Impacts

1B – B1/2-SK3-ST0-I4 – b7
2B – B1-SK3-ST3-I2b – b8
3B – B2-SK3-ST3-I2a – b9
4B – B1-SK4-ST0-I1 – b1
5B – B1/2-SK4-ST0-I4 – b6
6B – B2-SK4-ST0-I1 – b2
7B – B1-SK5-ST4-I2a – b4
8B – B2-SK5-ST4-I2a – b3
9B - B1/2-SK5-ST0-I4 – b5

Bays 3&4 Ice Impacts

10B – B4-SK1-ST0-I1 – b11
11B – B3-SK1-ST1-I2b – b12
12B – B3-SK2-ST1-I2a – b13
13B – B4-SK2-ST0-I1 – b10
14B - B3-SK2-ST2-I2b – b14

Figure 52. Ice impact test locations on panel B

3.6 SPHERICAL TIP DROP WEIGHT IMPACT TEST SETUP

To simulate impact damage related to ground-based equipment, a drop weight, spear-type impact device was designed and fabricated. The intention of these tests was to induce varying levels of damage on the panels created by hard, spherical-tipped impacts and was applied only to full-scale test panels. The intended levels of damage ranged from almost nonexistent to fairly severe.

The hemispherical shape was selected to represent a generalized solid object impacting the skin of the panel. A 2″ diameter, spherical impact tip was selected to test panel A. The drop spear was constructed using a ¾″ to 10″ threaded rod. The threaded rod was used so that the weight of the spear could be easily adjusted using large washers secured to the rod with nuts. A 10′-tall pipe was used to guide the drop spear to its target. Two larger diameter aluminum guide washers were fabricated with a diameter that was 1/8th″ smaller than the inside diameter of the guide tube. The guide washers were sized to minimize rattling during the spear descent into its target. A smooth, sanded radius was integrated on the outside edge of the guide washers to minimize frictional energy loss. Figure 53 shows the drop tube and spear with the 2″ diameter impact tip.

Figure 53. Guide tube, drop spear with 2″ diameter impact tip, and quick release mechanism

To raise the drop spear to the desired height of impact, a steel cable loop was attached to the top of the drop spear. A quick release mechanism attached to a cable was run through a pulley secured above the top of the guide tube and attached to a manual winch. The quick release was attached to the drop spear through a rectangular access hole in the guide tube. The drop spear was suspended

at the intended distance from the panel in the center of the drop tube. A string was run down through the top of the tube to the quick release. This is also shown in figure 53. Prior to each drop test, the tube was checked for vertical level to ensure the spear did not slide along the side of the tube.

To secure the panel during impact testing, a steel frame was fabricated using 1″ x 2″ steel tubing. The frame was welded together with two supports clamped to each frame on the panel at 10 locations. Angled stiffeners were added to prevent any horizontal movement during impact testing. A picture of panel A clamped to the mounting fixture is shown in figure 54. The vertical runs of bonded fiber can be seen in the lower left side of the figure. The horizontal runs of fiber can be seen in the upper right corner.

Figure 54. Panel A clamped to the steel frame for drop weight impact testing

Each impact was performed perpendicular to the surface of the panel. Two brackets, one on each side of the frame, were used to secure the panel at the required angle to keep the impact site perpendicular to the spear guide tube. The two brackets clamped to the frame are shown in figure 55.

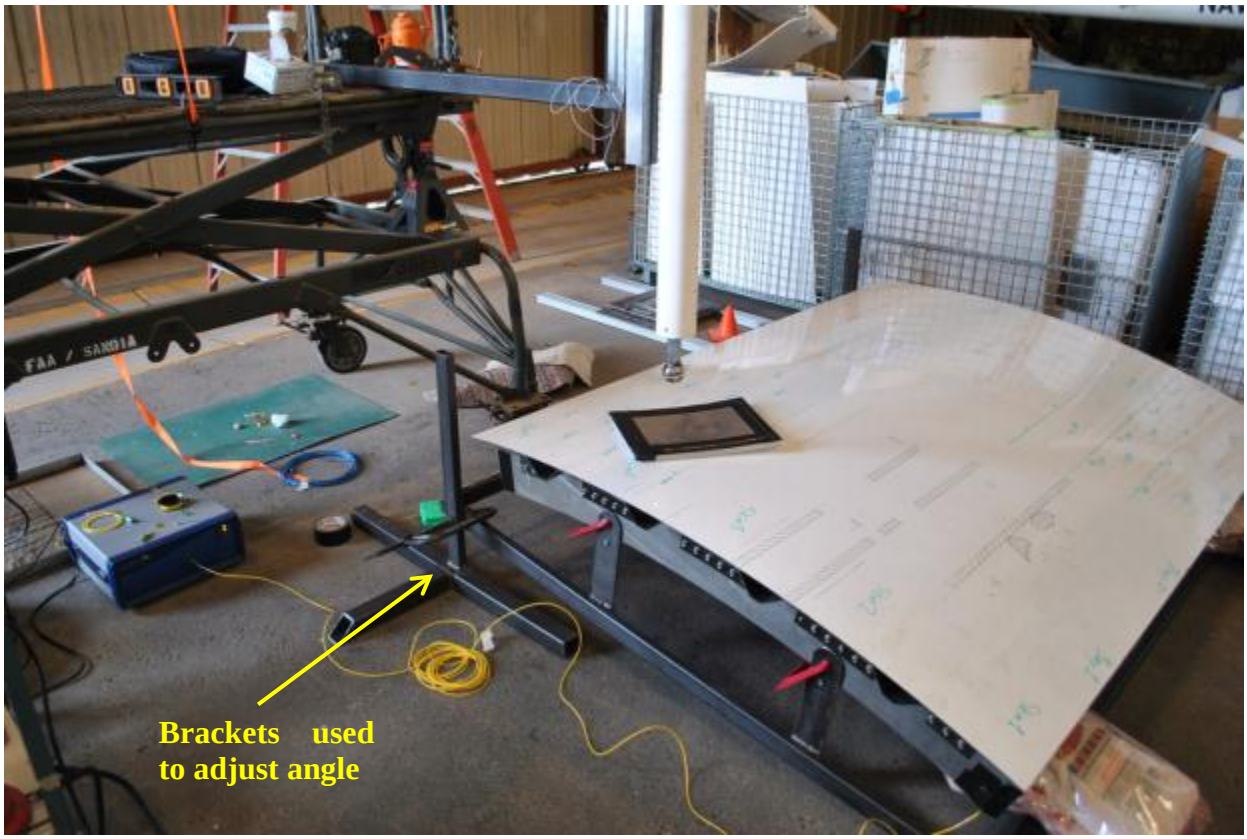

Figure 55. Panel A set up for drop weight impact testing

Impact locations for the steel, spherical tip impacts that were performed on panel A are shown in figure 56. There were 43 spherical tip impacts performed on the panel.

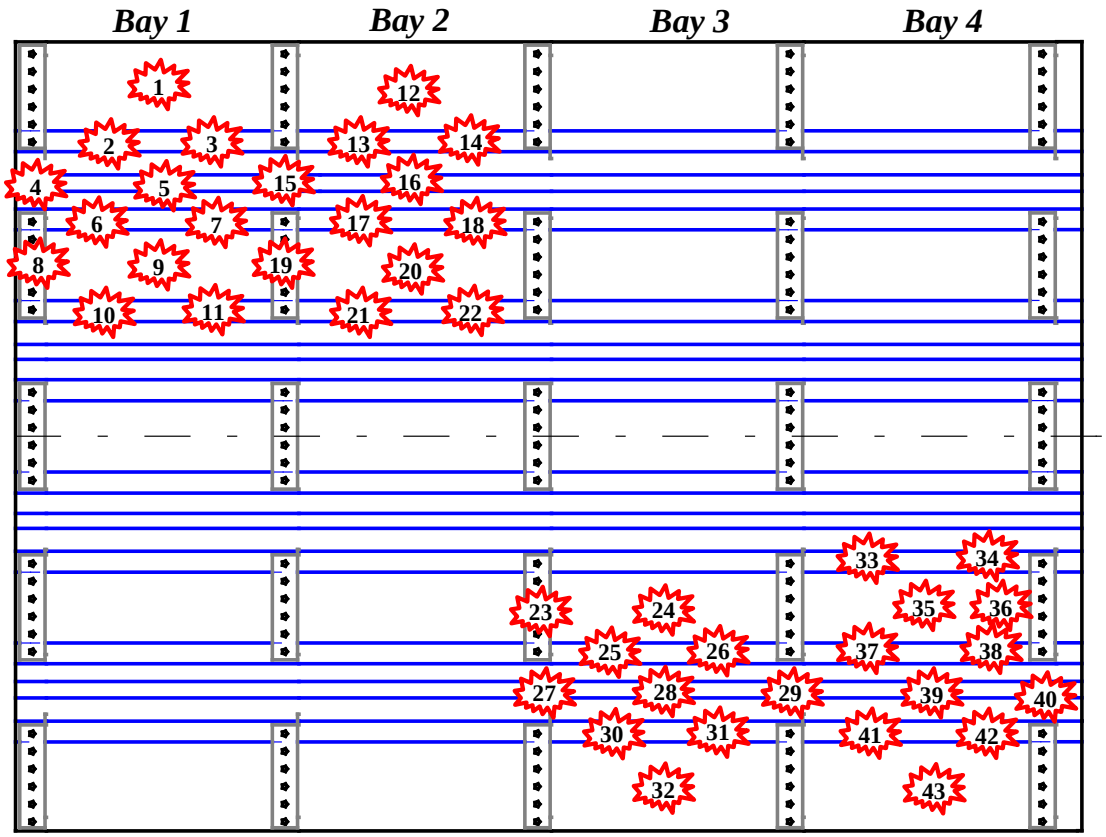

Figure 56. Impact locations for steel, spherical tip impacts

4. RESULTS AND DISCUSSIONS

4.1 DAMAGE CHARACTERIZATION ON COMPOSITE PLATE STRUCTURES

Damage characterization on the composite flat plates was achieved through the use of various NDI methods. To assess the various methods of NDI used in this study, impact damage generated on the panels ranged from below the FTE to barely visible impact damage. These terms are discussed in section 2.3. A total of 81 panels were impact tested in this study. The breakdown of test panels is detailed in table 5.

Table 5. Number of flat plate panels tested

Flat Plates - Impact Test Summary - Simulated Hail Number of Panels Inspected		
Structure Type	Hail Diameter (mm)	Number of Samples
8-Ply Flat Plate	38.1	10
	50.8	7
	60.1	7
16-Ply Flat Plate	38.1	12
	50.8	8
	60.1	11
24-Ply Flat Plate	38.1	7
	50.8	10
	60.1	9

The failure criterion being considered to determine FTE was delamination. To determine whether a delamination had occurred after impact, the panel was inspected using various methods of UT. Example inspection results of impact damage generated at energy levels spanning the FTE of the 8-, 16-, and 24-ply panels are shown in figures 57–59. Inspection results from all 81 panels inspected can be seen in appendix A and are separated by panel thickness.

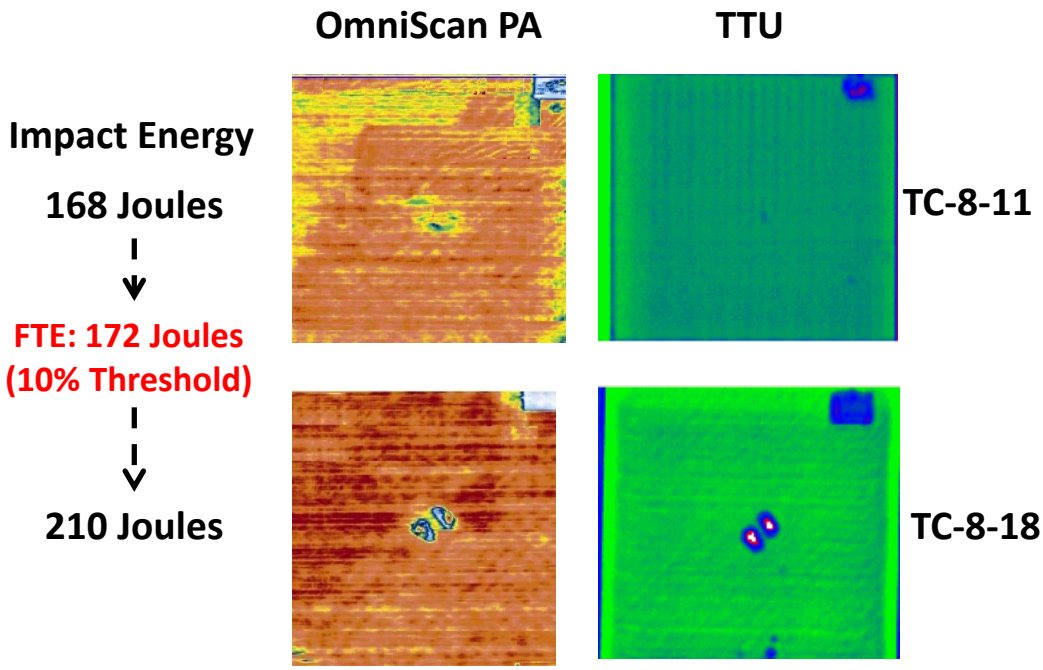

Figure 57. UT phased-array and through-transmission results of two 8-ply panels spanning the FTE for 38.1 mm simulated hail

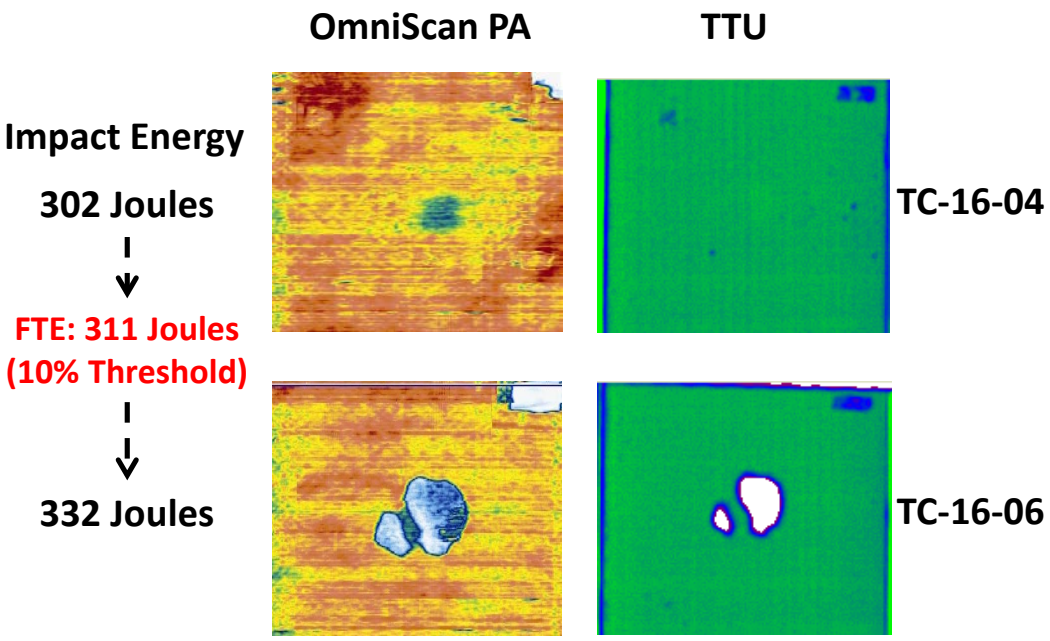

Figure 58. UT phased-array and through-transmission results of two 16-ply panels spanning the FTE for 38.1 mm simulated hail

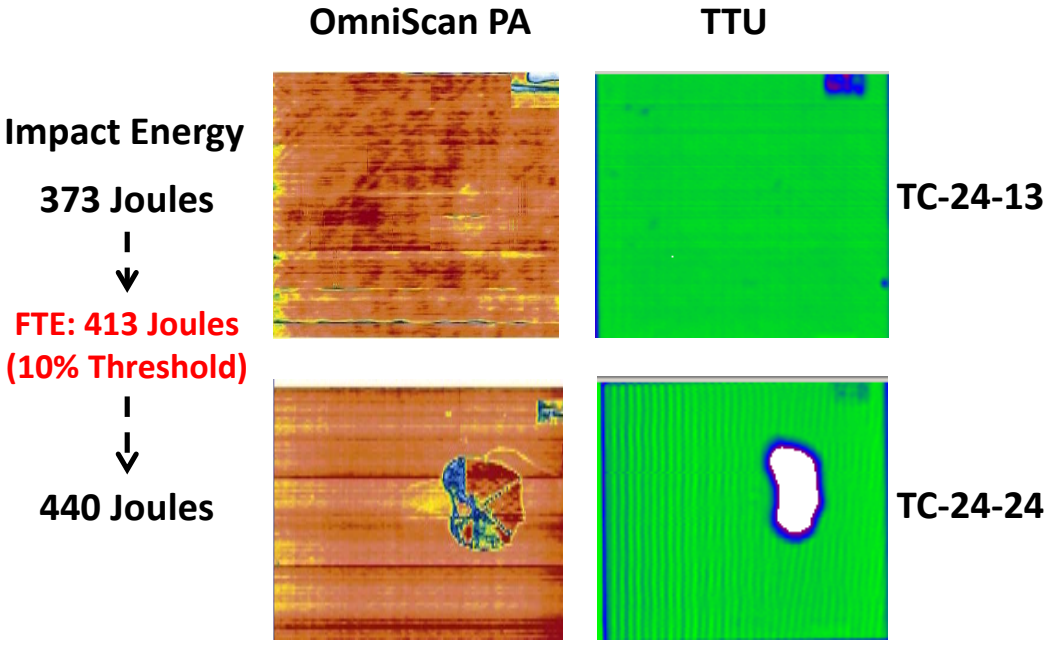

Figure 59. UT phased-array and through-transmission results of two 8-ply panels spanning the FTE for 38.1 mm simulated hail

4.1.1 UT Damage Detection

4.1.1.1 Single-Element and PA-UT Inspection

After each impact test was performed, a hand-deployed 5 MHz UT transducer was used to determine whether damage was induced during the impact. If the desired level of damage was not obtained, the panel was impacted again—up to three times. Typical signal changes of interest to determine whether the onset of damage had occurred were loss of and shift in back wall signal.

The OmniScan MX was use to inspect all 81 of the flat plate panels with a 0.25″ diameter, 5 MHz single-element transducer with a delay line on the Olympus X-Y glider. The setup used is shown in figure 60. The transducer was indexed at 0.125″ (half the transducer diameter) over the entire panel to produce a C-scan.

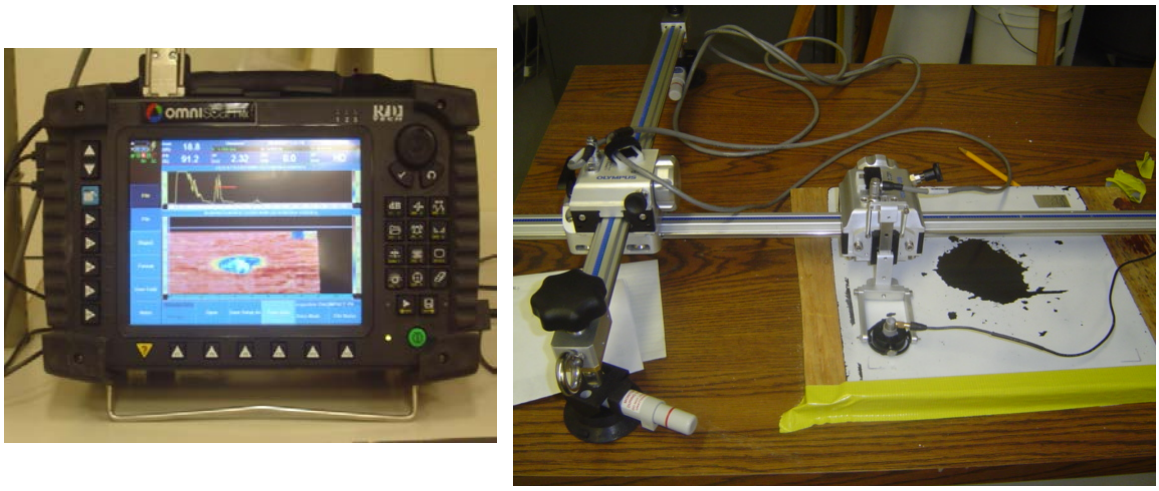

Figure 60. OmniScan 5 MHz single-element inspection setup

The OmniScan MX was also used to deploy the 10 MHz, 10L64 phased-array probe used to inspect all the panels. To enhance signal clarity, an Olympus water box was used. The typical A-scan setup used to compose C-scan images is shown in figure 61. Resulting phased-array and single-element C-scan results are also shown. It can be seen that the clarity and resolution of the phased-array inspection is much better than that of the single-element transducer. This is because of the scanning or indexing distance used to inspect the panel with the single-element transducer. These panels were inspected with a manual scanner at 0.125″ index spacing, which is larger than the pitch/spacing of the elements in the array probe. The single-element transducer used was a 5 MHz probe. The PA probe was a 10 MHz unit, which also contributed to the resolution differences.

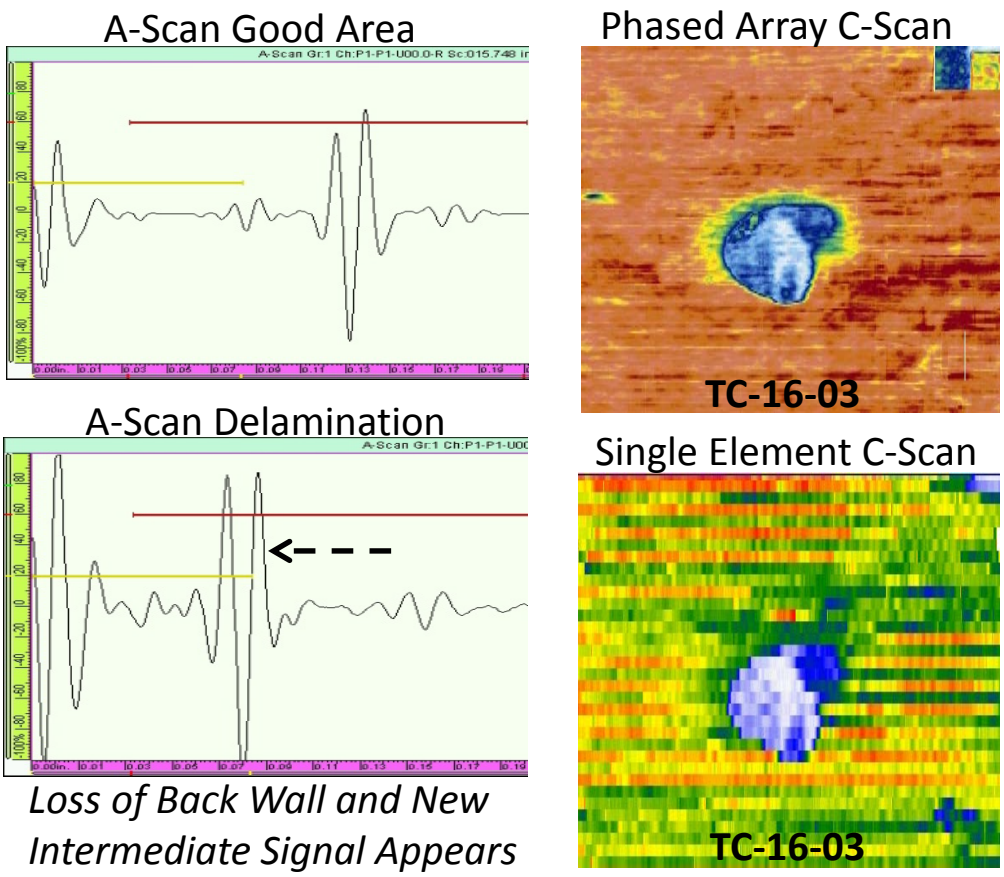

Figure 61. Typical OmniScan A-scan setup used to compose C-scans and resulting phased-array and single-element C-scan images for a select panel

Damage area was determined using several of the UT deployment methods, including the OmniScan phased array. Damage area was estimated using the limited measurement features available in the unit's software, which were comprised of the ability to measure the distance between two points. This was used to estimate the best-fitting shape to the damage. An example of this is shown in figure 62. It is important to note that the damage area or affected zone where there was a decrease in amplitude was used to estimate the damage area with this technique. This area of decreased amplitude was typically seen around the edges of the delamination and most likely consisted of microcracking in the matrix material. This is discussed further in section 4.1.5.

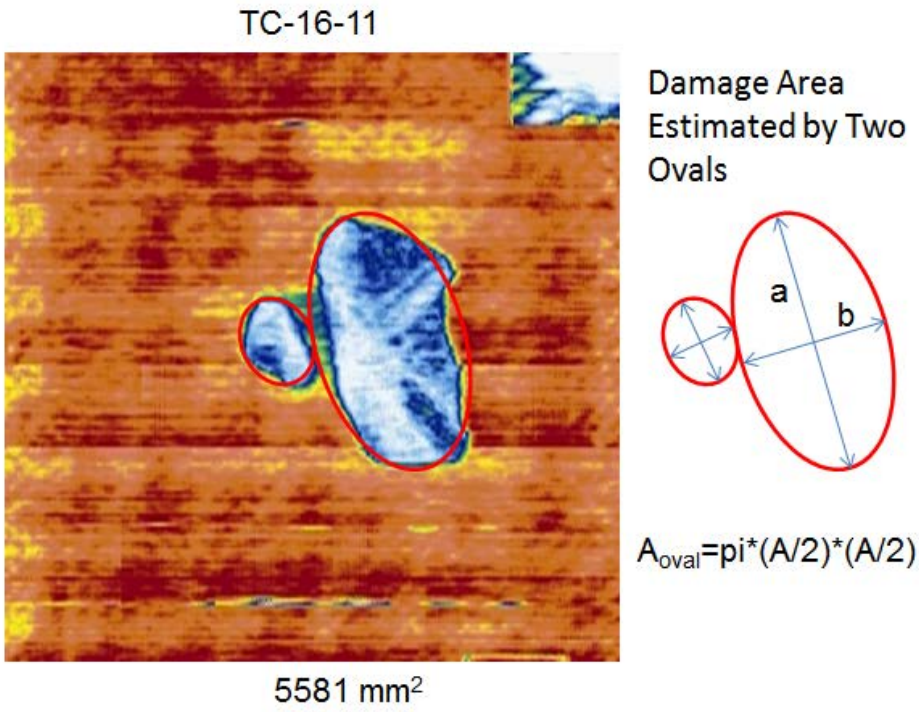

Figure 62. OmniScan phased-array damage area measurement example

In addition to assessing damage based on A-scans and amplitude C-scans, TOF, or depth scans, are also beneficial to assess the level of impact damage. Figure 63 shows an example of a depth scan acquired using a 3.5 MHz phased-array probe on the OmniScan MX. It can be seen in the figure that by using a good color pallet, the depth of delamination on different plies can be identified. By using the thickness of the plies in the laminate and the depth reading indicated in the C-scan, one can determine at what ply depth the ply splitting occurred. Accurately determining the depth of damage is critical when scarfing plies in preparation for a repair.

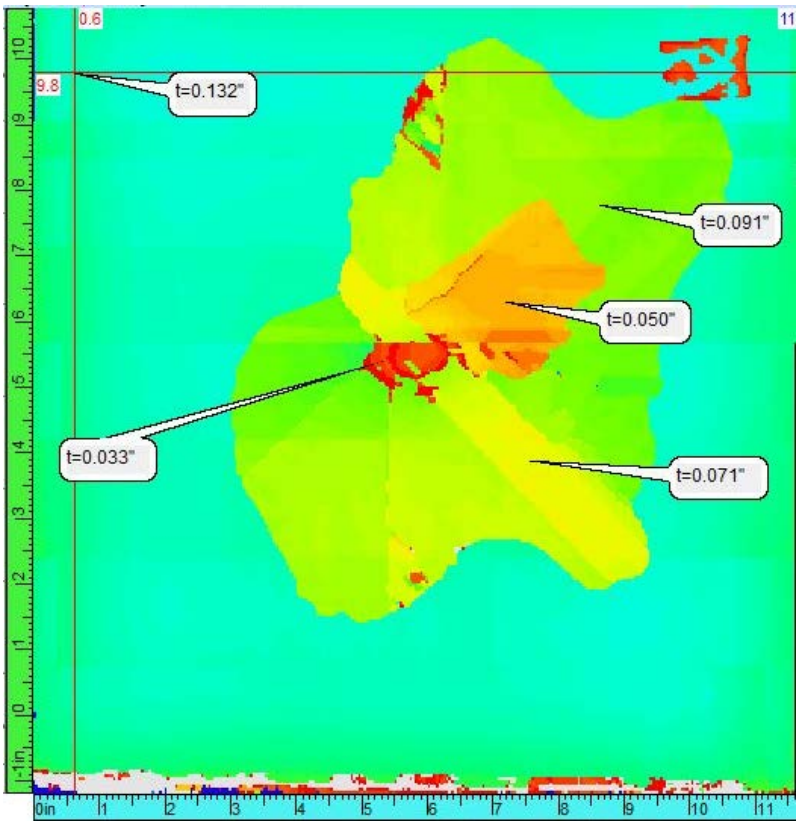

Figure 63. OmniScan phased-array TOF C-scan

The Boeing MAUS V system was used to inspect all the panels with both single-element pulse echo and resonance inspection. It was also used to inspect select panels with low-frequency bond tests (LFBT) and mechanical impedance analysis (MIA). This is discussed in section 4.1.2. For UT testing, a 0.25″ diameter, 5 MHz transducer with a delay line was used. The setup used to inspect the panels is shown in figure 64.

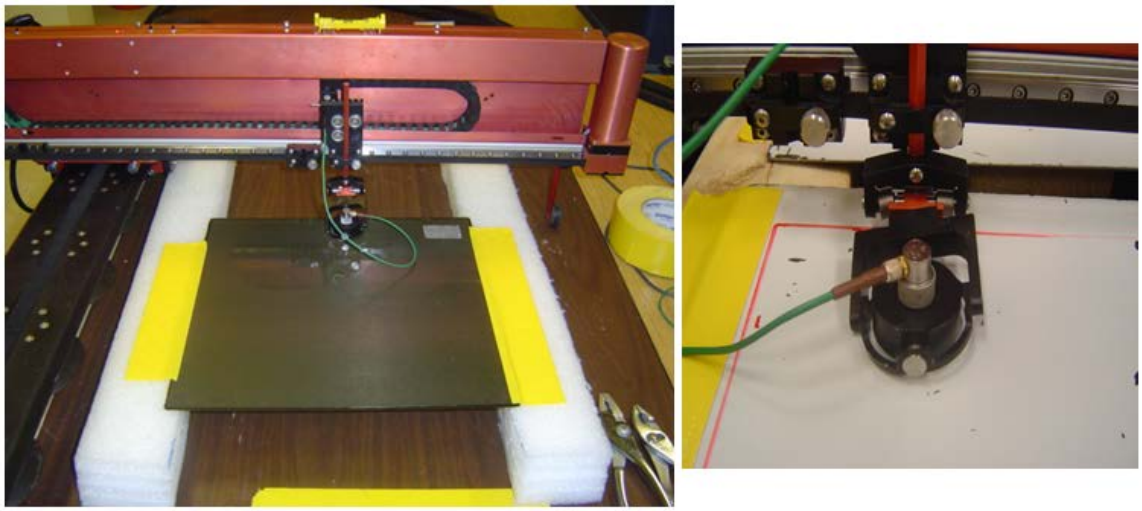

Figure 64. Boeing MAUS V pulse-echo setup used

Damage area was calculated for each panel using the MAUS V system. This was performed using the internal measurement capabilities of the system. After a scan was performed and the color pallet adjusted for optimum damage resolution, discrete line segments were traced around the damage. The area contained within the line segments was then reported by the system. An example damage area measurement is shown in figure 65.

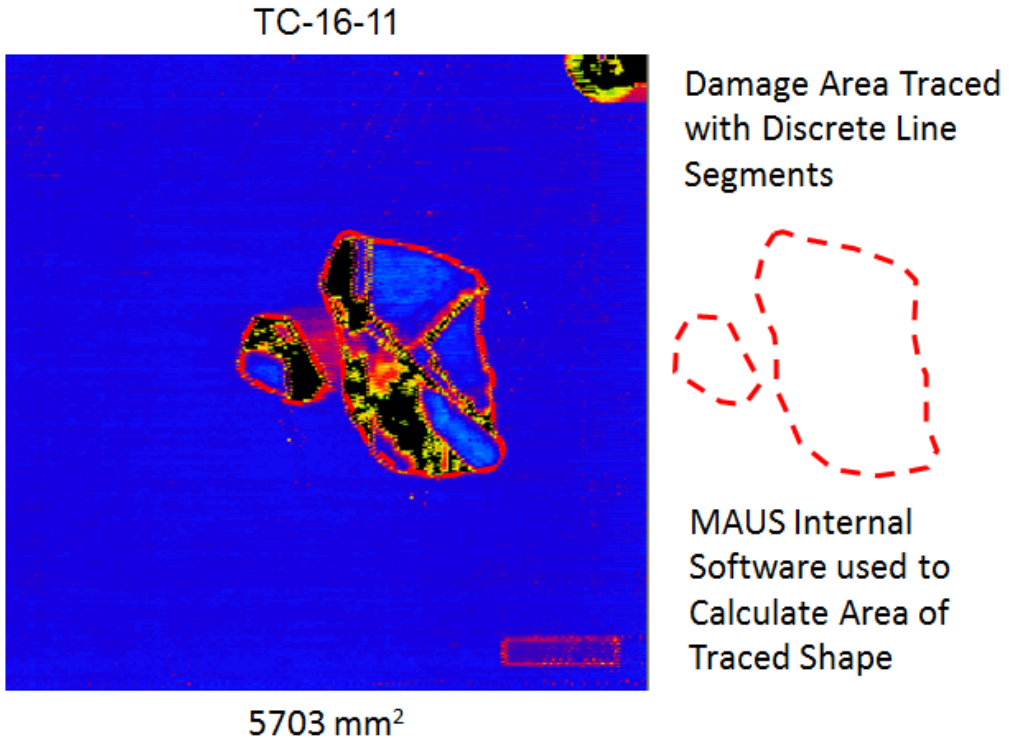

Figure 65. The MAUS V single-element damage area measurement example

4.1.1.2 Through-Transmission UT

All the panels were inspected with both 5 MHz and 1 MHz TTU inspection. The 1 MHz TTU inspections were performed at Sandia using 0.5″ diameter submersible transducers with a 0.030″ indexing resolution. The UT software used was UltraWin, a 32-bit Windows® data acquisition, imaging, and analysis software system from NDT Automation. The UT tank and an example C-scan are shown in figure 66. An example A-scan and settings screenshot are shown in figure 67.

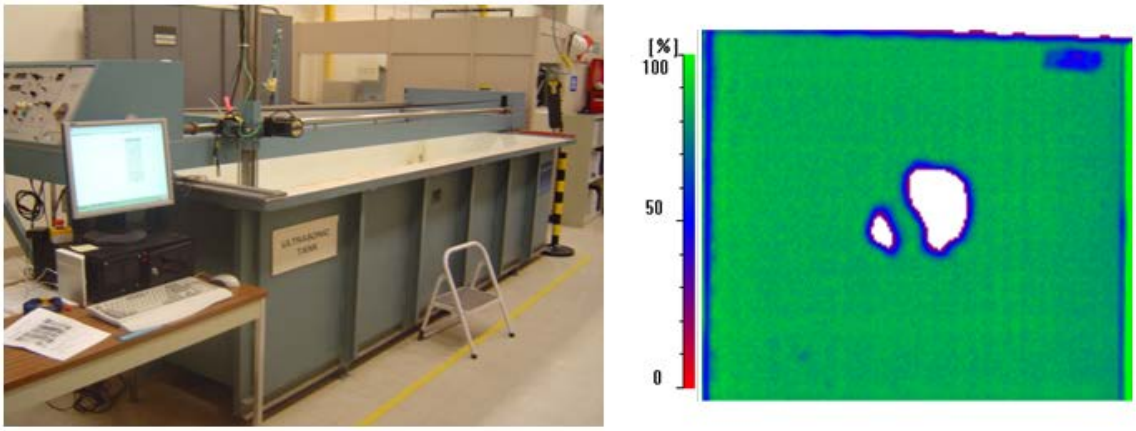

Figure 66. UT tank used at Sandia for TTU inspection and example C-scan result (TC-16-6)

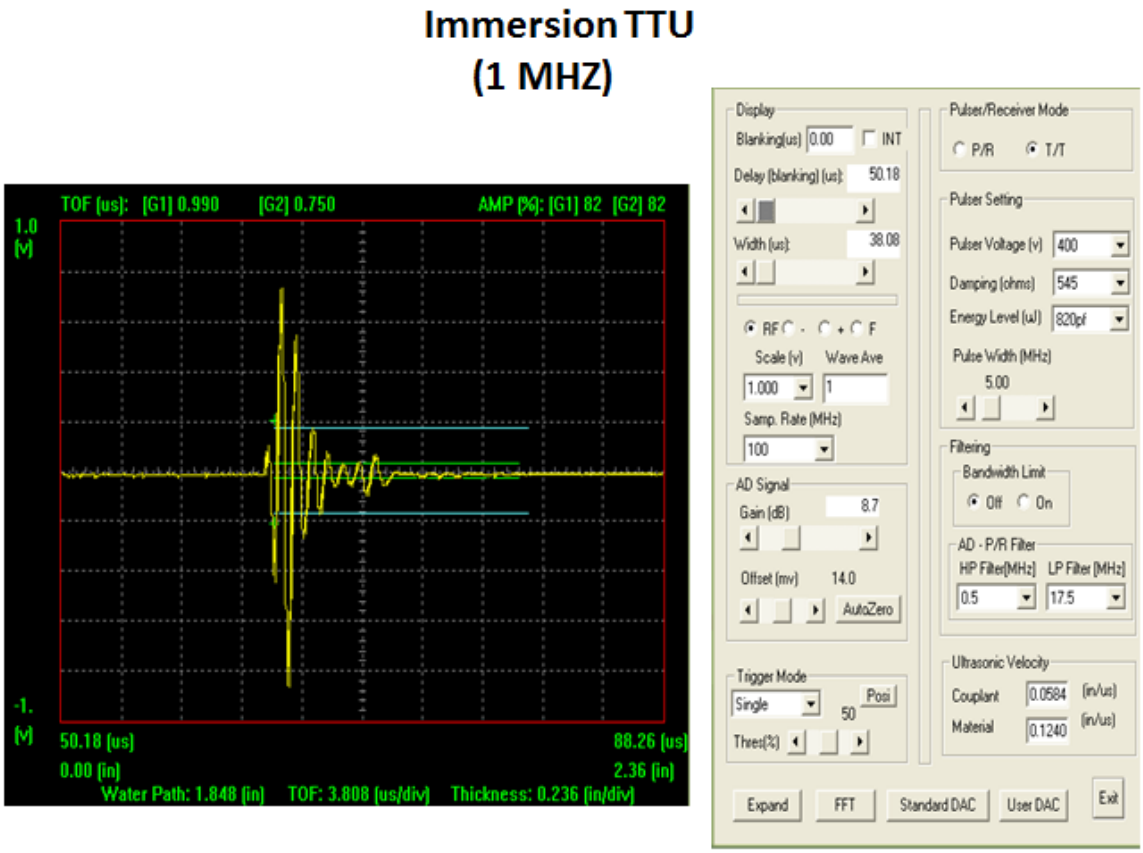

Figure 67. A-scan example from TTU inspection and settings screenshot

After impact testing, each panel was removed from the fixture and inspected using an immersion UT C-scan tank at UCSD. The system was a Physical Acoustics UltraPac II system with 5 MHz transducers in through-transmission mode, which produced a two-dimensional C-scan. A 1 mm indexing resolution was used to obtain a map of the damage contained in the panels. The total damage area was calculated based on a 95% threshold of signal amplitude transmission loss [16]. The system used, and an example C-scan, are shown in figure 68. This system was used to determine the delamination area induced by each impact presented in section 4.1.5.

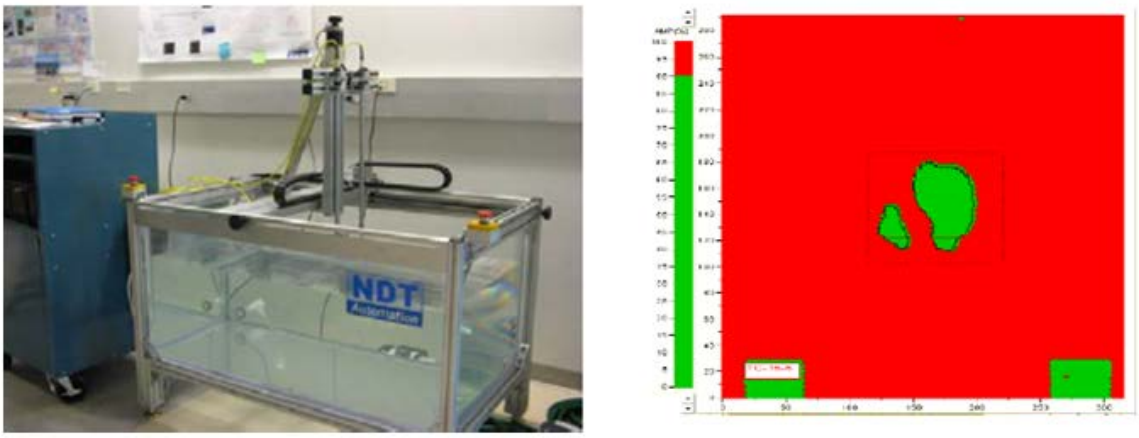

Figure 68. UT tank used at UCSD for TTU inspection and example C-scan result (TC-16-6) [16]

4.1.2 UT Resonance Damage Detection

Resonance testing was performed using the MAYS V system. A 330 KHz resonance probe was used by initially calibrating the transducer on an area of the panel that had no defect. The probe was then nulled, or zeroed, to establish a baseline signal and the scan was performed. Figure 69 shows an example of a resonance C-scan inspection result compared to TTU on a 16-ply impact panel. The resonance inspection technique was applied to all flat plate impact panels and results for all panels are shown in the appendix. Typically, resonance inspection provided similar results to PE-UT.

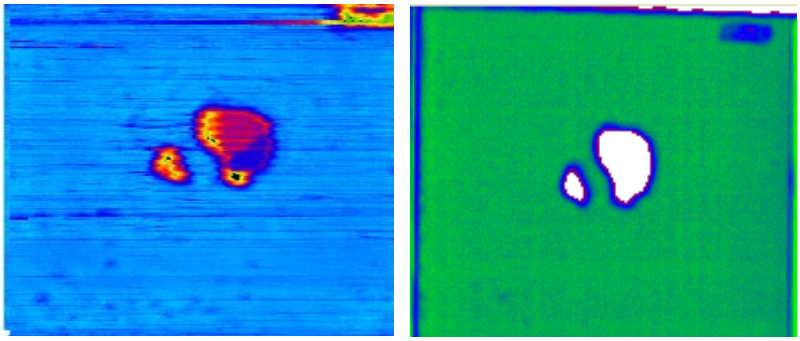

Figure 69. Example resonance inspection results compared to TTU (TC-16-6)

4.1.3 Pulse Thermography Damage Detection

Pulse thermography was applied to all 81 test panels. For this setup, the hood was positioned vertically over the samples, as shown in figure 70. A 10 microsecond pulse of heat was applied to the surface of the sample and the IR camera recorded the thermal response from the surface of the panel. The TWI system used was a commercially available flash thermography system, which uses two xenon flash tubes to supply heat to the surface of the composite sample. The panels were

painted with removable mat black paint, then flashed at 75% power. The test coupons were left to cool and the temperature responses were recorded by the IR camera, which recorded the data for approximately 6–9 seconds, depending on the thickness, at 60 Hz. The data were then post-processed with TWI's TSR processing technique using MOSAIQ 4.0 software. The best image in the sequence with the highest thermal contrast was used for the analysis. Time versus temperature plots were analyzed to assess the damage to the panel, and a mask was applied, as shown in figure 71. To perform this, markers were placed in a known good area and a suspect damage region to view the time versus temperature curve at specific points.

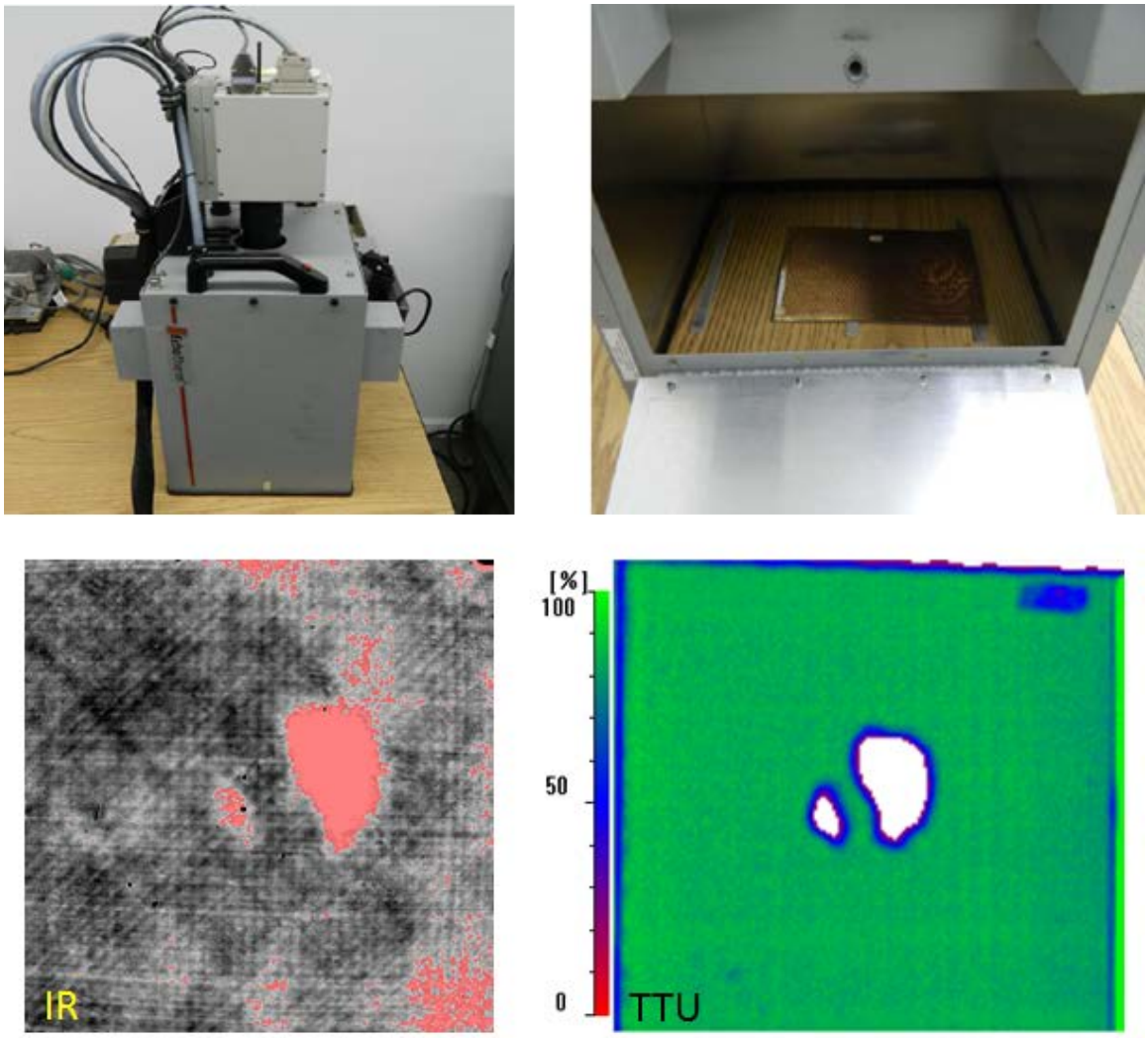

Figure 70. Pulse thermography setup used and example IR inspection results (TC-16-6)

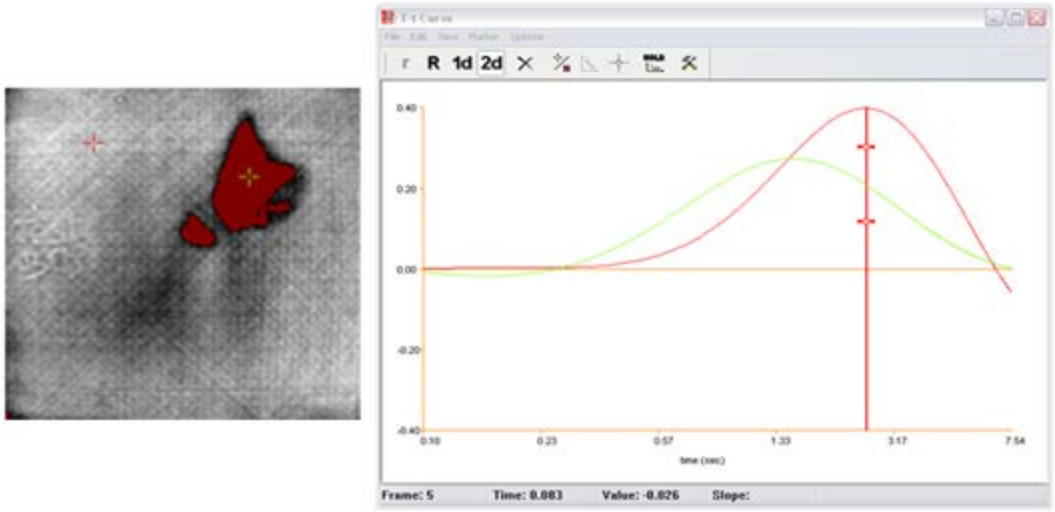

Figure 71. Example time vs. temperature plot and markers used to analyze impact damage

4.1.4 Other Inspections Applied to Select Flat Plate Panels

Early in the hail impact test series, additional NDI techniques were used to assess whether the technologies should be applied to all of the test panels. These included MIA and LFBT.

4.1.4.1 MIA

MIA is the method of bond testing that compares the stiffness of a structure in contact with the probe tip. The probe, in direct contact with the test surface, sends sonic vibrations into the structure and then measures how these vibrations resonate within the structure. A flaw in the structure causes a reduction in its mechanical impedance (stiffness), which changes the displayed signal. The stiffness of the structure is a function of thickness, geometry, elastic variables, and densities of the bonded components. The structure under test is vibrated and disbonds, or other anomalies cause a reduction in mechanical impedance (stiffness), which can result in a phase or amplitude change to the displayed signal depending on the frequency of the probe.

The mechanical impedance of a structure, defined as the ratio of the applied force, F, and the resultant velocity, v, is a measure of the resistance to motion of the part. Like the tap test, the MIA method also exploits the reduced stiffness and, hence, a reduction in the resistance to motion of a structure containing damage. For example, when the same force is applied to the face sheet of a composite honeycomb panel over a region of fractured core, the resultant velocity will be higher and the mechanical impedance will be lower than a region of no damage. Like electrical impedance, the mechanical impedance is also frequency-dependent. In commercial MIA instruments, the probe typically contains a driving piezoelectric element and a receiving piezoelectric element. An oscillatory voltage of a certain frequency is applied to the driving element; the receiving element, sandwiched between the driving element and the structural surface with a spring loaded force, then produces a response voltage with an amplitude and phase dependent on the mechanical impedance of the structure. In practice, the spring loaded probe is moved slowly over the part surface to detect disbonds or delaminations.

MIA was applied to select hail impact panels so the viability of the method to detect hail impact damage in solid laminate structure could be investigated. As expected, MIA was more sensitive to detecting damage in the thinnest 8-ply panels, but significantly less sensitive than the UT techniques used. The technique was limited in its capabilities to detect damage in the thicker 16- and 24-ply panels. It can be seen in figure 72 that the MIA inspections had difficulty imaging the delaminations contained in the four panels shown when compared to TTU. It can also be seen in the MIA results that the paint that had flaked off of the thickest 24-ply panel was imaged and the damage was not.

4.1.4.2 LFBT

LFBT refers to bondtesters that operate below 100 KHz, generally called sonic bondtesters. Figure 73 shows the MAUS V LFBT setup used for testing select panels. Bondtesters generally do not require the use of liquid couplant (dry coupled) and operate in the audio or near-audio frequency range. Different techniques for transmitting and receiving energy have been developed for low-frequency bondtest applications. Each technique introduces a pressure wave into the specimen and then detects the transmitted or reflected wave. The pitch-catch impulse test method uses a dual-element, point-contact, non-couplant, low-frequency sonic probe. One element transmits acoustic waves into the test part and a separate element receives the sound. The sound propagates in a complex wave mode across the test piece between the probe tips. The return signals are processed and the difference between the effects of good and bad areas of the part along the sound path are analyzed and compared. A complex wave front is generated internally in the material as a result of velocity characteristics, acoustical impedance, and thickness. The time and amount of received energy is affected by the changes in material properties, such as thickness, disbands, and discontinuities. The instrument processes the received impulse and displays the received information on a phase and amplitude meter. Using the MAUS system, a C-scan can be composed using both phase and amplitude. Similar to MIA, LFBT was limited on depth of penetration when applied to the 8-, 16-, and 24-ply solid laminate panels. The extent of damage detected when compared to TTU was significantly less, as shown in figure 72.

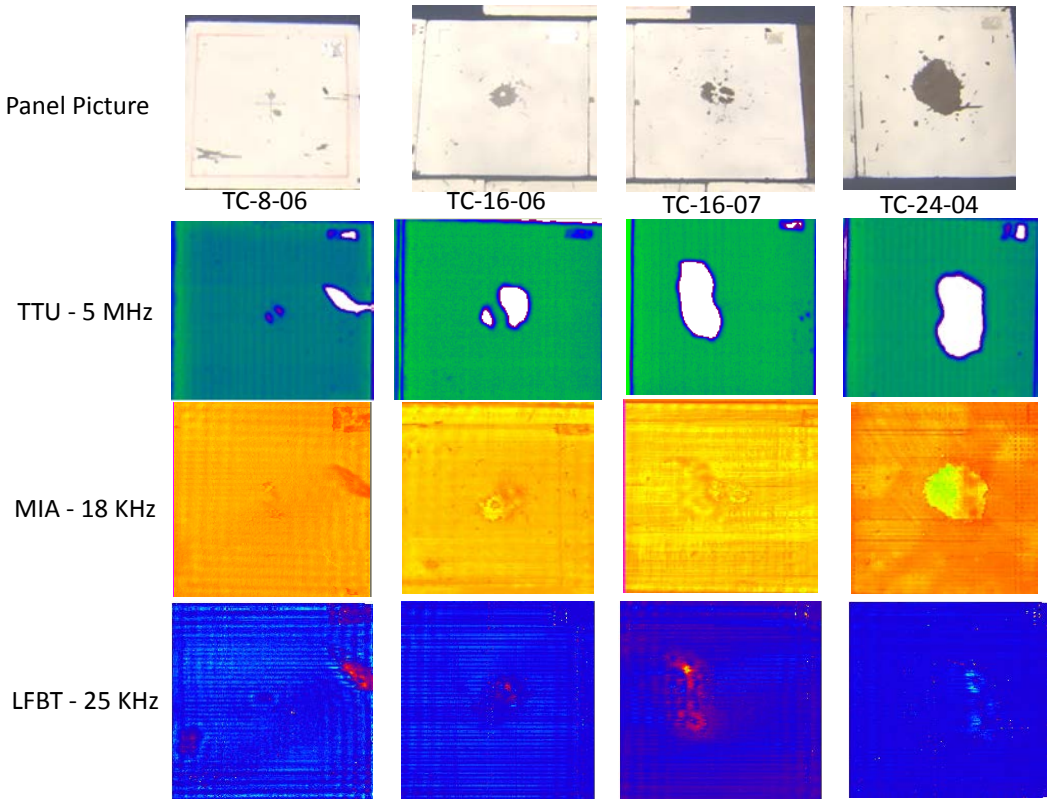

Figure 72. Inspection results for MIA and LFBE compared to TTU results

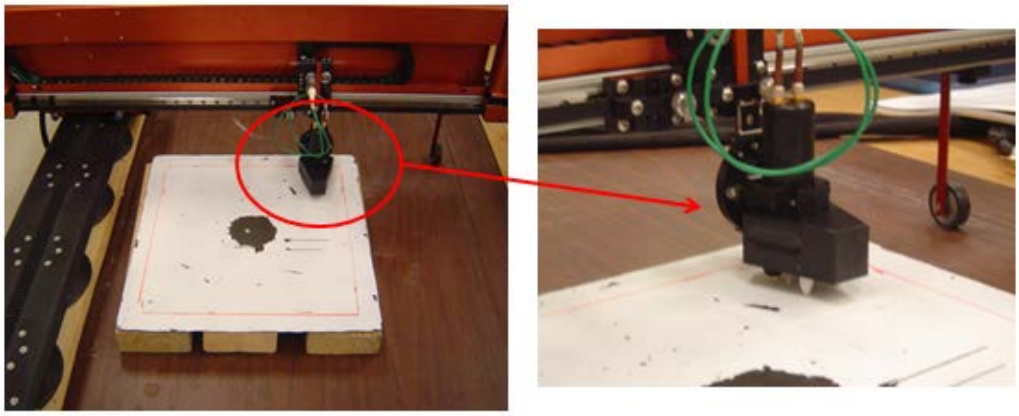

Figure 73. The MAUS 25 KHz low-frequency pitch catch set up tested on select panels

4.1.5 Result of Inspections Applied to Composite Plates

To assess the inspection techniques applied in this study, an impact damage database was assembled for the flat plate panel specimens. Inspection results from each method applied to each panel can be visually compared side-by-side by using the database. The database for the 8-, 16-, and 24-ply panels can be seen in appendix B of this report.

Figure 74 shows an example of an 8-ply panel impacted with a 38.1 mm diameter hail ball. This panel contains a delamination on each side of the impact site. The impact damage generated in this panel is an example of a small-to-medium delamination when compared to the other test panels. It can be observed that all 10 NDI techniques detected the damage on this panel. Two additional NDI techniques used to inspect this panel were not applied to all of the panels. They were the Toshiba Matrixeye™ and LaserUT®. The A-scan shown in the figure clearly shows a shift in the reflected signal, indicating a delamination, which was also detected using the ramp damage check (RDC) device.

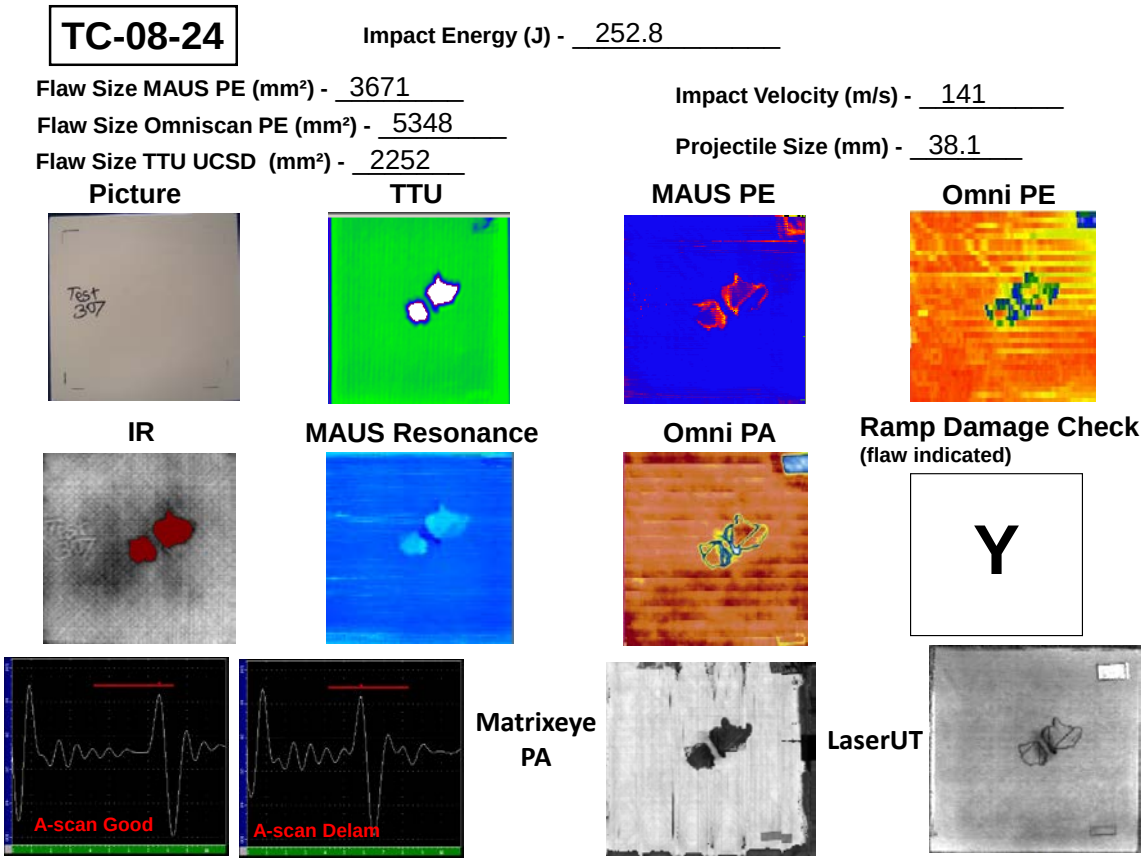

Figure 74. Inspection comparison on 8-ply flat plate panel

Figure 75 shows an example of small impact damage on a 16-ply panel impacted with a 50.8 mm diameter hail ball. The damage induced on this panel was detectable using some NDI methods. The delamination area determined using TTU for this panel was 62 mm^2. The affected zone at which a 6 dB drop in amplitude was noticed using the MAUS and OmniScan was approximately 1500 mm^2. The damage was not detected in the flash thermography scan, in resonance inspection, or by the RDC. A decrease in UT amplitude could be observed using single-element pulse echo, as shown in the lower left area of figure 75. This impact panel is a good specimen to demonstrate how the impact database can be used to compare sensitivity differences in the NDI techniques used.

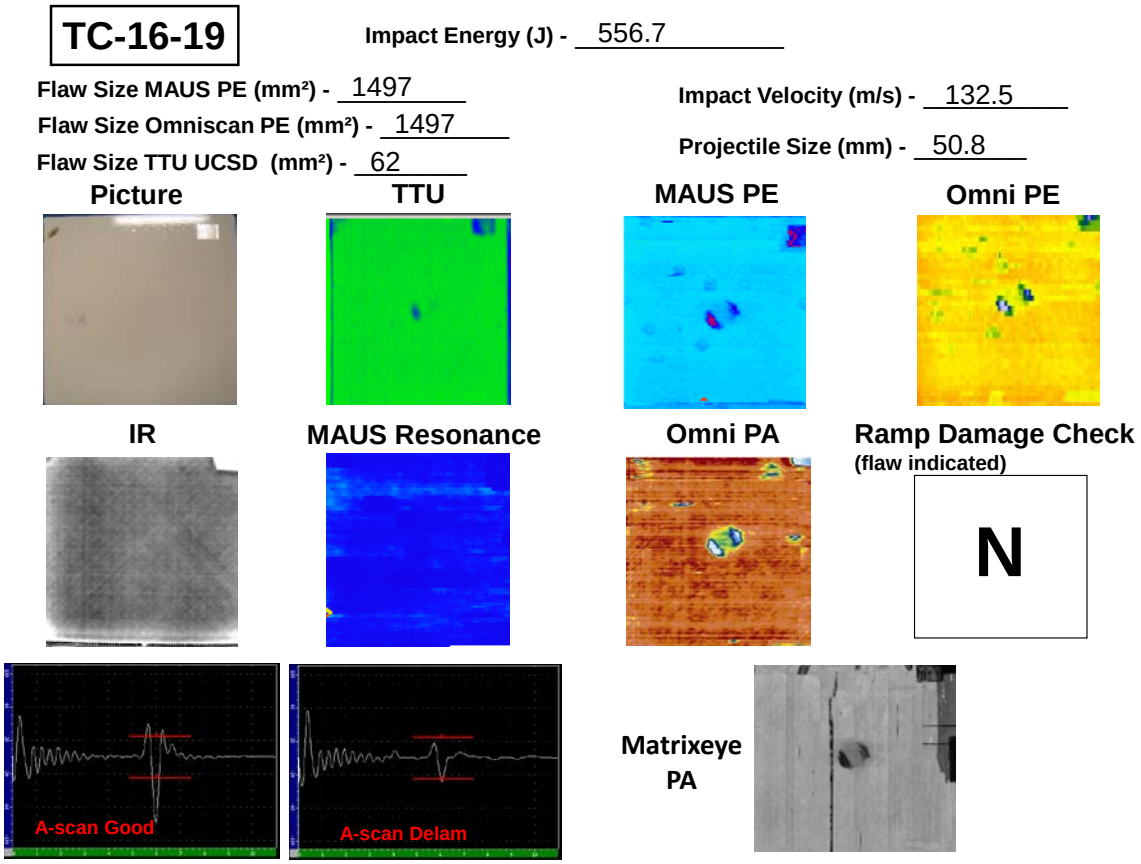

Figure 75. Inspection comparison on 16-ply flat plate panel

Figure 76 shows an example of a large delamination generated on a 24-ply panel with a 50.8 mm hail ball. All NDI methods applied to this panel were capable of detecting the impact damage on this specimen. Because the 24-ply specimens were the thickest in this study, NDI techniques with limited depth of penetration began to lose some sensitivity to resolve the full damage. Those included thermography and some resonance scans on the smaller area impact damage specimens.

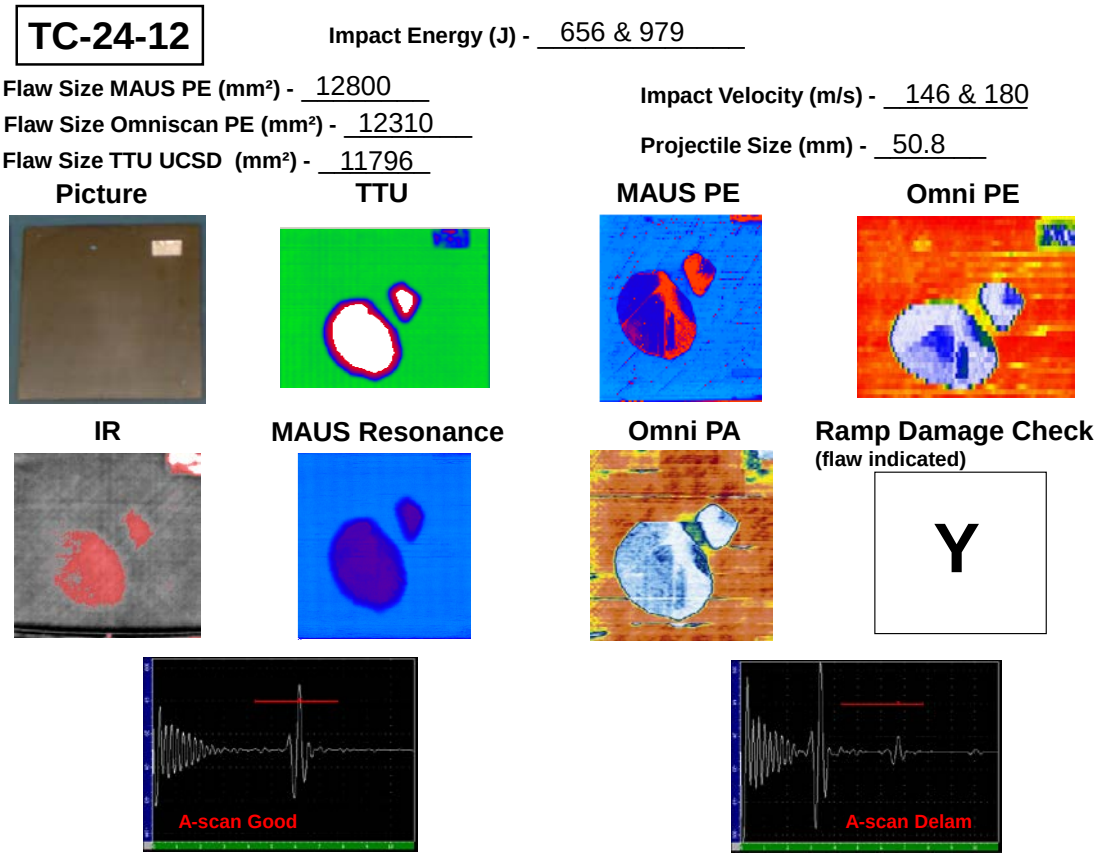

Figure 76. Inspection comparison on 24-ply flat plate panel

Three UT methods were selected to determine the area of damage generated by each SHI. The methods used were the MAUS V pulse echo with a 5 MHz transducer, the OmniScan 10 MHz phased array, and 5 MHz thru-transmission. The approach used to calculate area for each technique is described in section 4.1.1.

One panel thickness was selected to present damage area tables and plots in this section, but the damage area results for all panels are presented in appendix A. Table 6 shows the highest energy impact conducted on each 16-ply panel, the measured velocity, the damage area determined using the three UT methods described, and the simulated hail ball diameter used.

Table 6. Damage area for 16-ply laminate plates

16-Ply Flat Plates - Impact Test Summary - Simulated Hail Highest Energy Level Shown						
Panel No.	Highest Impact Energy (J)	Highest Impact Velocity (m/s)	MAUS PE Damage Area (cm^2)	OmniScan PE Damage Area (cm^2)	TTU Damage Area (cm^2)	SHI Diameter (mm)
TC-16-04	302	157	15	10	0	38.1
TC-16-06	332	162	43	39	28	38.1
TC-16-14	385	173	0	0	0	38.1
TC-16-15	373	170	0	0	0	38.1
TC-16-24	487	193	85	66	65	38.1
TC-16-25	525	212	294	284	264	38.1
TC-16-26	487	197	168	188	143	38.1
TC-16-27	487	191	115	104	93	38.1
TC-16-29	433	191	41	42	37	38.1
TC-16-30	406	185	133	143	123	38.1
TC-16-31	439	187	93	99	86	38.1
TC-16-32	357	169	51	58	48	38.1
TC-16-07	561	133	75	93	71	50.8
TC-16-12	458	123	118	127	108	50.8
TC-16-16	620	N/A	0	9	0	50.8
TC-16-161R	788	159	159	190	135	50.8
TC-16-17	513	128	6	14	0	50.8
TC-16-18	705	150	150	198	131	50.8
TC-16-19	557	133	15	15	1	50.8
TC-16-28	488	127	45	53	41	50.8
TC-16-03	749	117	24	33	15	61.0
TC-16-08	423	89	17	11	0	61.0
TC-16-09	522	100	39	48	37	61.0
TC-16-10	512	98	25	10	0	61.0
TC-16-11	505	97	57	56	44	61.0
TC-16-20	697	113	12	12	0	61.0
TC-16-21	639	109	13	18	0	61.0
TC-16-22	602	N/A	9	9	0	61.0
TC-16-22R	782	121	311	254	175	61.0
TC-16-23	507	97	0	4	0	61.0
TC-16-23R	719	116	0	33	0	61.0

Impact energy versus resulting damage area for the 16-ply thick specimens is shown in figures 77–79. The damage area determined using the MAUS and OmniScan are typically larger than the damage area determined by the through-transmission technique. This is because the damage area was determined using different techniques. The MAUS and OmniScan were used to examine the extent of delamination and the area around the delamination, at which point the amplitude of the returned signal dropped approximately 6 dB. This was visually assessed by C-scan post- analysis. The resulting damage area could be thought of as the zone affected by the

hail impact. The decreased amplitude surrounding the delamination is most likely a result of microcracking in the matrix. The through-transmission technique used was set up to determine only the area of delamination. Ultrasound either made it through the laminate or was reflected by the delamination. That is why the TTU area is typically smaller than the other two methods.

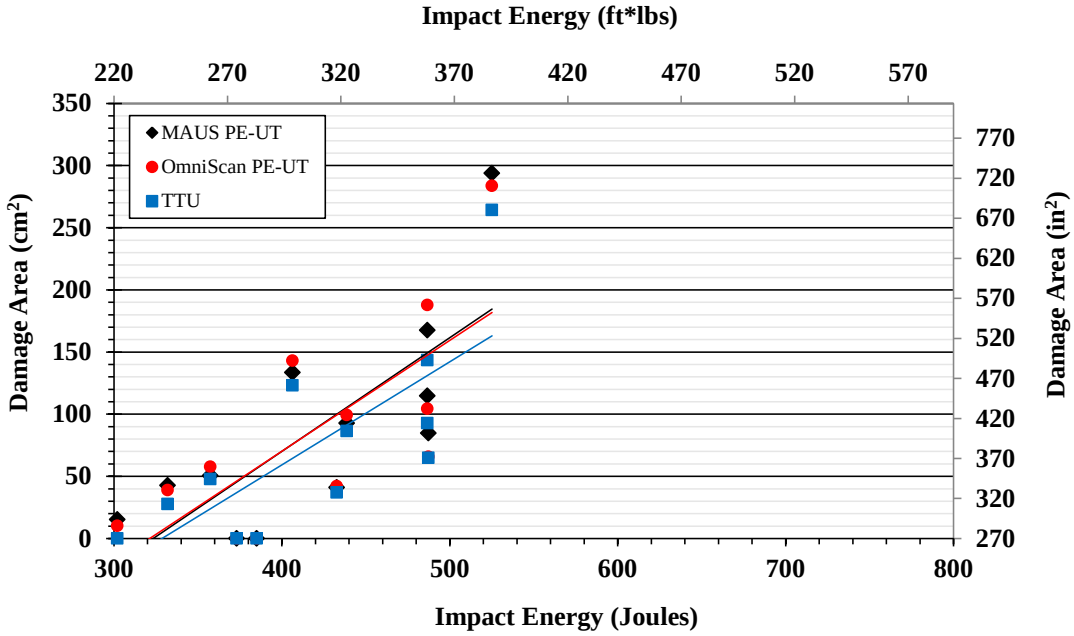

Figure 77. Impact damage area for 16-ply laminates – 38.1 mm. diameter simulated hail

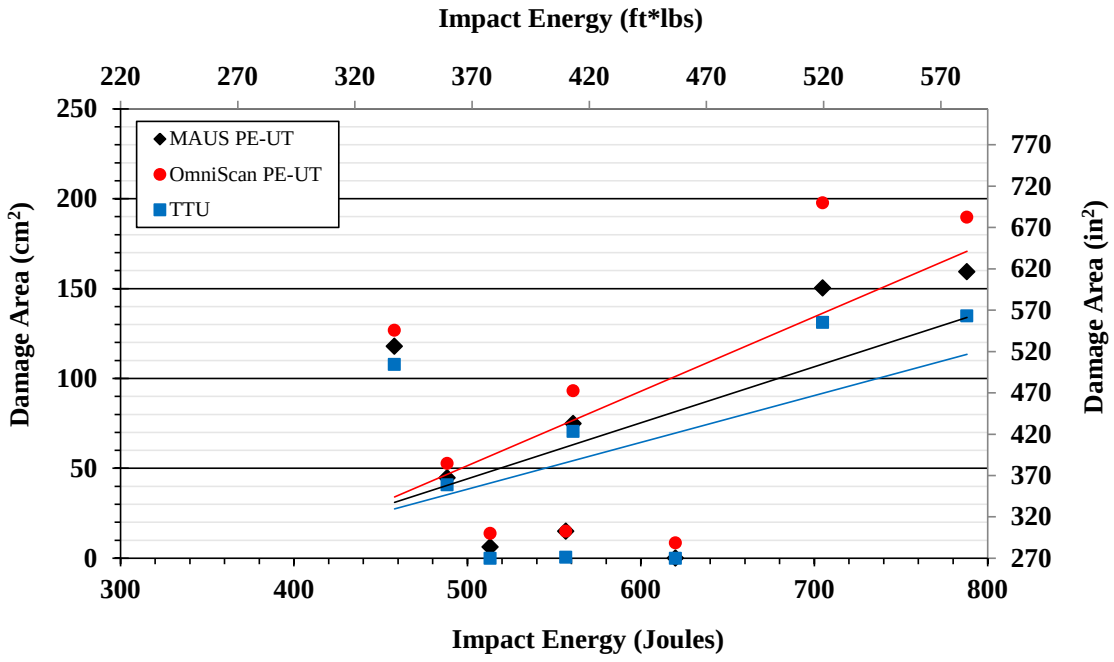

Figure 78. Impact damage area for 16-ply laminates – 50.8 mm. diameter simulated hail

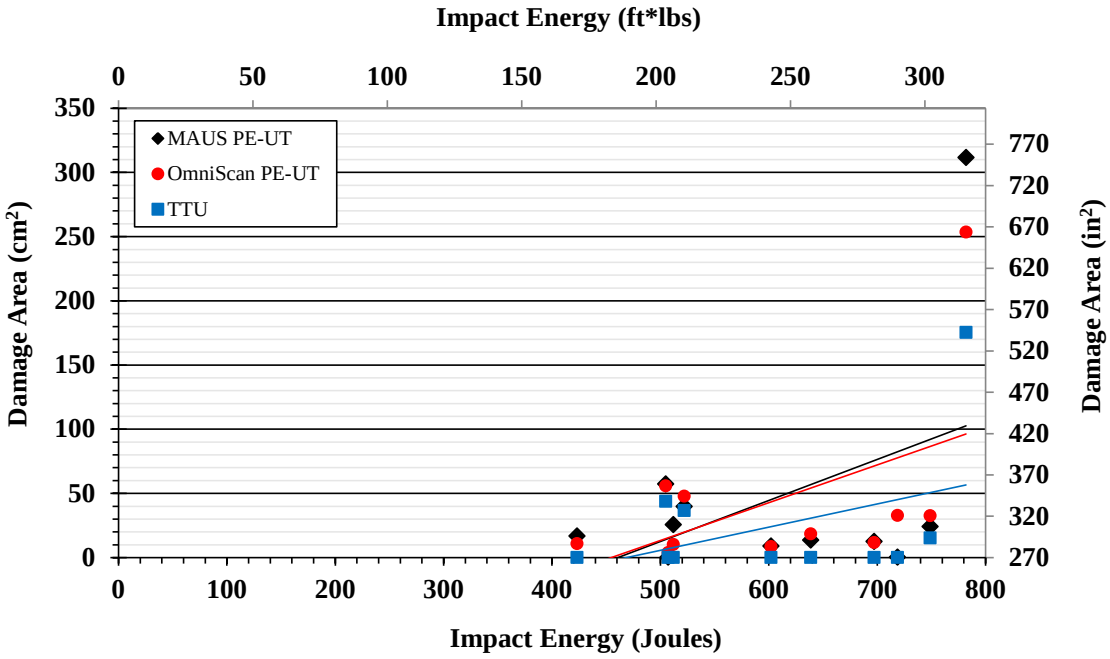

Figure 79. Impact damage area for 16-ply laminates – 61.0 mm. diameter simulated hail

By conducting inspections on the 81 flat plate hail impact specimens with multiple NDI methods and comparing the inspection results obtained in this study, some qualitative assessments were made regarding each technique's ability to detect and characterize hail impact damage in a solid laminate composite aircraft structure.

- An LFBT was applied to select panels; this was not an adequate method to detect hail impact damage in the specimens tested
- MIA could detect some level of delamination in the select panels to which the technique was applied. Detection was possible when the delamination manifested itself near the surface of the panel and affected the relative through thickness stiffness of the specimen. The technique was not sensitive enough to detect small damage or damage in the thicker laminates (unless near the surface)
- TTU was effective for examining delamination areas generated by hail impact. Both 1 MHz and 5 MHz TTU inspections were performed on all panels and both frequencies effectively resolved the delamination. The techniques were not well-suited to examine areas around the delamination where decreased amplitude was observed because of microcracking in the matrix. TTU was also not an effective tool to investigate the depth of delamination
- The UT inspection using the MAUS system was an efficient and sensitive tool to characterize damage induced by hail impact. Low-level impact damage generated by hail that did not fully induce delamination could be observed using the MAUS system with a 5 MHz, 0.25″ diameter transducer. This typically was visually detected in the C-scan results and was indicated by a slight decrease in UT amplitude. Post-processing using the system was not possible because the system does not perform full waveform capture. This limited how the data could be presented to the results first obtained when the system was first set up

- The OmniScan with the manually deployed scanner and single-element transducer rendered lower resolution scans (dependent on indexing distance) and was time-consuming when compared to the other inspection techniques. Typically, the setup was capable of detecting levels of damage similar to the other UT techniques, but with decreased resolution and image quality making it more difficult to detect subtle damage
- In most cases, if a delamination occurred because of hail impact (confirmed when compared with TTU), it was detected using the flash thermography system. Using time versus temperature plots and masking techniques, results could be fine-tuned to fully investigate the laminate damage. Subtler damage in the thickest 24-ply laminate was often not detected using the flash thermography technique
- The MAUS resonance was applied to all of the hail impact specimens. The technique was not as sensitive detecting hail impact damage as the PE-UT methods applied to the specimens
- The RDC device performed well on the flat plate solid laminate specimens. Because there were no substructure calibration issues and the panels were of uniform thickness, the unit typically indicated damage when a delamination was present. This was confirmed with TTU and other inspections. The unit would not indicate damage if a delamination was not identified in the TTU inspection, even if there was a decrease in amplitude shown in the other UT-based scans (e.g., see TC-8-11 in appendix B)
- A-scan analysis was performed on each panel to investigate shifts in the returned signal and drops in signal amplitude at the impact location. A-scan analysis was useful to estimate the depth of delamination and provide a more detailed check as to what was revealed in the UT C-scans. This method of inspection was also used after each impact was conducted during testing to determine whether the level of intended damage was achieved

4.2 DAMAGE CHARACTERIZATION ON FULL-SCALE PANELS

For this experimental investigation, 45 ice impacts were performed at 22 different locations (some multiple impacts at the same location) on two full-scale fuselage panels. Additionally, 69 2″ diameter spherical tip impacts were performed at 43 different locations on one of the panels. The quantity of each type of impact on the different structural elements of the panel is shown in table 7.

Table 7. Number and type of impacts conducted on panels (some experienced multiple impacts at same location)

Number of Impact Test Performed		
Structure Type	Simulated Hail	Hard Spherical
1 - Center Bay Over Skin	19	16
2a - Edge of Stringer Flange (Not Stringer Side)	6	13
2b - Center of Stringer Flange	9	14
2c - Edge of Stringer Flange (Stringer Side)	0	12
3 - Mid-Stringer	6	11
4 - On Shear Tie	5	3

Panels A and B were separated into quadrants for simulated hail and hard spherical tip impact testing. The SHI damage was induced in two quadrants of panels A and B. Drop spear spherical tip impacts were performed in two quadrants on panel A.

Strain data were collected on the embedded FO during SHI testing, but because of heat induced by the halogen lamps used to illuminate the panel during testing for the high-speed cameras, a majority of the data collected were not usable. However, strain data were successfully collected during hard, drop spear impact testing using two different bonded FO layouts.

The naming convention used to describe each impact is made up of the bay number, skin number, stringer number, and impact type. An example using this naming convention is B2-SK2-ST1L-H2c or Bay#-Skin#-Stringer# (left or right)-Impact Type (H for hard and I for ice). With the name and panel schematic shown in figure 80, each unique impact can be identified and located on the panel.

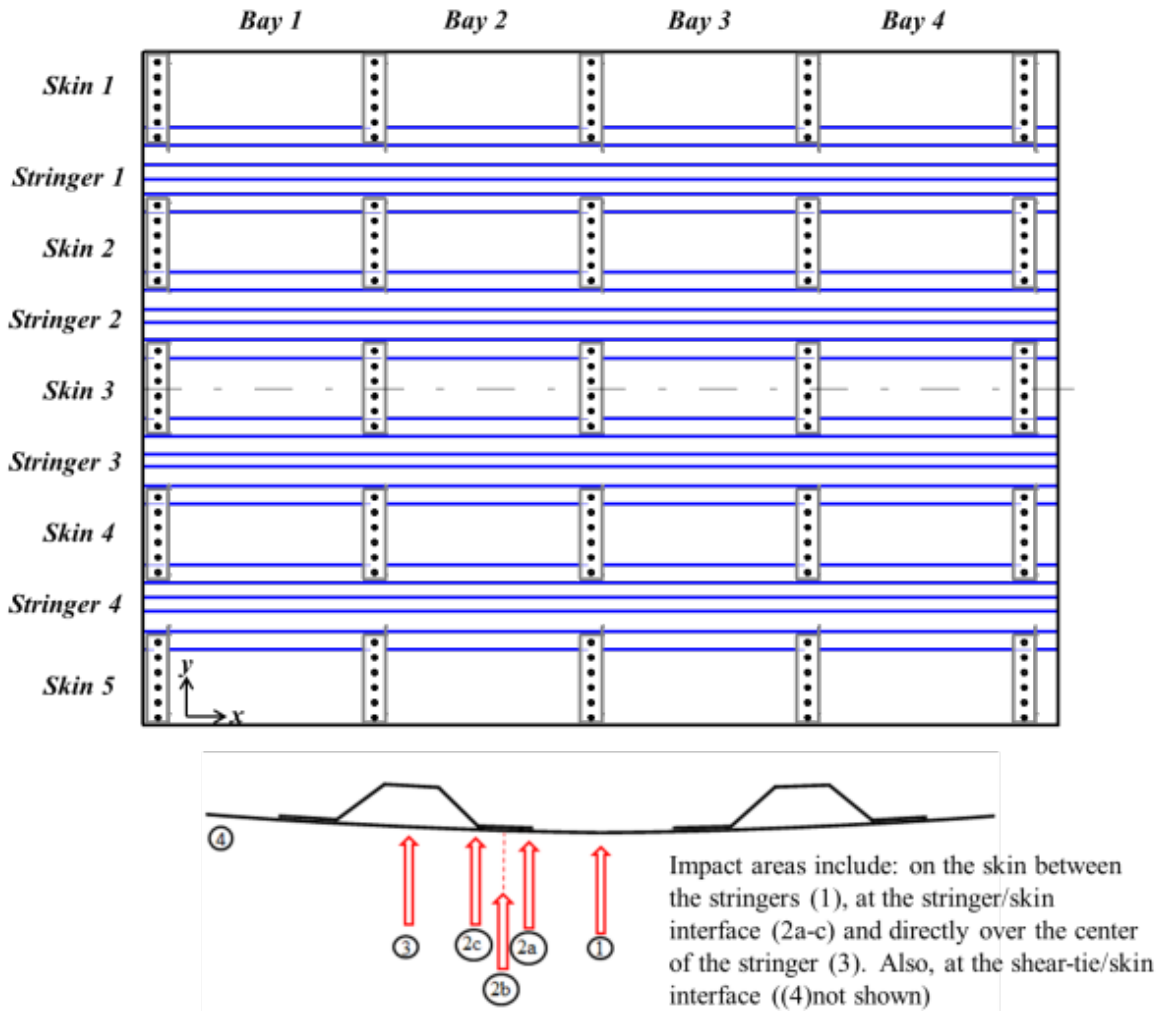

Figure 80. Schematic used to label and locate impact damage

Damage characterization was accomplished through detailed visual inspection on both sides of the panels and through NDI methods, including UT amplitude analysis, TOF, and resonance. A database was assembled containing pertinent impact information at each impact location, which is presented in appendices B and C. The database contains information regarding all impact damage, including location of impact, maximum impact energy, maximum impact velocity, visual indications of impact damage, damage area, interpretation of type of damage, and C-scan images of the damage.

Damage was assessed by interpreting information gathered through the NDI techniques on a structural level. Example A-scans showing how the return signals change depending on the type and depth of damage are shown in figure 81. A clear back wall signal over the skin laminate is shown in A, an A-scan over a skin interply delamination is shown in B, a co-cured stringer flange disbond is shown in C, an interply delamination in the flange of the stringer is shown in D, and near-surface skin damage is shown in E. A complete loss of back wall signal with no appearance of an intermediate signal was interpreted as near-surface fiber fracture or matrix crushing and was typically observed in hard impacts.

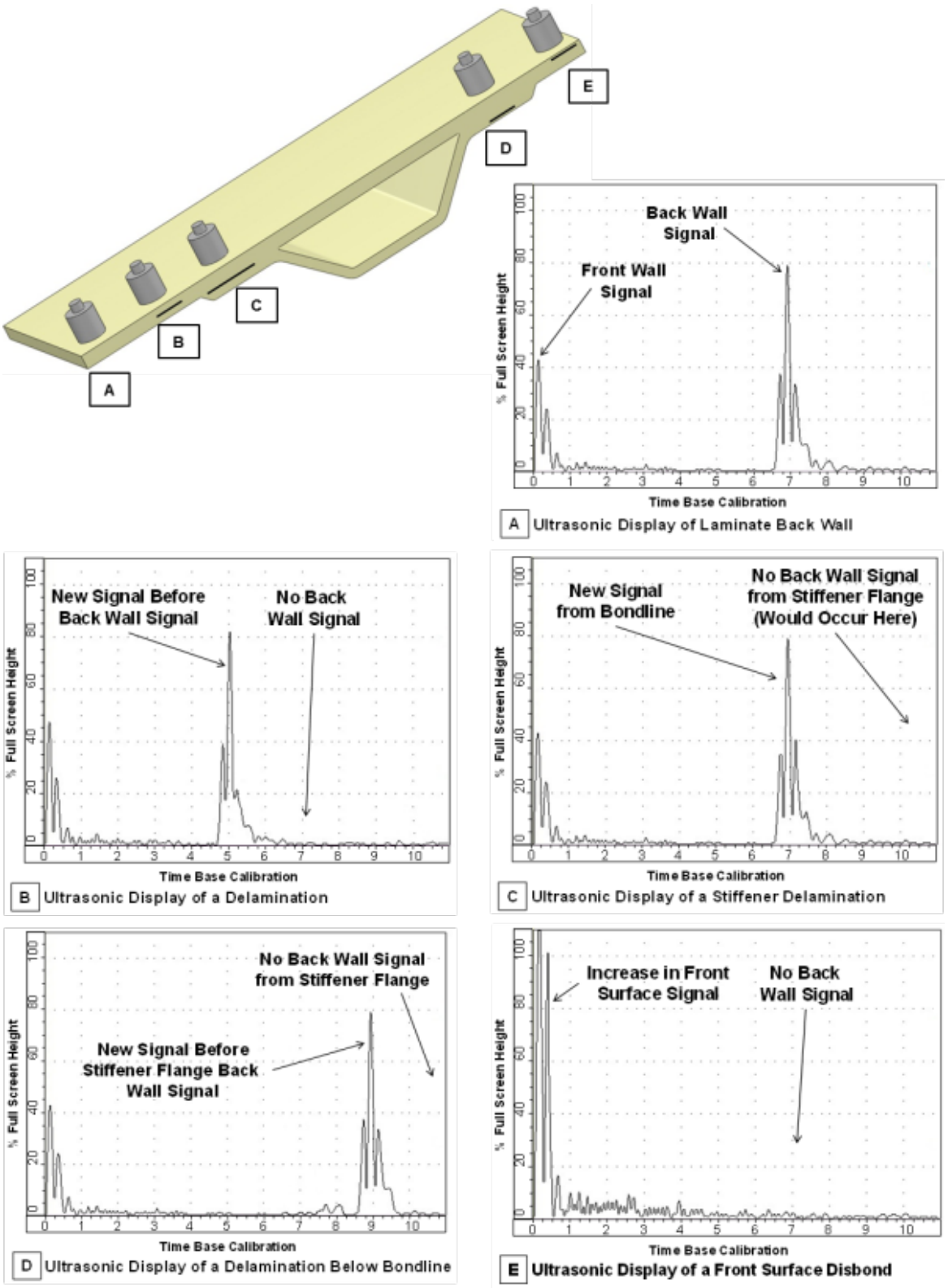

Figure 81. Example A-scan signals over different structural elements and damage

4.2.1 UT Damage Section

After each impact test was performed, a hand-deployed 5 MHz UT transducer was used to determine whether damage was induced during the impact. If the desired level of damage was not obtained, the panel was impacted again. Notes were taken during these initial hand-deployed inspections and were documented and mapped out on the panels. Typical signal changes of interest were loss of back wall signal and a shift in the back wall signal. A less common signal change was a decrease in amplitude (not total loss of signal).

When the full set of impact tests was completed, each panel was inspected using the Boeing MAUS V system in both UT pitch-catch (5 MHz) and resonance (330 KHz) modes. Figure 82 shows the scanning system, mounted via vacuum suction, inspecting panel A. The inspections of the panels were split into ten sections—five across the top of each panel and five across the bottom. The ten scans were then reassembled to make up the inspection of the entire panel.

Figure 82. Boeing MAUS V scanning system conducting a UT inspection

The C-scan inspections revealed significantly more information than the handheld pulse-echo inspections performed during impact testing. Flaws that were difficult to size using hand-deployed UT were easily sized and mapped using a combination of amplitude and TOF C-scan images. The difference in damaged mapping is illustrated on the top left side of panel B in figure 83. The black mapped regions of damage were sized using handheld UT and the red mapped regions using a combination of UT amplitude, TOF, and resonance.

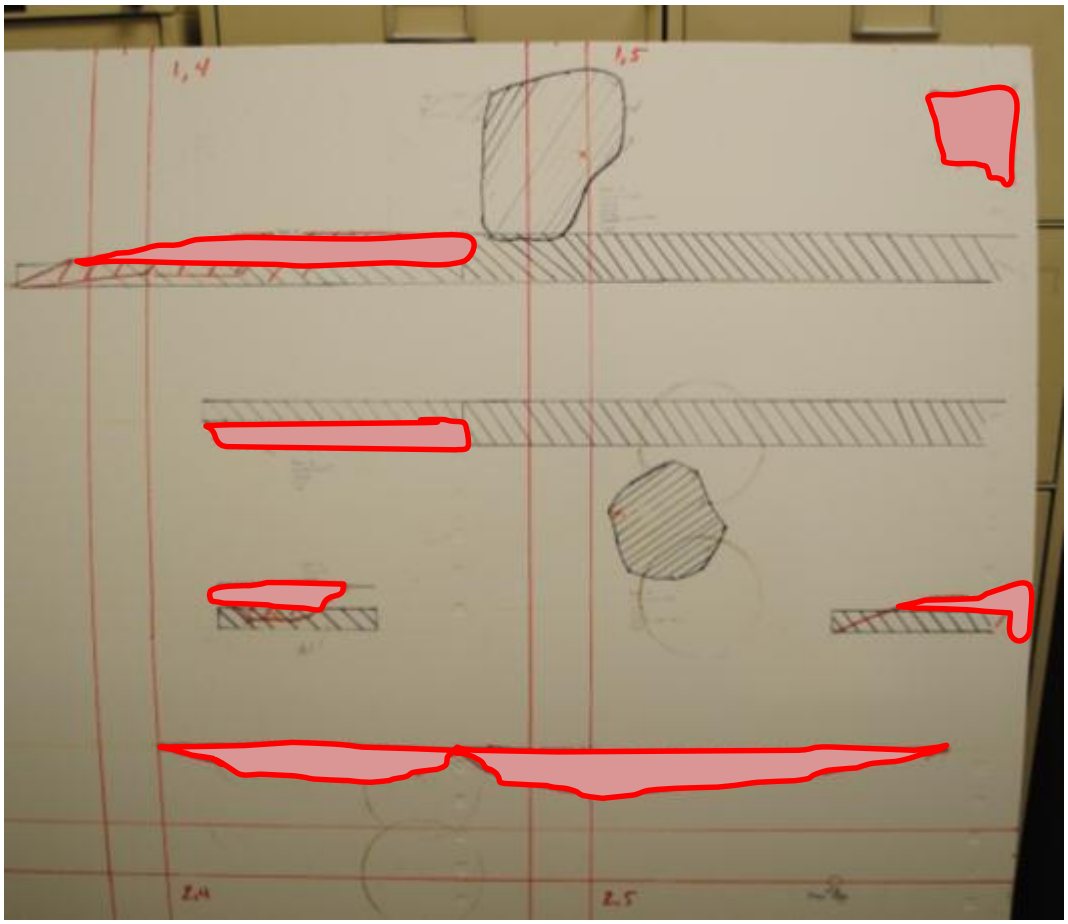

Figure 83. Top right side of panel B—black mapped damage was detected after impact with hand-held UT, and red mapped damage was additional damage detected and sized using the MAUS V scanning system

Interply delaminations in the skin of the panels and stringer flange delaminations were the two most common damage modes observed in the post-inspections of SHI. The example C-scan shown in figure 84 shows the difference between an interply delamination in the skin and a stringer delamination, which were both induced by an SHI. It was also noted that hail impact can produce damage in regions that were farther from the impact location than anticipated. Some of this distant damage was not detected during initial A-scan inspections. Also shown in the figure is the clear difference between a bonded and disbonded stringer flange. The scan on the left of the figure has one fully bonded stringer flange and one partially disbonded flange. The image on the right has two fully bonded flanges. These two images can be compared to the pristine area shown at the top of the figure.

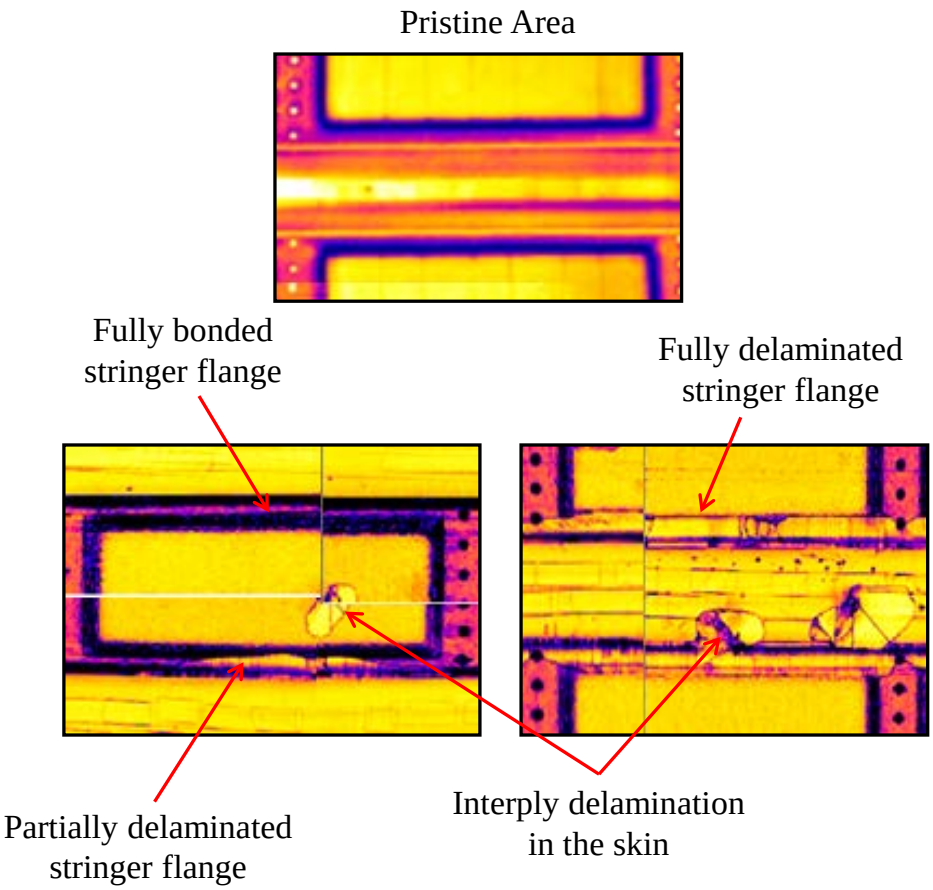

Figure 84. Impact damage induced on panel A showing the difference between interply delamination and stringer flange delamination

Although it is fairly simple to detect delaminated stringer flanges using the amplitude C-scans, additional, less obvious delaminations could be detected when analyzed side-by-side with TOF C-scans. An example of a TOF C-scan demonstrating the clear difference between a bonded and delaminated stringer flange is shown in figure 85. The purple areas in the figure are fully bonded flanges. The yellow/orange areas of the flange are at the same depth as the back wall of the skin of the panel, indicating a delamination at the skin-flange interface (right image).

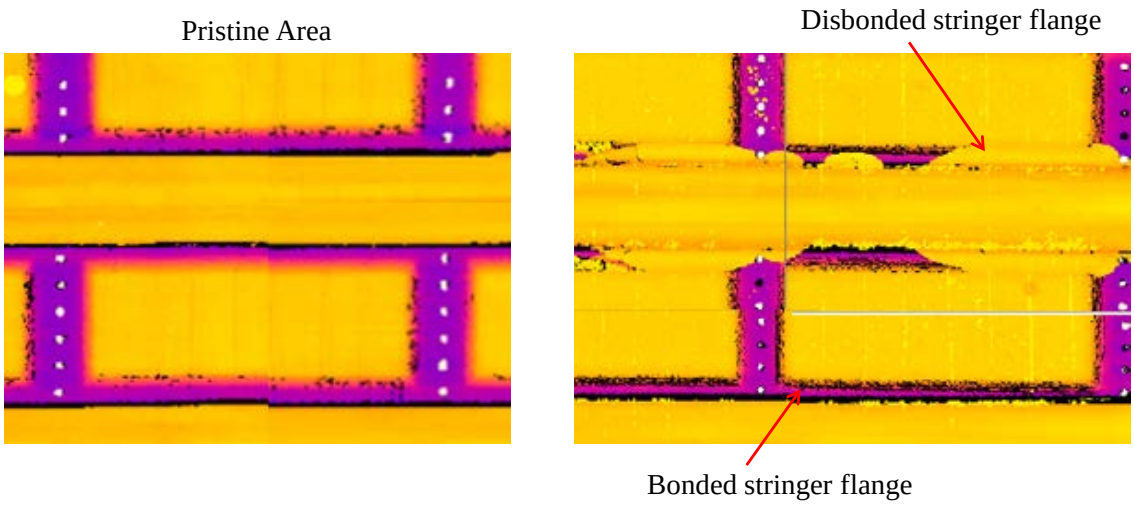

Figure 85. UT TOF C-scan showing delaminated stringer flanges

Full panel PE-UT inspections of panels A and B are shown in figures 86 and 87. The upper left and lower right sides of the panel inspections in figure 86 show the two areas of panel A that were impacted with the drop weight spherical tip impactor. The upper right and lower left quadrants are the two areas that were impacted with simulated hail. Similarly, figure 87 shows the PE-UT full-panel inspection results for panel B. The top left and bottom right are pristine, untested areas of the panel and the upper right and lower left were quadrants tested with simulated hail. Much greater inspection detail, including exact impact location, energy levels, and damage area, can be found in appendix B, for ice impact tests, and appendix C for hard impact tests.

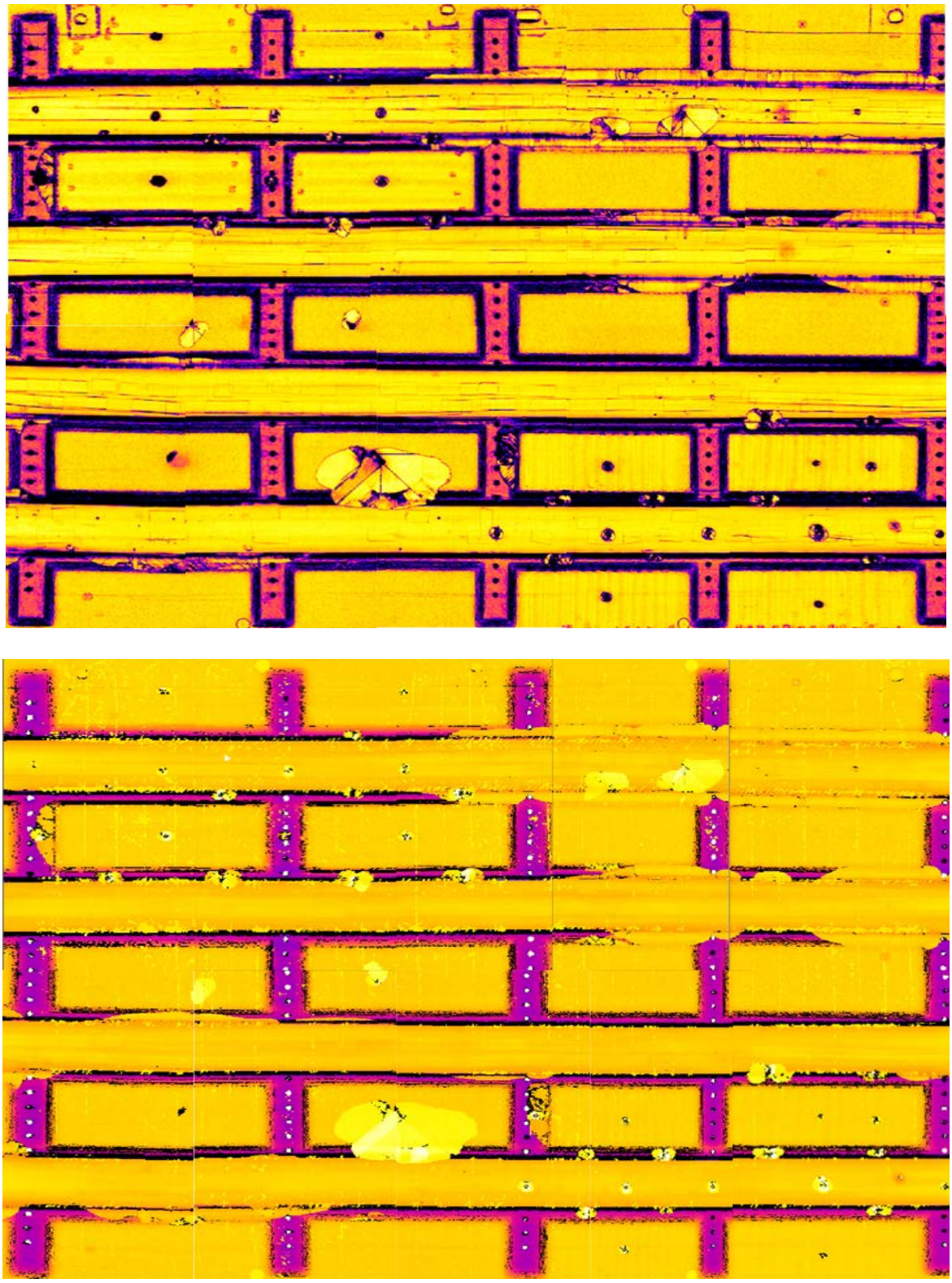

Figure 86. Panel A – UT amplitude (top) and TOF (bottom) C-scans

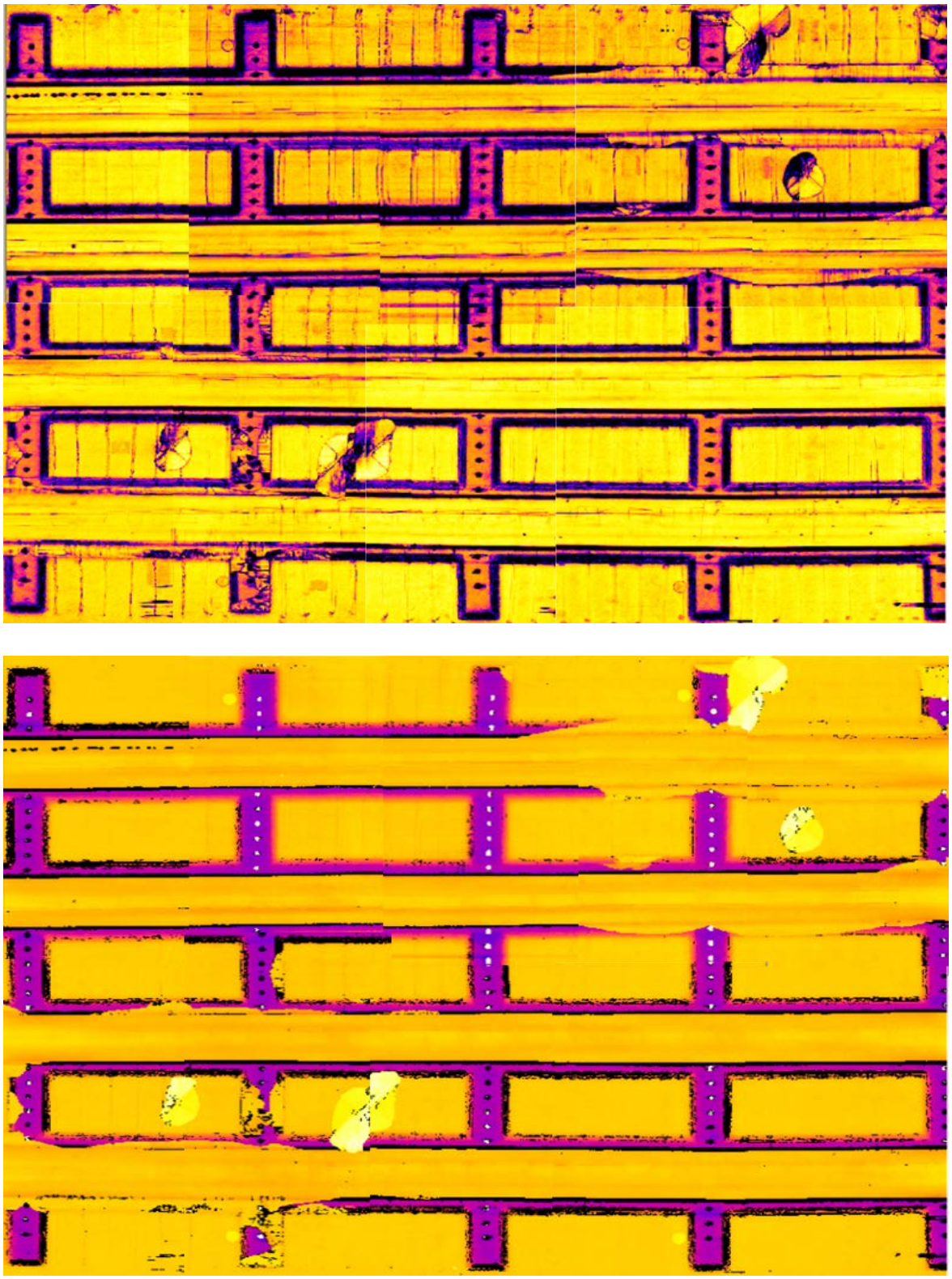

Figure 87. Panel B – UT amplitude (top) and TOF (bottom) C-scans

4.2.1.1 Damage Area Determination

The area of damage induced by SHI was determined using TOF C-scan images generated during PE-UT inspections. The TOF C-scans were imported into SolidWorks® and scaled to the physical dimensions of the panel. The damage was traced and the area calculated using a SolidWorks surface-area calculation feature. The traced areas used to calculate the damage area on panel B are shown in figure 88.

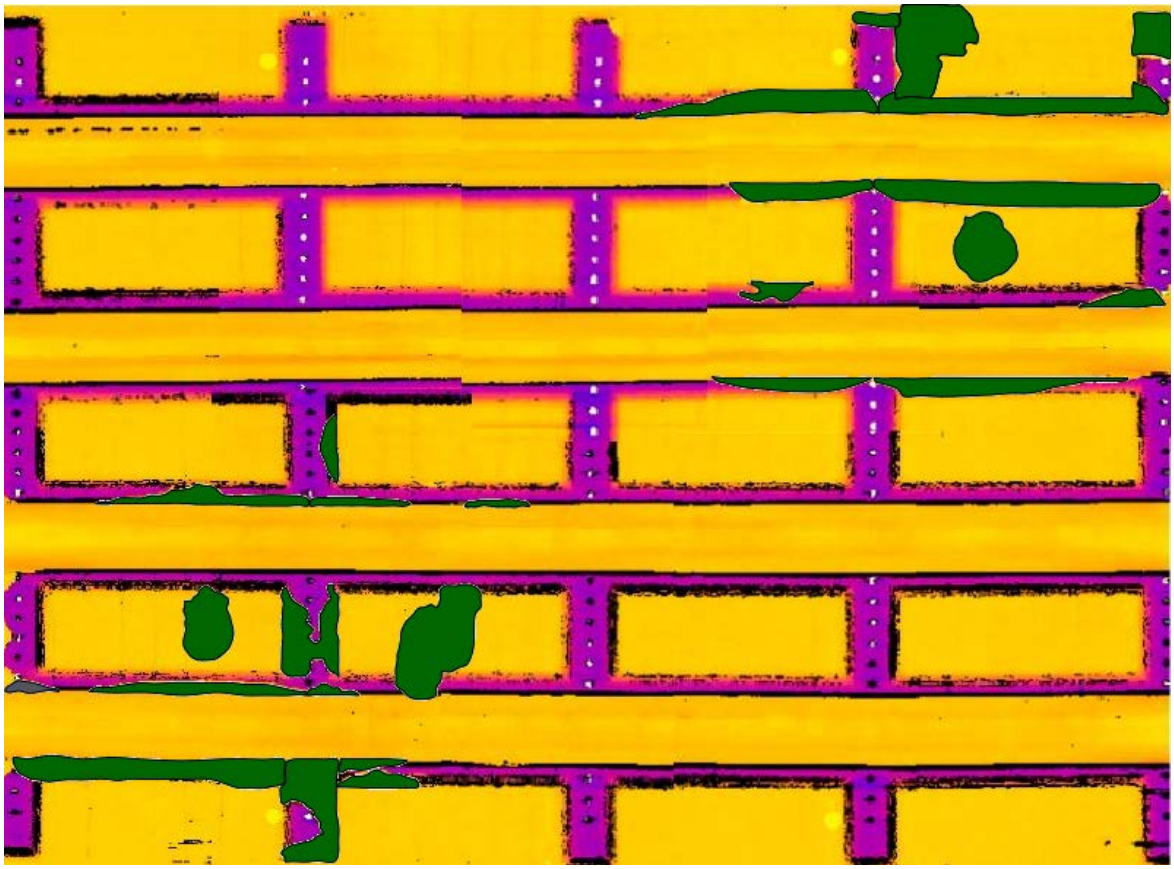

Figure 88. Green tracings used to determine damage area on Panel B

4.2.2 UT Resonance Damage Detection

The UT resonance C-scans were composed using the MAUS V scanning system with a 330 KHz resonance probe. In general, the resonance inspection technique detected the same damage as the PE-UT method. Similar to the TOF scans, resonance indicated areas where the substructure was disbonded from the skin more clearly than PE-UT amplitude. This is shown in figure 89, where the small stringer flange disbond in the circled area is detected in the TOF and resonance inspections but not in the amplitude inspection.

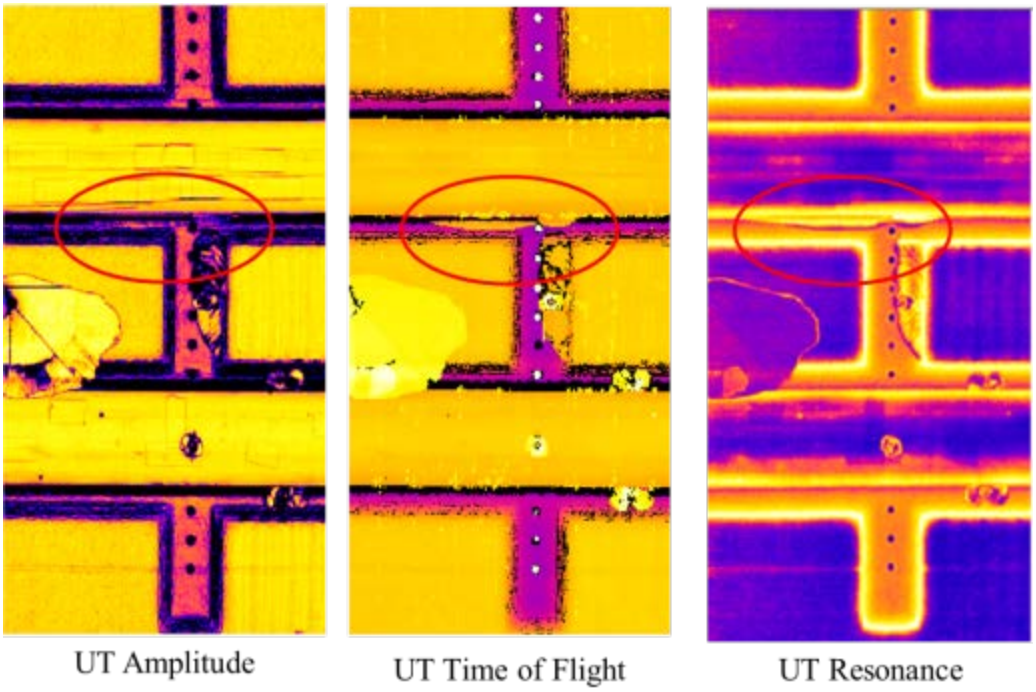

Figure 89. Comparison of UT amplitude, TOF, and resonance inspection results

Fully assembled resonance scans of panels A and B are shown in figures 90 and 91, respectively. There is a slight difference in the color pallet between panels A and B because of the way the resonance inspection technique was zeroed, or nulled. The probe was nulled on a pristine location on each panel, then the inspection was performed. There was also a slight difference in the initial null settings between the two panels, thus creating the difference in pallet.

The clear difference between bonded and disbonded stringer flanges can be observed by comparing the upper right and upper left sides of panel B. The upper left side of the panel was not impact tested and all of the substructure elements are still bonded. By comparison, disbonded stringer flanges can easily be detected on the upper right and lower left sides of the resonance scans in figure 91, as well as interply delaminations in the skin.

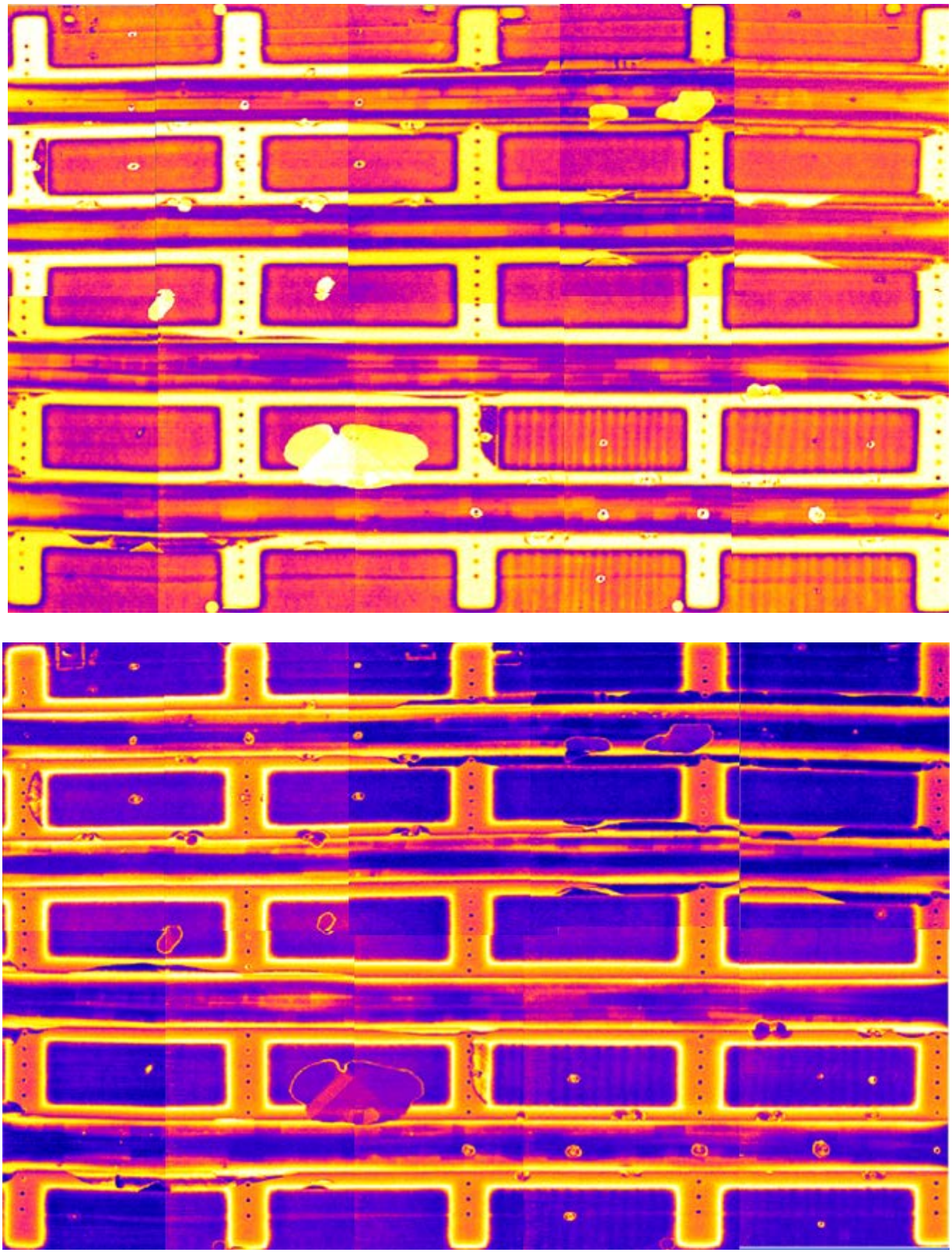

Figure 90. Panel A – resonance amplitude X plot (top) and Phase Y plot (bottom) C-scans

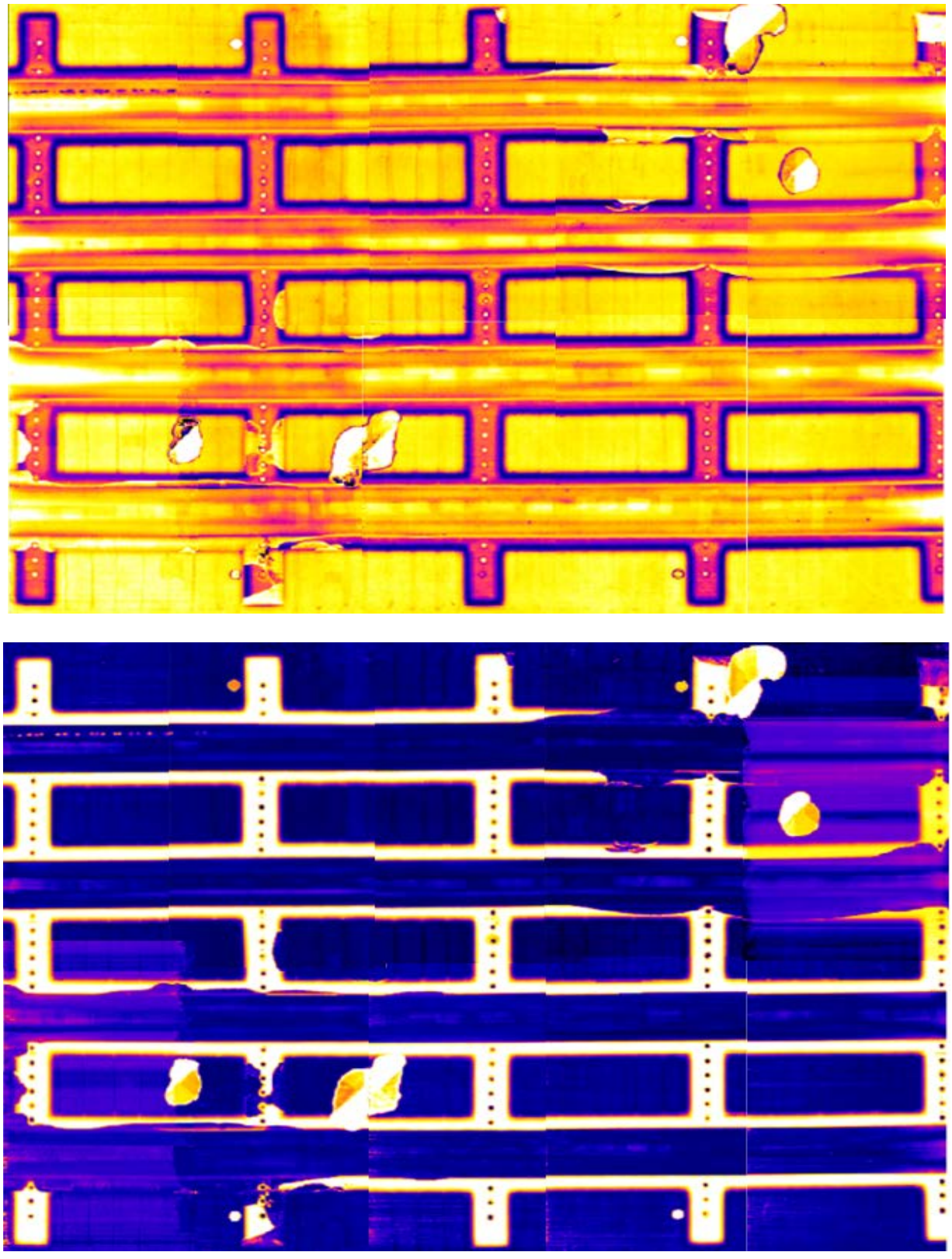

Figure 91. Panel B – Resonance amplitude X plot (top) and Phase Y plot (bottom) C-scans

The information gathered from the scans was assembled and analyzed at each impact location. The ice impact damage created from a 721 Joule, mid-bay skin impact is shown in figure 92. The information shown in the figure is an example of the data assembled for each test location and is provided for each impact location in the appendices. The damage shown in figure 92 is an example of a large interply skin delamination. The top of the figure shows what type of structure was impacted. Two up-close C-scans of the damage are shown in the middle of the figure (UT amplitude and resonance). The green dashed line in the close-up amplitude scan indicates where on the backside of the panel there was a visual indication of damage, if any. In this case, it was a 2″ crack in the stringer flange. The bottom two C-scans are the quadrant where the damage is located. The green dashed box in the quadrant scan shows where the close-up was taken. The damage induced during this impact also provides a good example of a small stringer flange disbond that was difficult to detect in the amplitude C-scan but is easily visible in the resonance scan.

5A - B2-SK4-ST0-I1

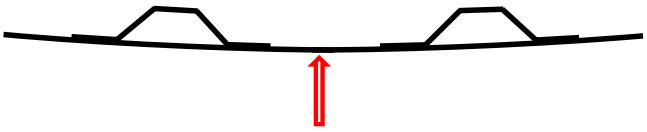

Skin Impact
Max Impact Energy: 531.9 ft lbs, 721.1 Joules
Max Impact Velocity: 382.9 ft/s, 116.7 m/s
Visual Indication: No front side visible indication, small 2” stringer flange crack detectable on backside
Damage Area: Interply Delamination 54.97 in^2, Stringer Disbond 1.70 in^2
Type of Damage: Mostly interply delamination, small stringer disbond to the upper right of the impact area not detected in amplitude scan

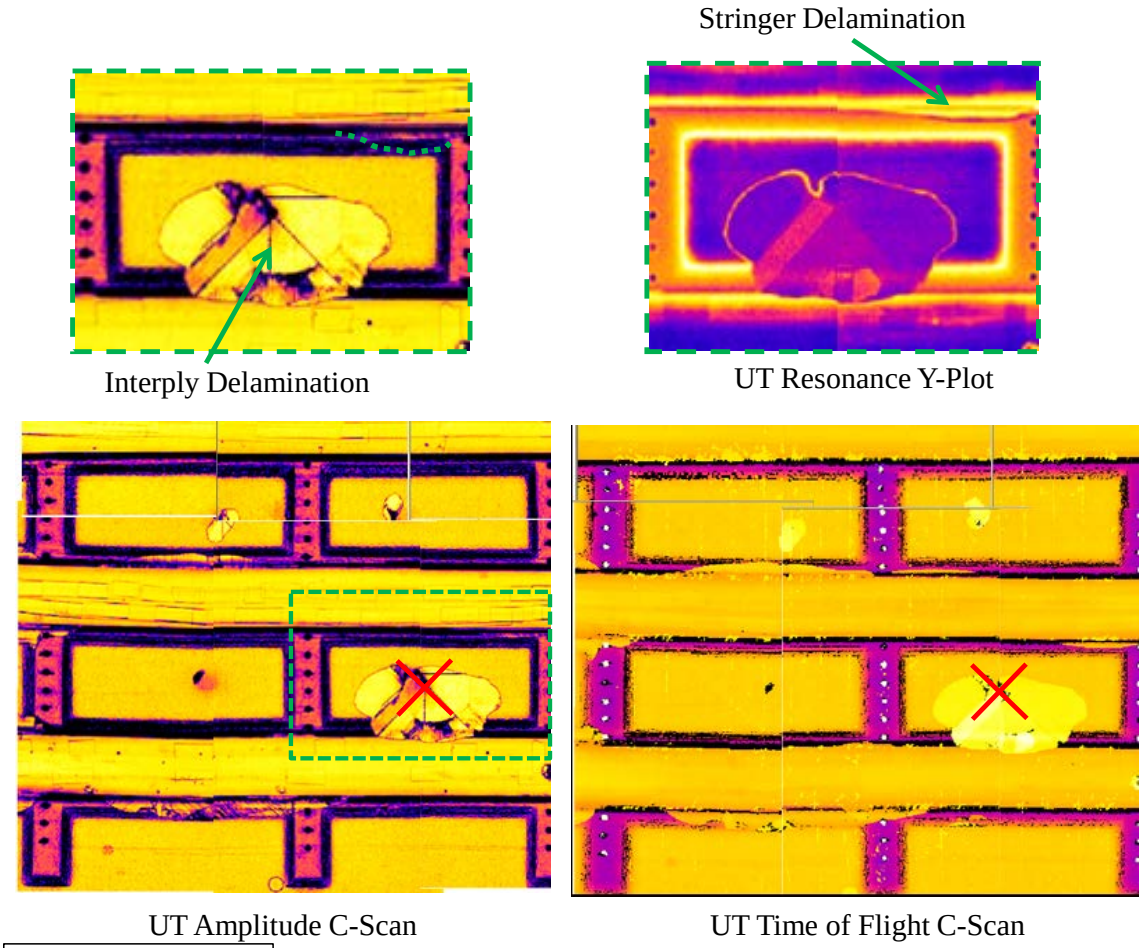

Figure 92. Damage created by ice impact at location 5A (mid-bay skin impact) on panel A

An example of damage induced by an ice impact at the edge of a stringer flange is shown in figure 93. The quadrant view C-scan at the bottom of the figure shows that the impact was directed midway between two shear ties at the edge of a stringer flange. The impact energy of the ice ball was 278.9 Joules and caused the stringer flange to fully disbond. The two shear tie built-up pad sections helped to resist the flange disbond from continuing farther. Additionally, there was a visible crack at the flange-skin interface along the length of the stringer. This is indicated in the center UT amplitude scan with a green dashed line on the stringer.

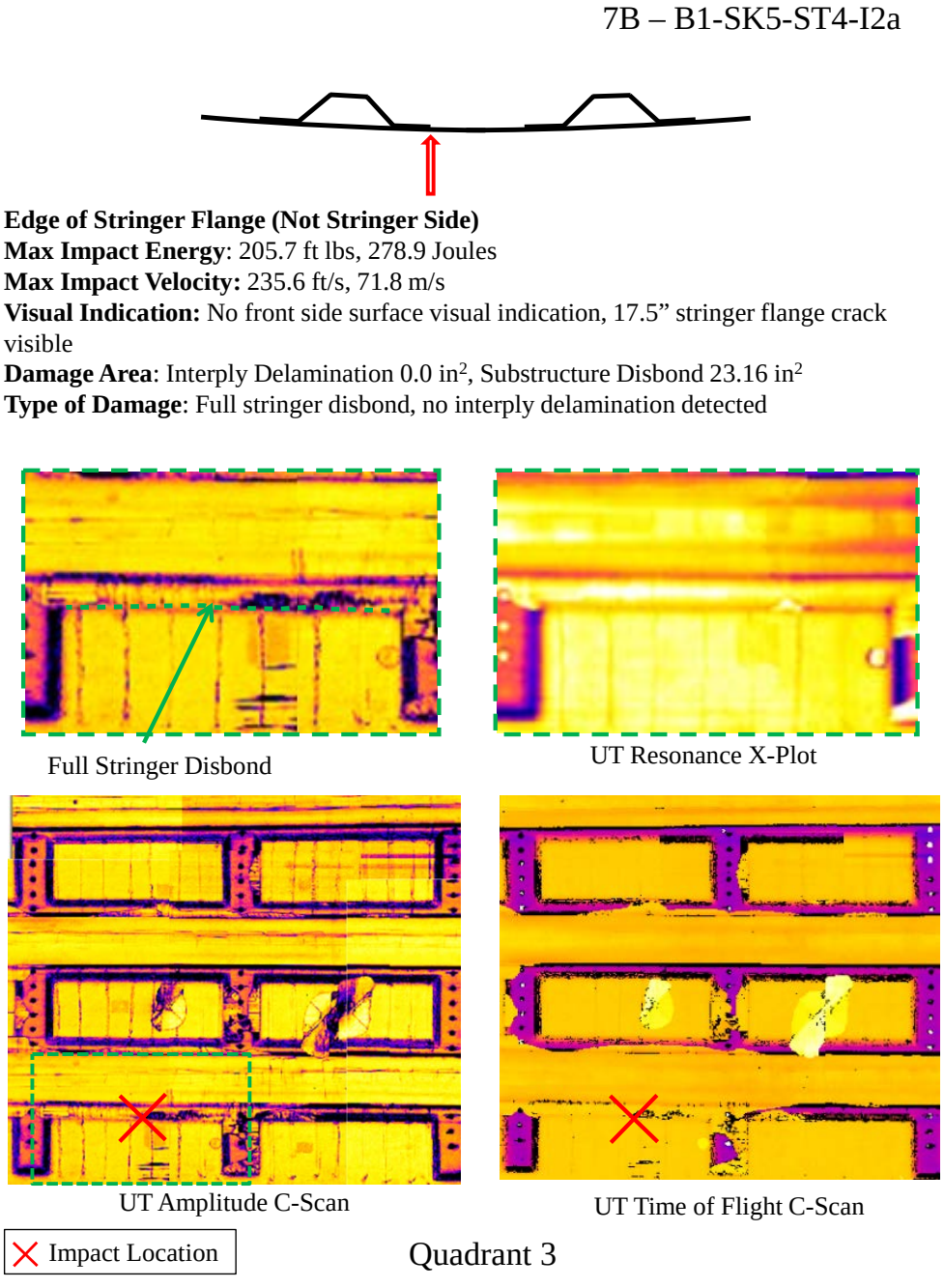

Figure 93. Damage created by ice impact at location 7B (edge of stringer flange) on panel B

4.2.3 Ramp Check Device Results Applied to Full-Scale Panels

Use of RDC equipment in regions of changing geometry – Inspections performed using the RDC unit on full-scale composite fuselage panels proved to be difficult on impact locations over substructure because of the tapered geometry of the stringer and shear-tie co-bonded areas. It was determined that use of the unit was straightforward over mid-bay regions and on the flat plate panels. However, the inspector must have significant knowledge of any tapered region, bonded substructure, and thickness changes behind the skin. Because of the continuously changing thickness of the taper regions, it is difficult to apply this equipment to tapered portions of the structure. Tracing out the substructure on the skin of the panel was necessary to perform initial calibration of the unit and ensure that the initial calibration measurement was taken at the same thickness section of the panel as the desired inspection region. If the probe was moved as little as 1/8″ perpendicular across a taper region, the message provided by the unit would state "out of calibration thickness" during subsequent inspections on stringer and shear tie built-up sections (i.e., equipment setup that is conducted on thinner regions will not accommodate inspections on regions of greater thickness). This should not result in a false call but will be confusing to the user and probably end in a "no decision" for the area of interest.

4.2.4 Laser UT and Projection Thermographic Damage Detection

Laser UT inspection was used to inspect one of the full-scale panels. Figure 94 shows UT amplitude C-scan results obtained from panel A. The curvature of the fuselage panels is relatively gradual and the part was considered flat from the LUS point of view. The delaminations caused by the SHI are clearly imaged in the LUS amplitude scans as well as the hard tip impacts generated by the drop spear. The laser UT inspection provided the highest resolution inspection of all the methods applied to the panels. Even subtle details, including ply orientation within a delamination, can be estimated using the LUS method. Additionally, "slicer" mode can be used, which allows the user to look at a C-scan cross section at any point in time, anywhere within the thickness of the part being inspected. This feature can help to isolate ply depth of delamination and has potential benefits with inspection repairs.

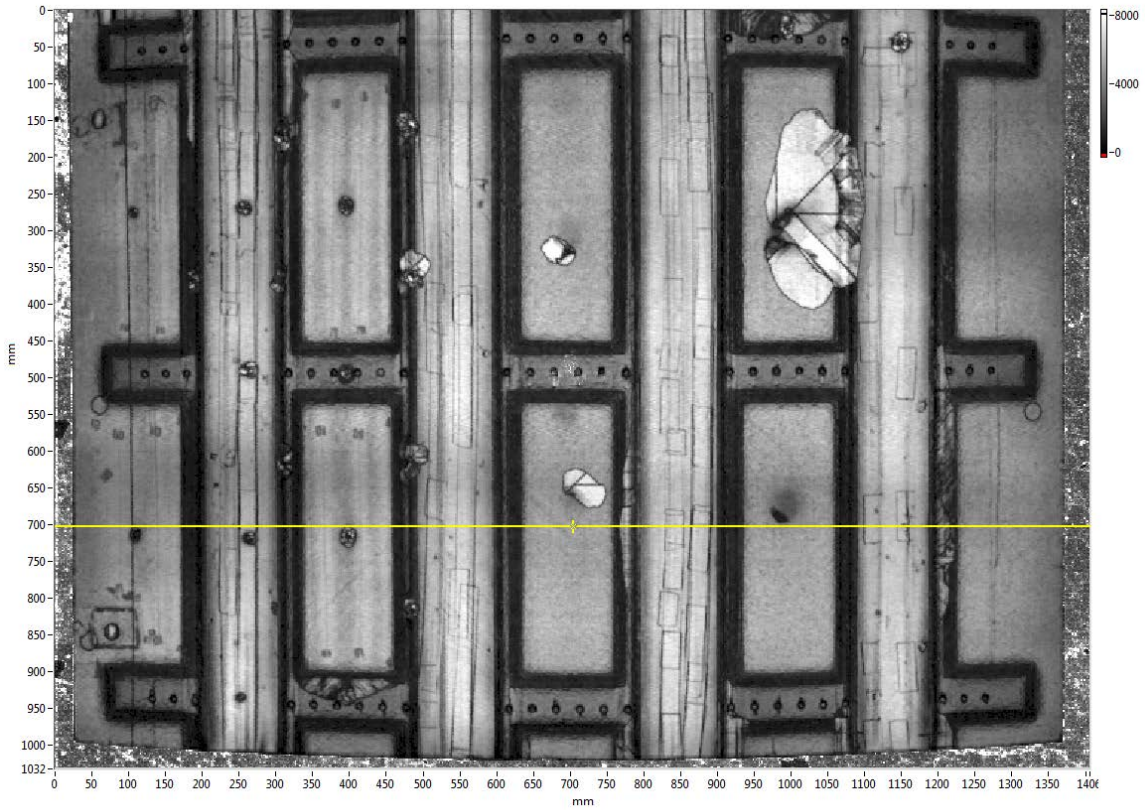

Figure 94. Amplitude C-scan result for laser UT inspection of full-scale fuselage panel

The previous LUS image presented was an amplitude C-scan of half of a panel with the LUS scanning head posed at one position. Figure 95 shows a TOF scan of a full panel taken with the LUS scanning head from one position. It took approximately 30 minutes for this particular scan to cover the entire panel. The TOF image clearly indicates delaminated stringers and built-up pad sections, as well as interply delaminations.

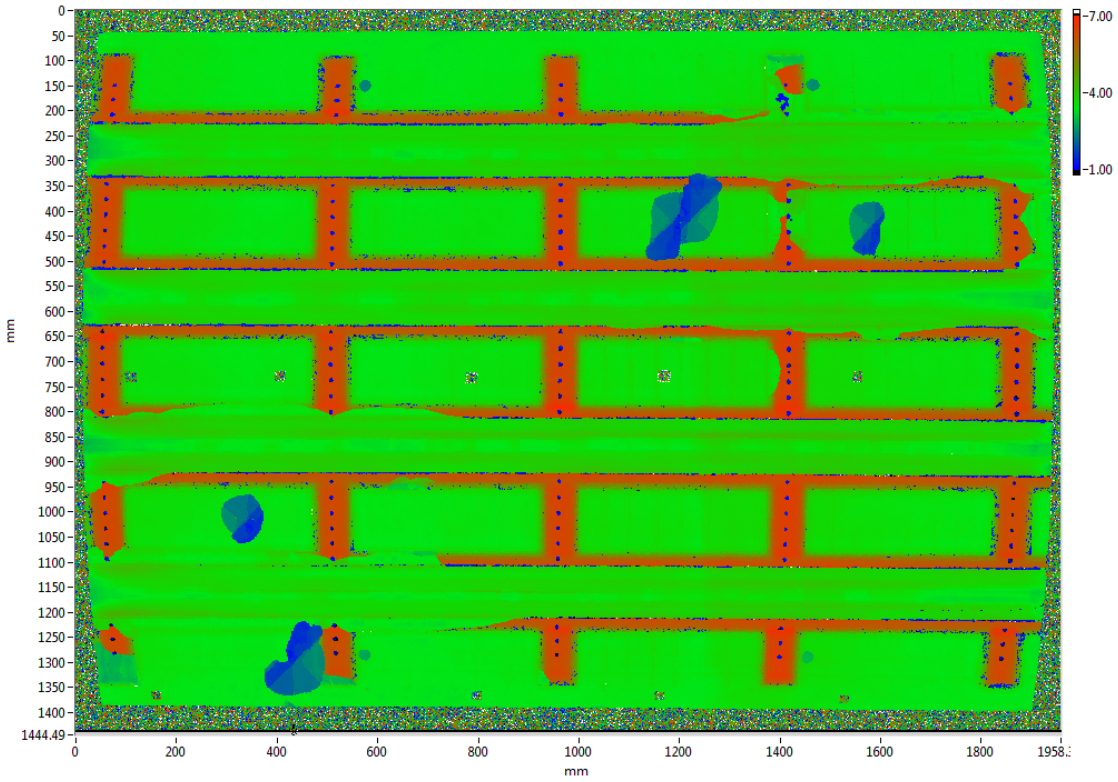

Figure 95. The TOF C-scan result for laser UT inspection of the full-scale fuselage panel

The LUS technology offers flexibility and faster inspection cycle time than other high-resolution inspection options. However, even though LUS signals are UT signals, there are some differences with the UT signals obtained with conventional UT transducers. Those differences must be understood when trying to adapt processing and analysis techniques coming from decades of experience using piezoelectric transducers. Key advantages of laser UT are: 1) the ability to scan quickly in a non-contact mode, all the way to the edge of a part and 2) the ability to launch a through-thickness longitudinal wave even when the laser beam impinges on the surface at an angle. This means that the laser beam can be directed at the surface of complex shapes and scan them efficiently without the need for contour following, complicated scan shoes, or angled water jet arrangements. A laser beam can also be directed through apertures to scan the interior of a structure. Disadvantages of laser UT include: 1) their sensitivity to surface coatings (variations in coatings can affect the strength of the UT signal), 2) the requirement that, for maximum sensitivity, tuning be done for each structure type, 3) the need for system expertise/training to ensure alignment to produce a uniform signal, and 4) safety concerns necessitating personnel exclusion zones.

Projection thermography, a recently tested wide area method of thermographic damage detection, was also applied to one of the full-scale panels at TWI. The projection thermography system developed by TWI uses two heat projectors to apply a thermal load to the part being inspected from a distance. To detect damage, an IR camera mounted on top of the heat projectors measures the surface temperature change as the part cools. A benefit to using this system is that, unlike other thermographic techniques, no surface preparation or coatings are needed. A picture of the system used to inspect panel A is shown in figure 96.

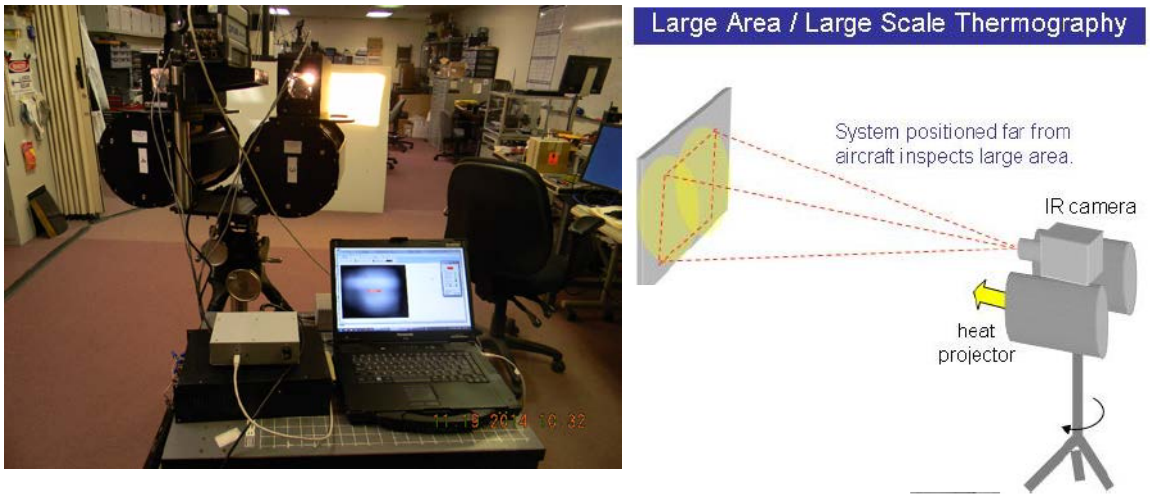

Figure 96. The projection thermography system being used to inspect panel A

Heat was applied to the surface of the panel for approximately 10 seconds from a distance of 10 ft. Surface temperature data were then collected at a frame rate of 20 Hz for approximately a minute and analyzed using TWI's ProjectIR system. Results obtained using the projection thermography system to detect composite impact damage is shown in figures 97 and 98. Each image (shot) obtained with the system took approximately 30 seconds to collect. Because the technique covers approximately four square feet per shot, wide area rapid inspection is possible using the system. When compared with the UT C-scan, it can be seen in the inspection results that a majority of the damage contained in the panel was detected, with the exception of some of the smaller delaminations.

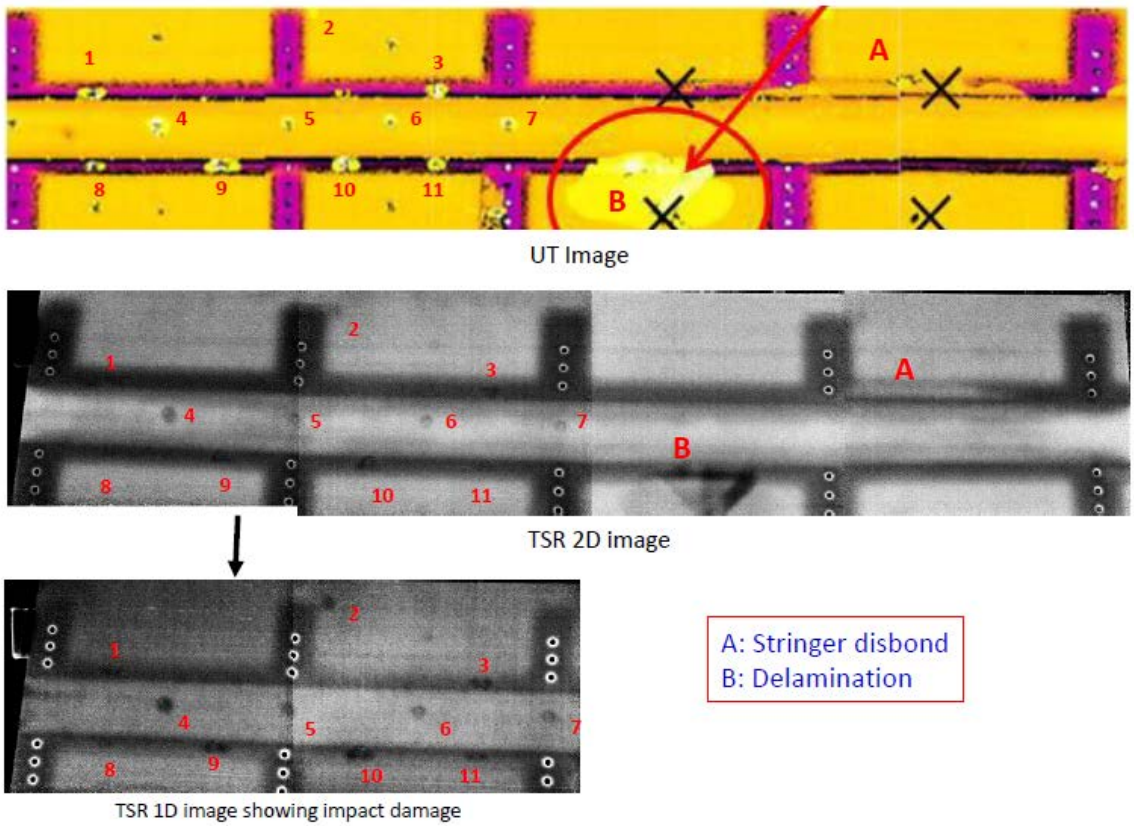

Figure 97. Projection thermography inspection results on panel A

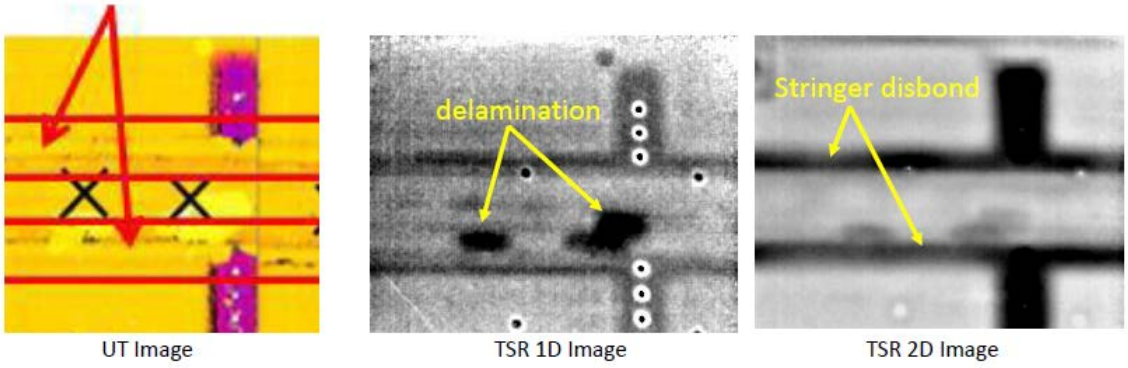

Figure 98. 1st and 2nd derivative thermal signal reconstruction images of delamination and stringer disbanding

4.2.5 Damage Detection

There were four different methods used to deploy FO for strain sensing on the two panels:

1. Embedded within the skin of the 16-ply laminate (panel A)
2. Bonded to the panel perpendicular to the stringers with the fiber being bonded to each skin and stringer in the same orientation and layout as the embedded fiber (panel B)
3. Bonded to the backside of the panel to only the skins parallel to the stringers (bays 1 and 2 on panel A)
4. Bonded to the backside of the panel perpendicular to the stringers—but not bonded to the stringers, only the skins (bays 3 and 4 on panel A)

An initial interrogation of the embedded fiber revealed significant light attenuation within the fiber and that light could not be transmitted through the length of the fiber. The majority of the FO was run in the 90° fiber direction and the fiber toes on either side of the embedded fiber were run at -45° and 0°. When the panel was cured under high pressure in the autoclave, the carbon fibers were pressed tightly, inducing microbending along the length of the fiber. Microbending of the FO is illustrated in figure 99. The initial intention in selecting a fiber for this application was to select a fiber with a high numerical aperture because such fibers are less susceptible to light attenuation due to microbending. The particular fiber used may not have had as high of a numerical aperture as intended.

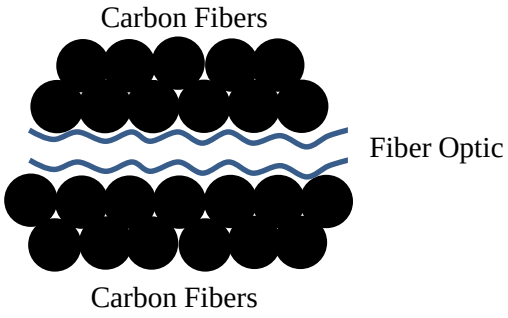

Figure 99. Microbending of embedded FO causing light attenuation

Although there was significant light attenuation in the FO and light could not pass all the way through the length of the fiber, two sections of fiber could successfully be interrogated using the two fiber egress connection points. Each side of the fiber could be interrogated for approximately the first five vertical runs of fiber but was successful only for the first impact test. The resulting strain map is shown in figure 100. A major factor contributing to the lack of data obtained from the embedded FO was the use of high-power flash lamps during the impact tests. The lamps were used to illuminate the area for the high-speed cameras to capture video during each impact. This had an inverse effect on the detection ability of the FO strain-sensing system because the flash lamps increased the surface temperature of the panel. Baseline measurements were taken prior to impact and obtained at an ambient temperature with the flash lamps off. When the data were later interpreted, it was clear that the heat from the lamps induced global strain changes in the panel and

swamped out any indication of impact damage. A color strain map result from the first impact test conducted on panel A is shown in figure 100.

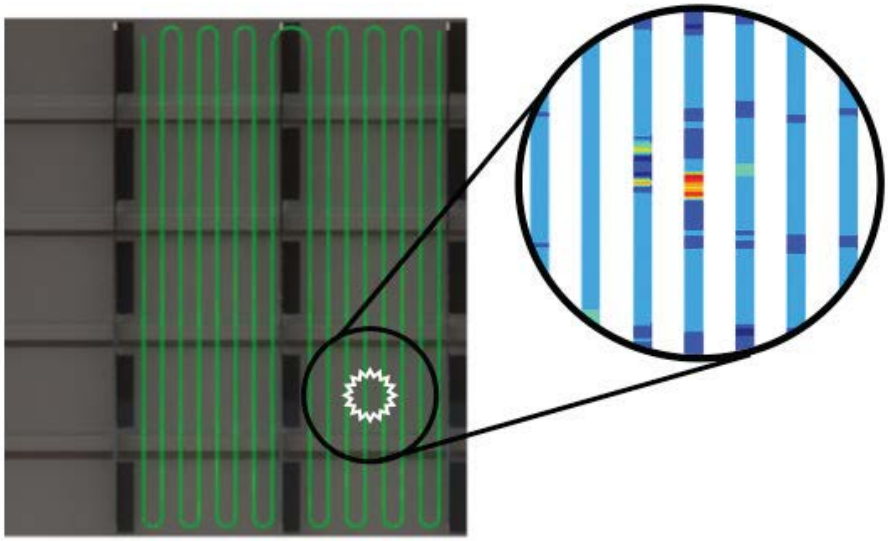

Figure 100. Strain map of first impact damage performed on panel A; only results obtained from embedded FO

Damage detection using the FO that was externally bonded to the skins and stringers was equally unsuccessful during SHI testing. Because the FO was bonded to both the skin and the stringers, when an impact occurred that delaminated the stringer flange from the skin, it broke the FO. An example of a delaminated stringer flange shearing the FO sensor (white line) is shown in figure 101. No results were obtained using this method of FO deployment due to extensive fiber breakage.

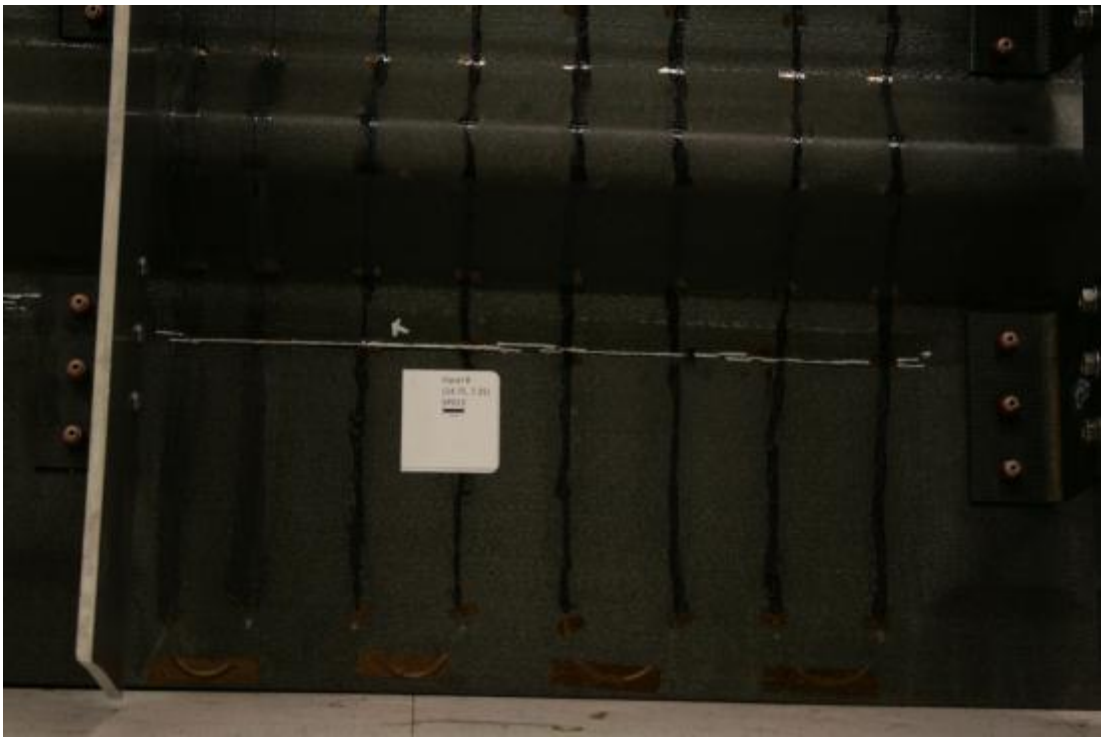

Figure 101. Broken FO due to stringer flange delamination

In response to the ineffective method of FO deployment used during SHI testing, two alternative methods were investigated that did not involve bonding the fiber over the stringer during hard impact testing. The two different layouts tested are shown in figure 102. In the fiber layout used in bays 1 and 2, the fiber was bonded parallel to the stringers. At each stringer flange, one strand of fiber was bonded just to the outside of each flange, and one was bonded just on the flange, but never bonded over the interface. In the fiber layout used in bays 3 and 4, the fiber was run perpendicular to the stringers, but the bond was stopped prior to the skin-to-flange intersection. Both of these layouts left unbonded sections of fiber, which were exposed to potential breakage during handling.

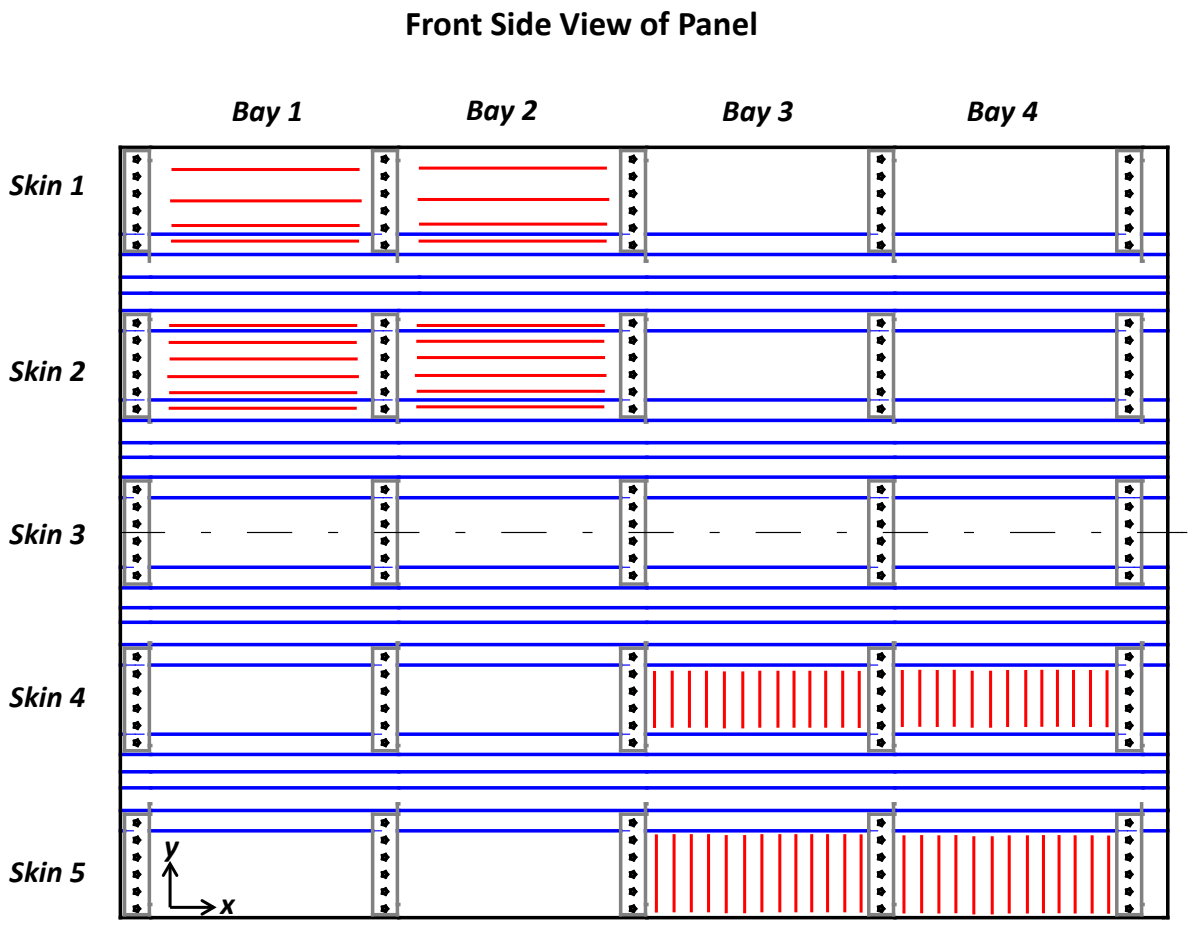

Figure 102. Bonded FO layouts used during 2″ diameter, spherical tip impacts

A picture of the two different FO layouts is shown in figure 103. Bay 2, on the left of the figure, shows the horizontal fiber runs that were unequally spaced apart. The spacing between the two fibers at the edge of the stringer flange (one on the edge of the flange and the other on the skin) were placed close together to better detect stringer disbonding. There were 20 bonded sections of fiber over the two skins. The right side of the figure shows the FO layout used in bays 3 and 4. There were 26 bonded sections of fiber in 13 vertical runs.

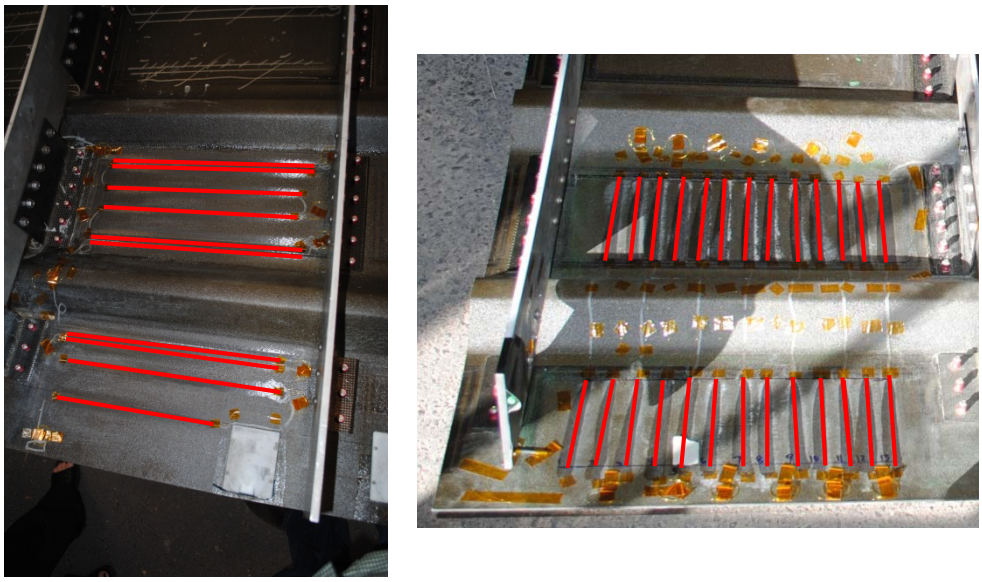

Figure 103. Picture of bays 2 and 4 showing where the FO was bonded to the panel

Baseline scans of the FO were taken prior to each impact event and collected within minutes of the impact test. To calculate strain, the system measured minute changes in the Raleigh backscatter between the baseline and post-test scans. A 1 cm strain resolution was used to interrogate the bonded FO. The OBR recorded linear strain data every 1 cm for the length of the entire FO. As shown in the previous figures, only certain portions of the fiber were bonded to the panel. The strain position data were used to determine the locations along the length of the fiber that were bonded and unbonded. Location calibration was accomplished by touching the fiber (changing the strain) at the beginning and end of each bonded section of fiber. Those specific fiber-length positions were found in the dataset and alternately plotted in a strain map. Because the data output from the OBR consisted of linear strain-position data, each strand of fiber needed to be plotted in the opposite direction of the previous strand. This is illustrated in figure 104.

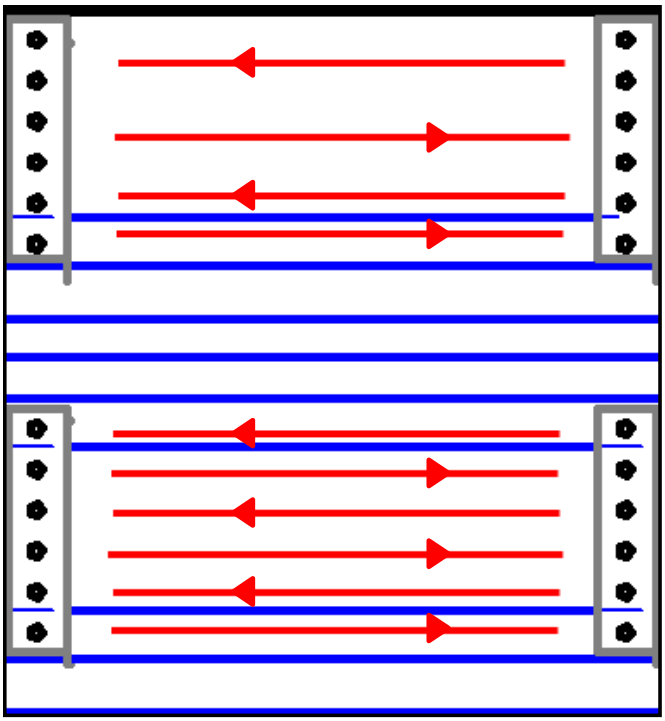

Figure 104. Linear strain position used for data plotting

A sample result constructed using the fiber orientation in bay 2 is shown in figure 105. This particular impact was successfully detected using the bonded FO. A noticeable strain indication of approximately 120 microstrain is shown in the 3D strain map at the bottom of the figure. Also seen in the 3D strain plot is a noticeable compressive strain on either side of the impact location, with a positive strain at the center of the impact. This is typical of a dent where the center of the impact corresponds to the peak positive strain of the dent and the compressive strains on either side correspond to the base (reverse bending) of the dent. The full set of strain map results for this fiber orientation and the vertical fiber orientations used in the hard-tip spherical impact tests are shown in appendix C.

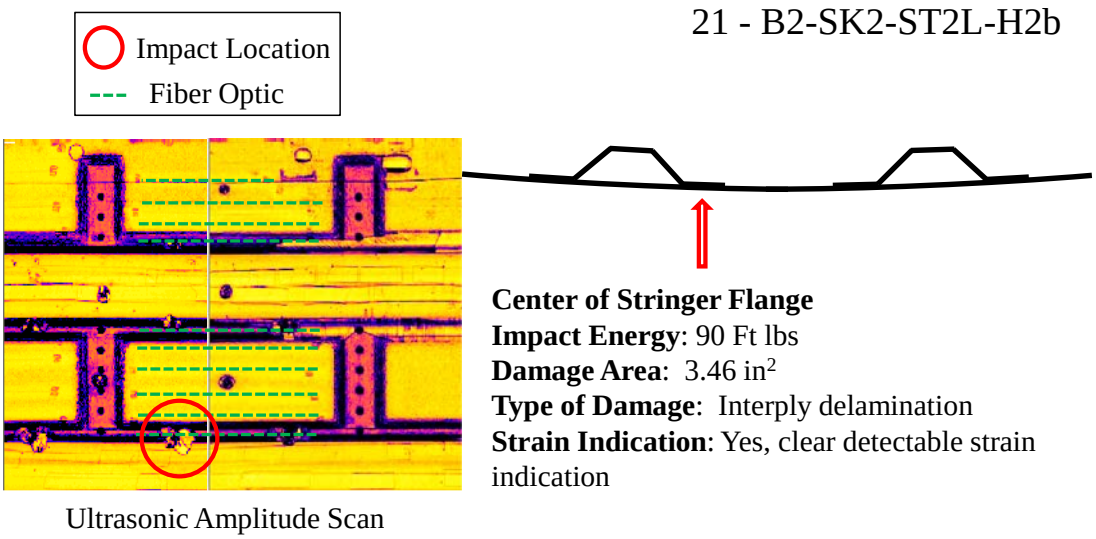

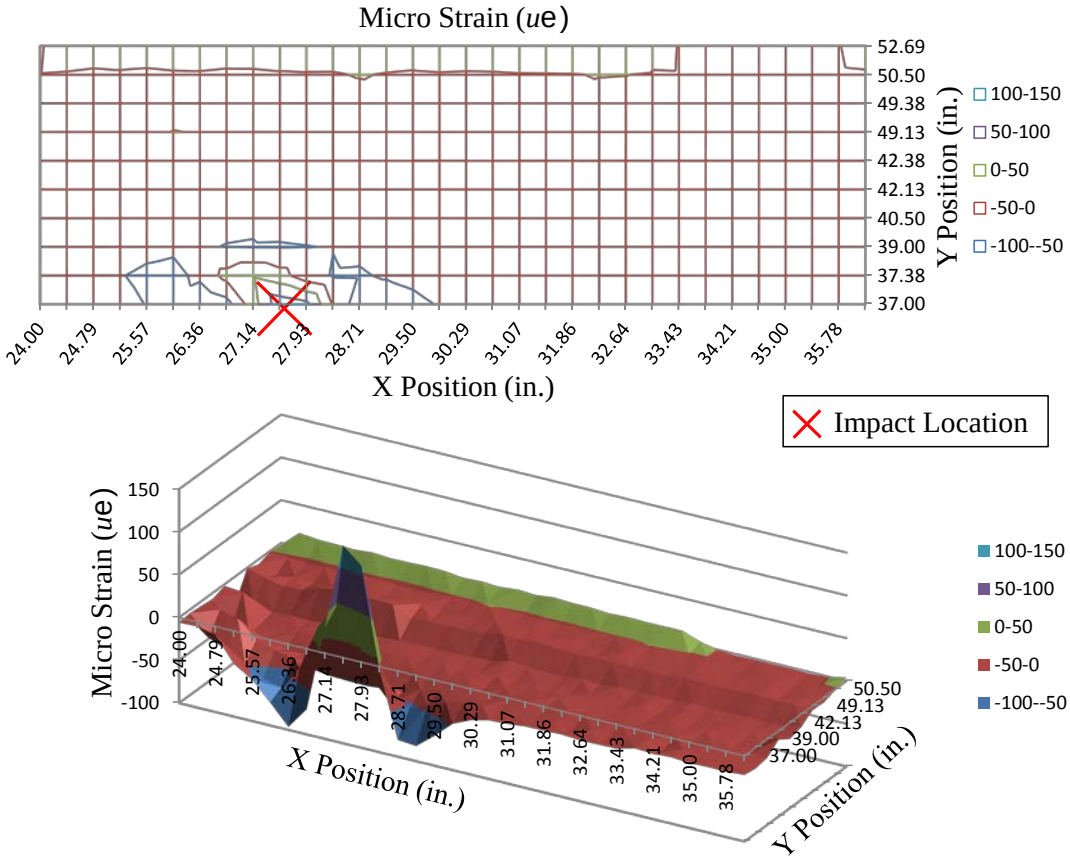

Figure 105. Example FO strain map of stringer flange impact

This set of results revealed that the vertical fiber orientation detected more impact damage than the horizontal fiber orientation. This was because the vertical fiber orientation (bays 3 and 4) was regularly spaced at approximately 1″, and the horizontal fiber runs were spaced at approximately 2.6″, 1.1″, and 0.25″. The closest spacing was placed on either side of the stringer flange-to-skin

transition. Deformation of the back side of the panel had to be in contact with the fiber for the FO to detect any strain indication. For example, skin impact damage generated between the stringer flanges (impacts H3) did not produce a detectable indication because the fiber was not bonded in this region.

Global changes in the strain field were occasionally noticed in some of the post-impact strain plots. This may have been attributed to shifts in temperature between the initial baseline measurement and the post-impact measurement, or movement of the panel during testing. Typically, these were observed in tests involving no detectable strain indication of damage and a relatively low maximum strain over the length of the fiber. An example of a non-detectable impact damage and the resulting strain field measurements is shown in figure 106. This impact was conducted on the skin between the stringer flanges. It can be seen in the impact schematic in the top right of the figure that significant deformation at the impact site, including stringer flange disbanding, would have to occur for the FO to detect the strain change from this impact. It can also be seen in the UT amplitude C-scan at the top left side of the figure that there was very little damage (i.e., 0.47 in^2 of near surface fiber crushing) induced by the impact.

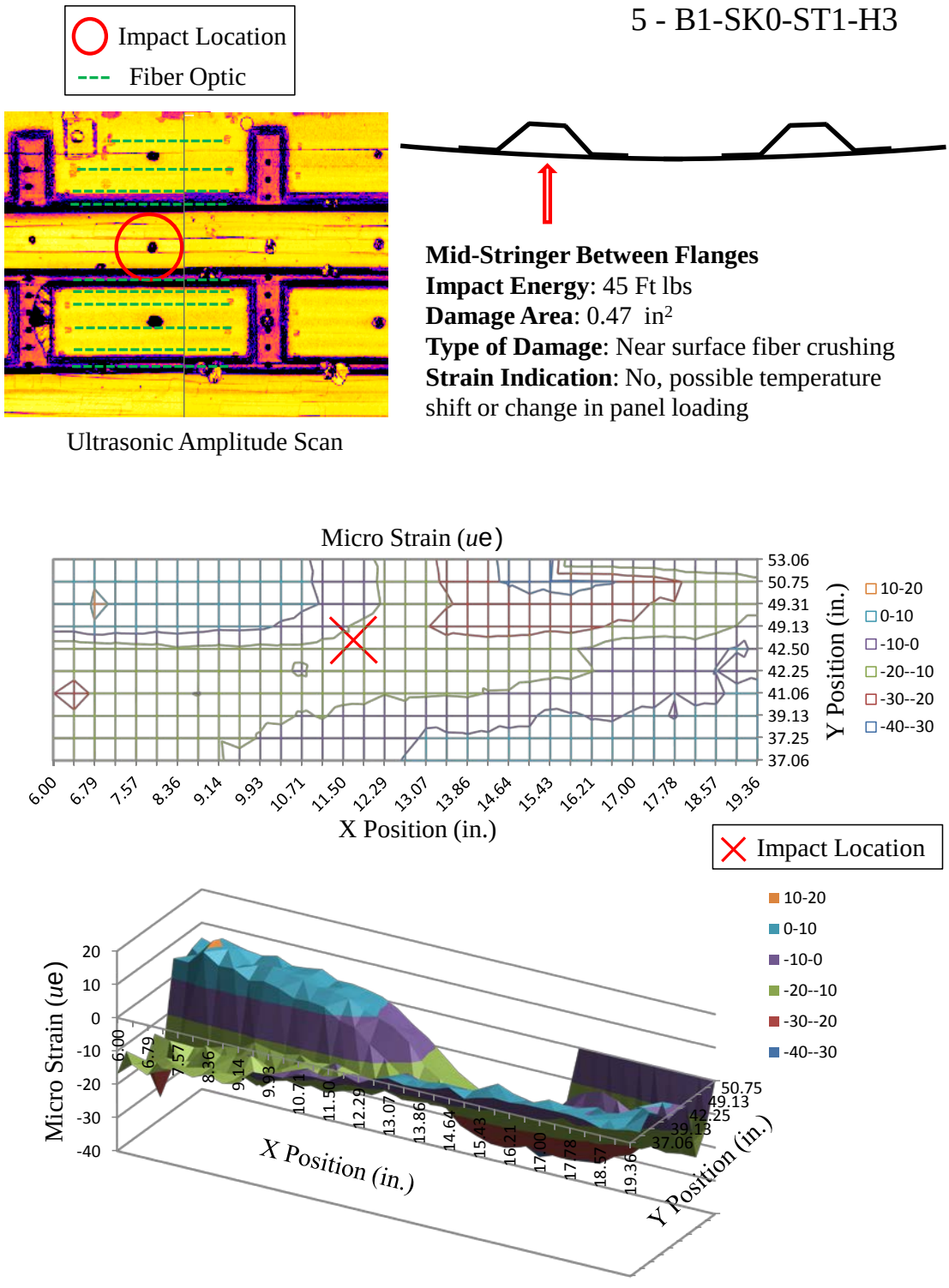

Figure 106. Impact at mid-stringer between flanges that was not detectable with the FO

4.2.6 Damage Associated With Hail Impact

There were three main types of damage associated with the hail impact damage imparted on the panels. Depending on the location of the impact, the corresponding damage could be interply delamination in the 16-ply skin, disbonding at the skin-to-stringer flange interface (substructure delamination), delamination between the plies of the built-up shear tie pad, or shear tie cracking. Interply skin and substructure delamination were detectable with the NDI techniques used, but shear tie cracking was detectable only visually from the backside of the panels. An example of a visually detectable disbonded stringer flange is shown in figure 107, and an example of a cracked shear tie is shown in figure 108. The fractures in the shear ties were observed to occur in the vertical flange at the radius. Thus, UT inspections from the skin side could not detect this damage.

Figure 107. Stringer flange delamination detectable from backside of panel A

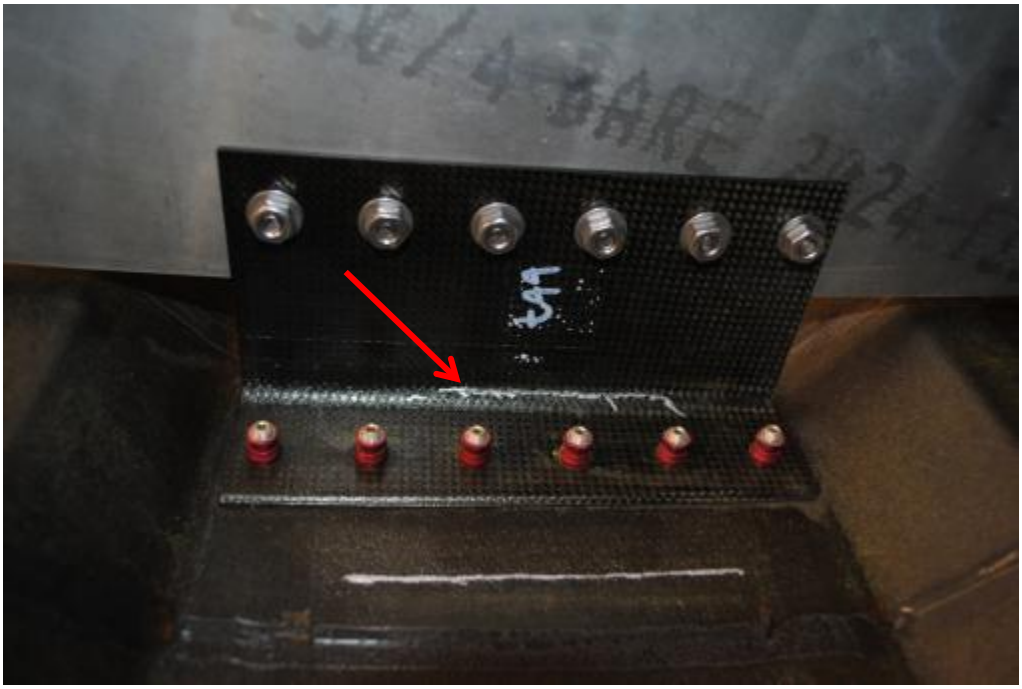

Figure 108. Crack on shear tie bend radius not detectable using NDI from front side of panel

4.2.6.1 Mid-Bay Impacts (Type I1)

Damage created by mid-bay hail skin impacts included both substructure and interply skin delaminations. Figure 109 plots the hail impact energy versus the resulting damage size. The calculated damage area associated with each impact can be found in the tables in appendix C; the information for each impact and the corresponding inspection images are contained in appendix D. As a general trend, the interply delamination created by mid-bay skin impacts increases with impact energy, but not linearly (black diamonds), and is not a very strong trend. Mid-bay skin impacts sometimes caused stringer flange delamination but not always.

Impact locations that were impacted multiple times, starting with low-energy levels, showed that damage onset is somewhat of a binary, bifurcation point. It either happens or it does not. However, there may be some very subtle changes in the local makeup (e.g., microchanges in the resin matrix or a reorder in the distribution of residual strains). Thus, when the FTE is reached after multiple impacts at the same location, the resulting damage could be slightly different than if it had been impacted only once at the highest energy level.

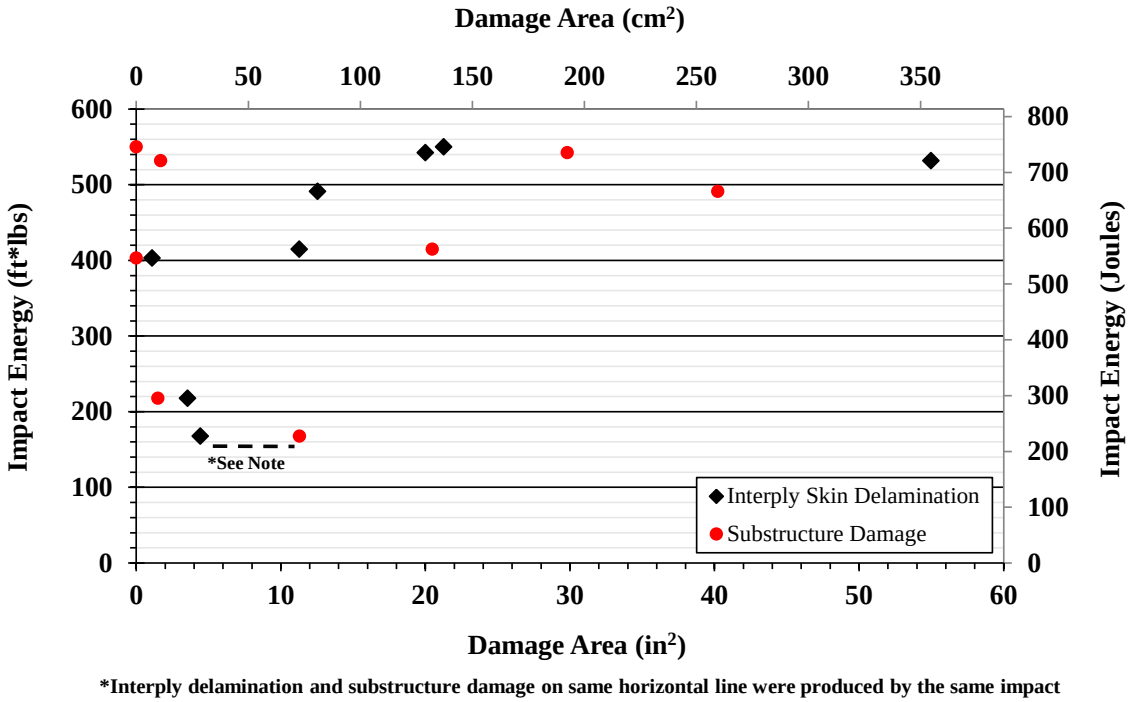

Figure 109. Substructure and skin delamination damage area created by simulated hail, mid-bay skin impacts (type I1)

The total damage area, or combination of substructure and interply delamination, is charted in figure 110. The black bar in the chart indicates the damage contributed by interply delamination in the skin; the red bar shows the damage contribution from substructure delamination. The chart shows that it is difficult to determine when substructure disbonding will occur. There is not a set energy threshold that, when increased from this threshold, causes substructure delamination to occur.

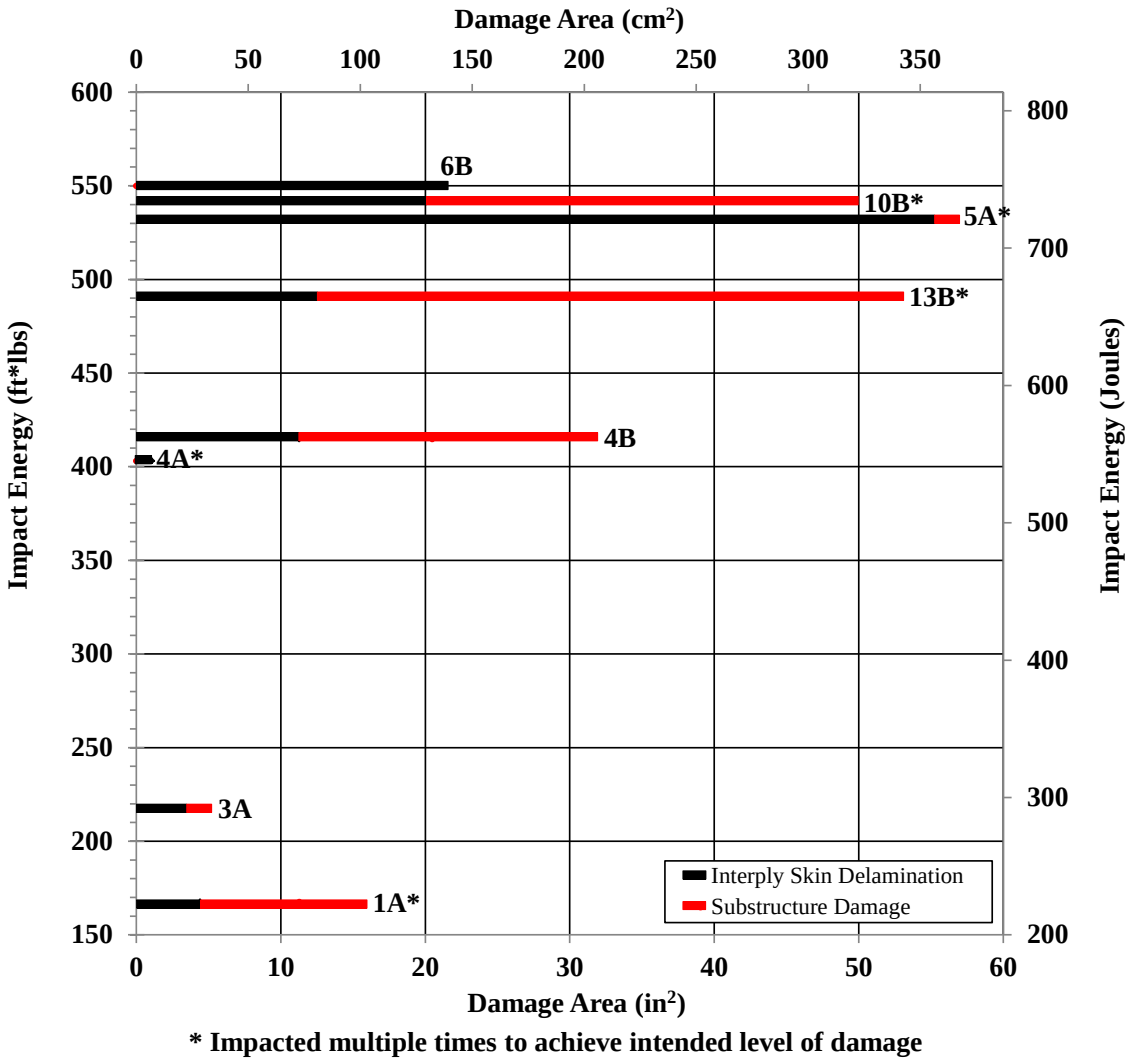

Figure 110. Total damage area created by simulated hail, mid-bay skin impacts (type I1)

The damage produced from mid-bay skin impacts, inspection results with the associated damage area, and the associated impact energy levels are shown in figure 111. The minimum energy level to achieve damage was 1A, at 227.1 Joules.

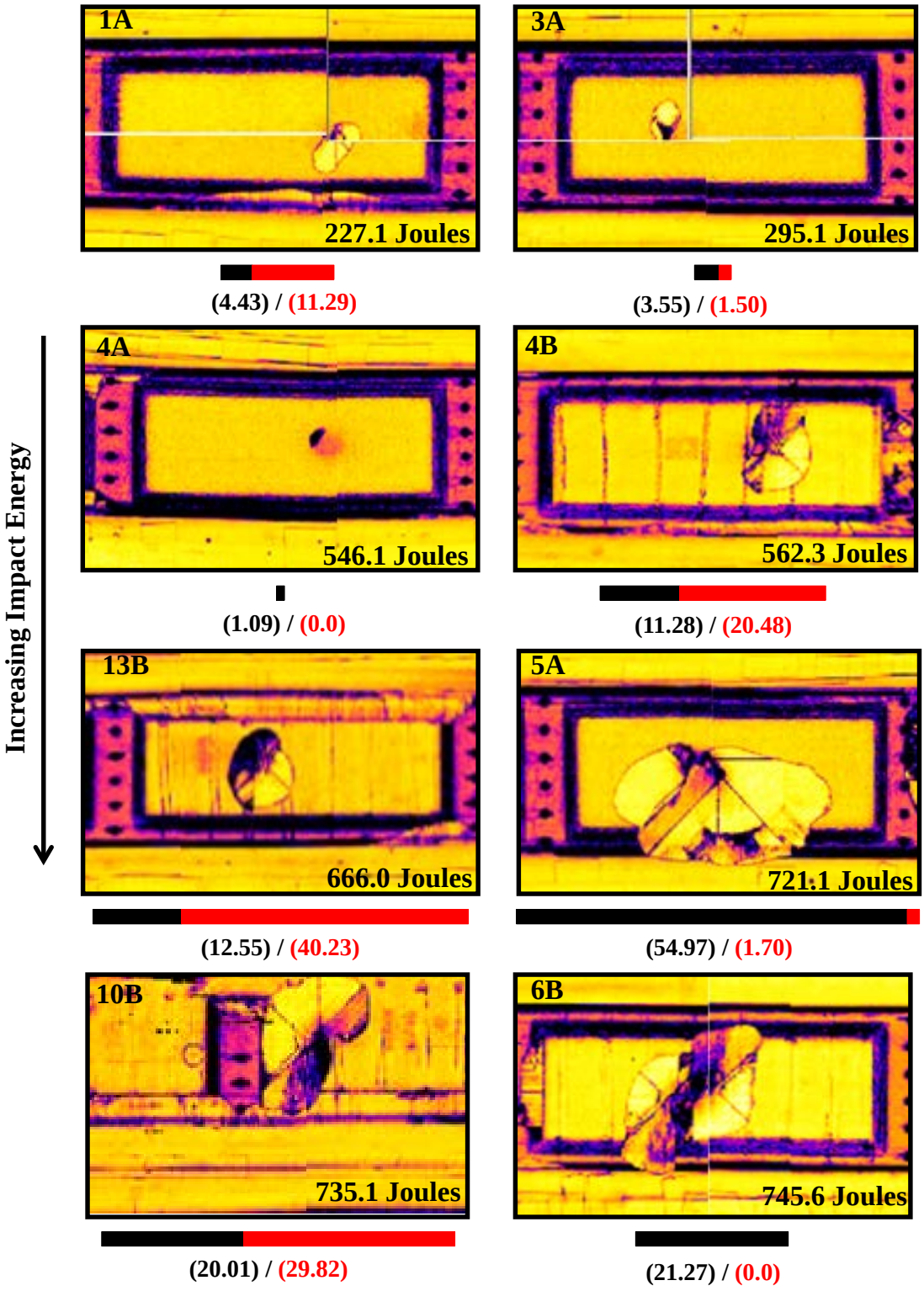

Figure 111. Amplitude C-scan results for simulated hail mid-bay impacts (type I1)

4.2.6.2 Stringer Flange Impacts (Type I2)

These full-scale panel tests investigated impact on both stiffened and unstiffened fuselage structural elements. Impacts conducted at locations over stringer flanges initiated damage at lower levels than impacts over unsupported skin impacts. Figure 112 plots the damage area in both substructure and skin elements induced by SHI over the stringer flange. The plot consists of both 2a and 2b type impacts and was combined for both panels. It was noted that none of the stringer flange impacts caused any type of interply delamination in the 16-ply skin. All of the damage area caused by these impacts was substructure disbonding and typically increased with impact energy. This most likely occurred because of the high peeling stresses that are generated at the edges of the flange when the skin of the panel bends during the impact event. The energy induced into the panel is absorbed through flange delamination and, therefore, does not lead to interply skin delamination. The total area damage plot for these impacts is not provided because it is the same as the substructure delamination area plot (red dots).

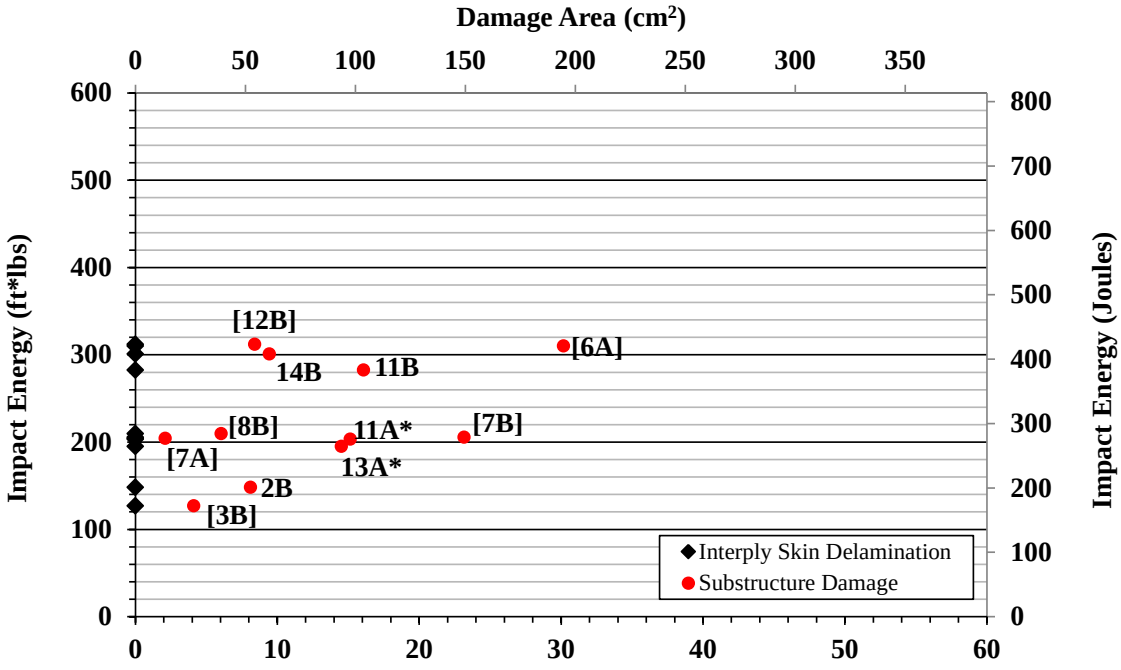

 # With No Brackets– Center flange (2b) impacts
[# With Brackets]– Edge of flange (2a) impacts
*** Impacted multiple times to achieve intended level of damage**

Figure 112. Substructure and skin delamination damage area created by simulated hail, stringer flange impacts

Damage associated with edge of flange impacts (type 2a) is shown in the TOF images in figure 113. TOF C-scans were selected to present this data because they were more sensitive to small delaminations in the stringer flanges than amplitude C-scans. Some of the damage in the TOF C-scans were initiated by other impacts that occurred in close proximity to the impact of interest and was not added in the area calculation for that particular impact. At low-impact energy levels,

a small amount of damage occurred, which did not span the width of the tapered flange. The minimum energy level to initiate damage was 172.2 Joules (impact 3B), as shown in figure 113. There was a small difference in impact energy between impact 7A and 7B, but a significant difference in substructure delamination area. This could potentially be due to the proximity of 7B to the edge of the panel, but this was not observed in other edge bay impacts.

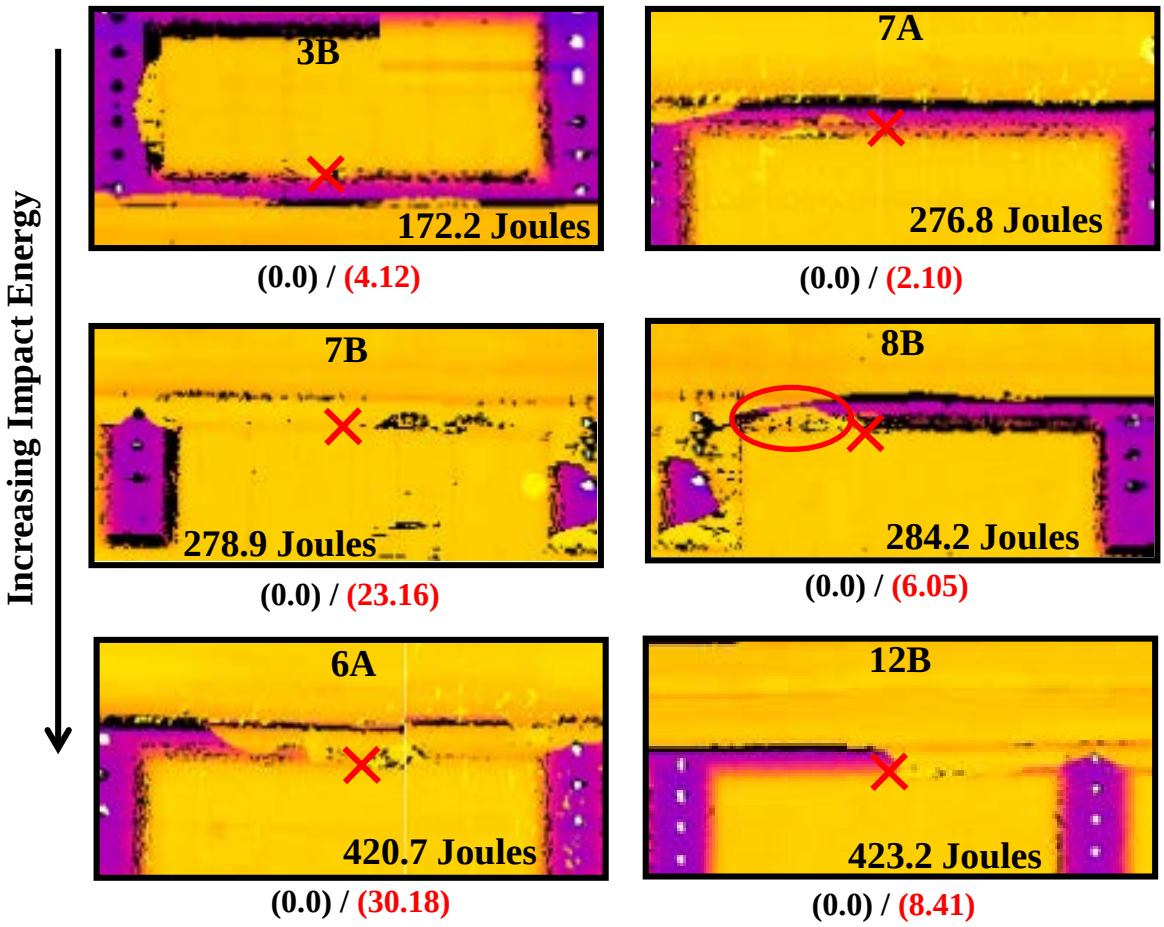

Figure 113. UT TOF C-scans of stringer flange edge impact damage produced by impact at X (type I2a)

Damage associated with center of flange impacts (type 2b) are shown in the TOF images in figure 114. Interestingly, impact 14B was the highest energy impact of this type and showed fairly little delamination at the impact site, but it did cause delamination of the adjacent stringer flange.

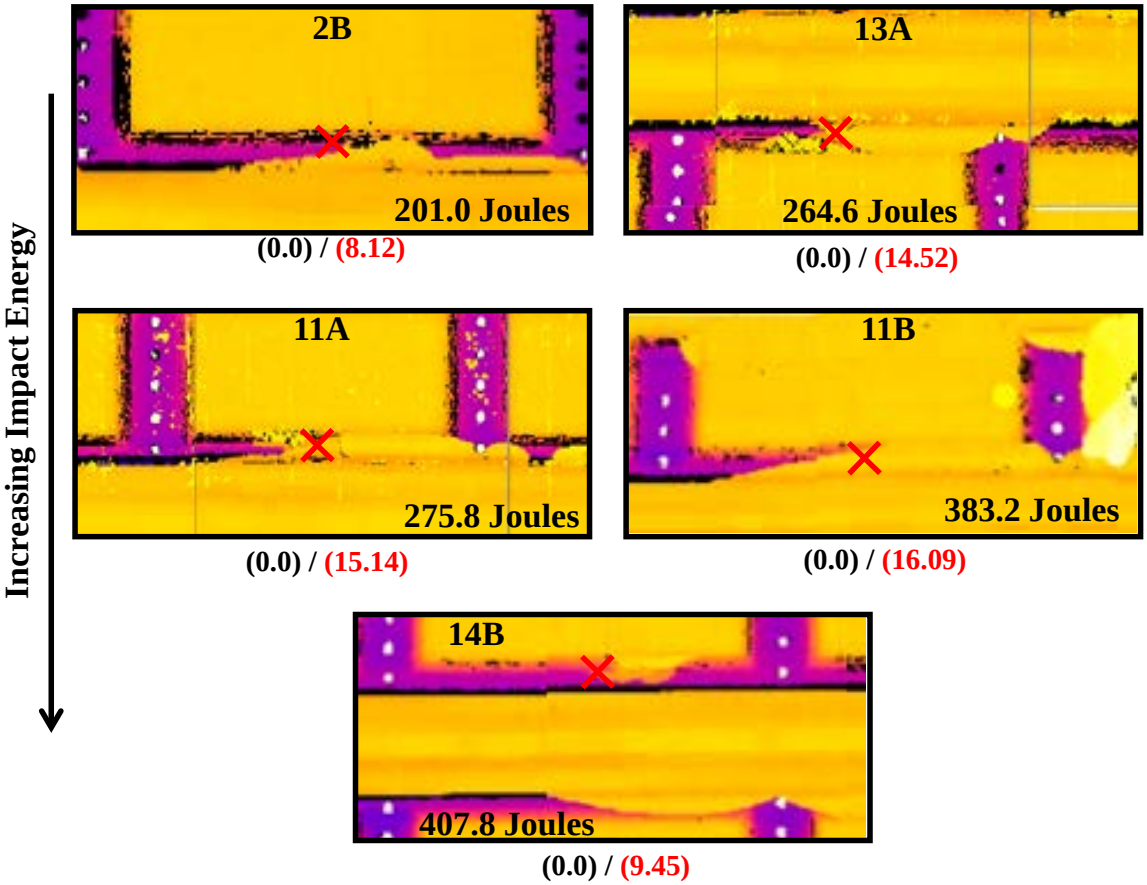

Figure 114. UT TOF C-scans of center stringer flange impact damage produced by impact at X (type I2b)

4.2.6.3 Mid-Stringer Impacts (Type I3)

The damage area induced from mid-stringer hail impacts for both substructure and skin delamination is plotted in figure 115. Similar to mid-bay skin impacts, two of the four mid-stringer impacts generated both interply delamination and stringer flange delamination. To initiate damage at the mid-stringer location, more impact energy was needed than the energy level that produced damage for a mid-bay impact and direct stringer flange impact.

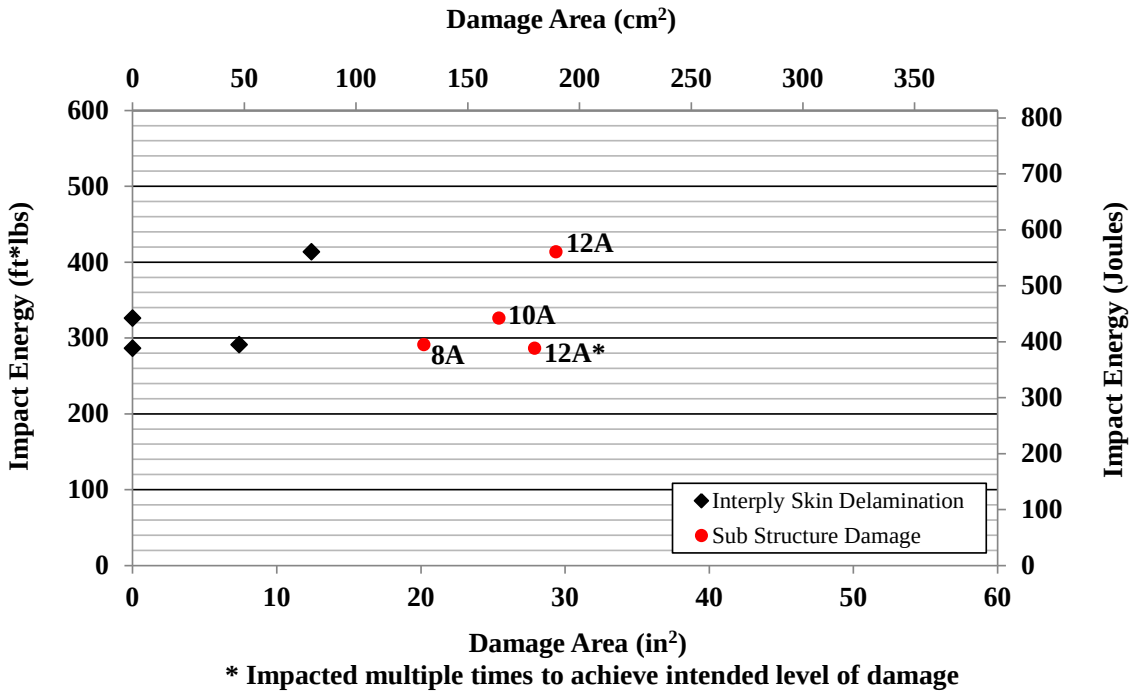

Figure 115. Substructure and skin delamination damage area created by simulated hail, mid-stringer impacts (type I3)

The total damage generated by mid-stringer impacts is shown in figure 116. Although interply skin delamination did occur in two of these impacts, a majority of the damage was caused at the skin-to-flange substructure interface. Because impacts 8A, 9A, and 10A were conducted on the same stringer, the first damage-inducing impact may have had an effect on subsequent, nearby impacts.

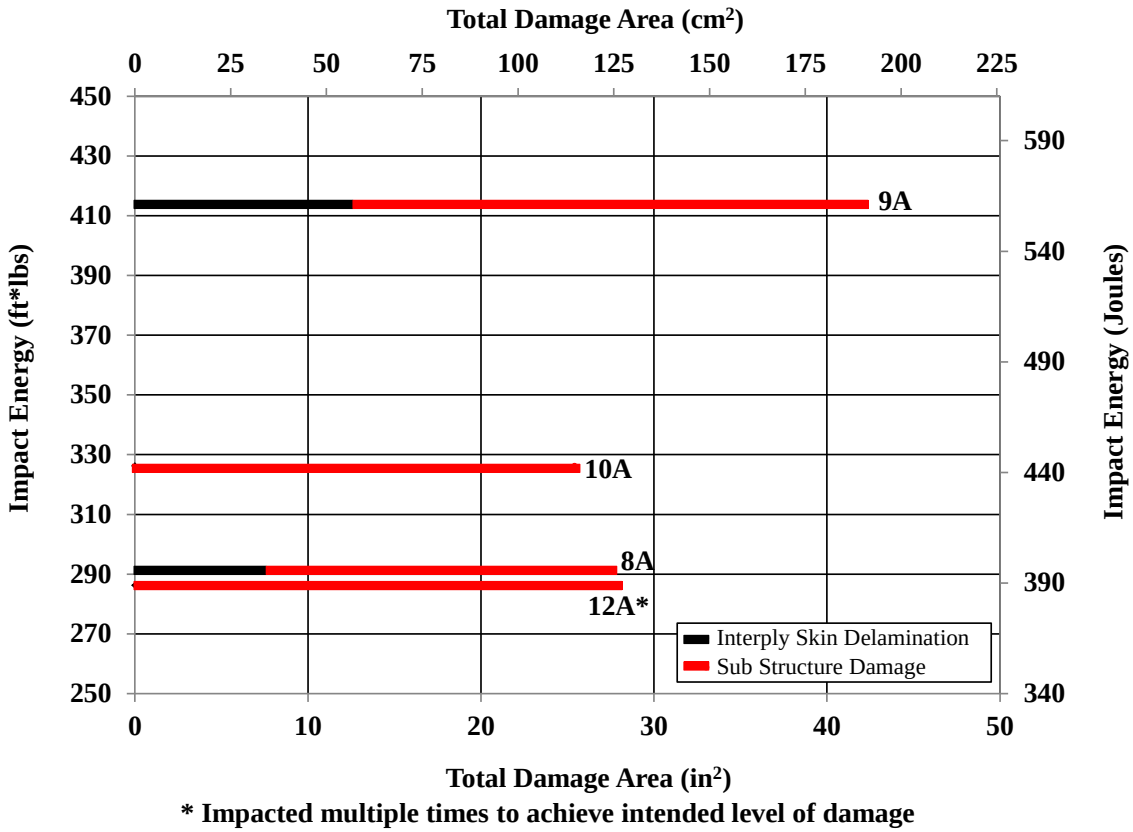

Figure 116. Total damage area created by simulated hail, mid-stringer impacts (type I3)

The UT amplitude C-scans in figure 117 show that all four of the mid-stringer impacts created some level of substructure delamination. There was some difficulty in the assessment of what damage area uniquely was associated with impacts 8A and 9A. Because the two impacts occurred close to each other and both stringer flanges on either side of the two impacts were fully delaminated, the assigned substructure damage within the same bay was split between the two impacts at a line halfway between them.

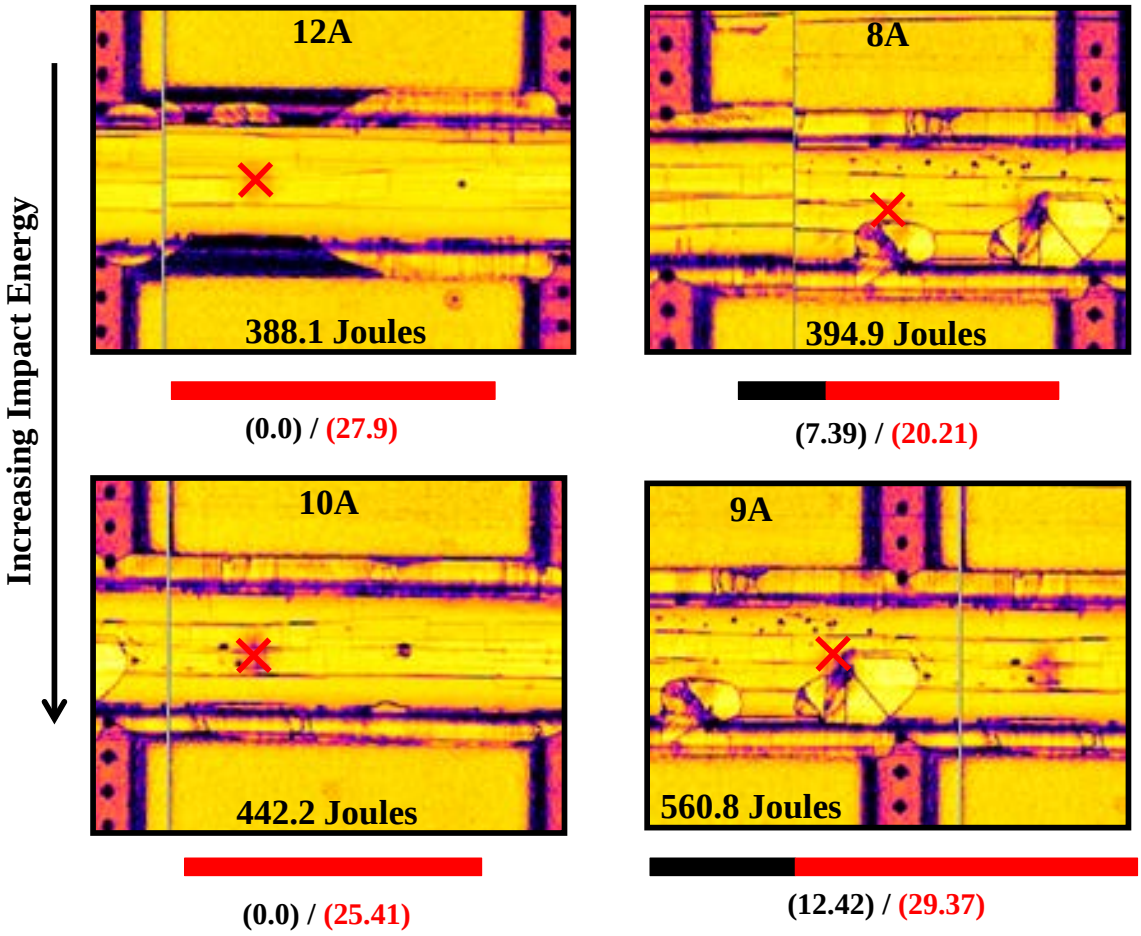

Figure 117. UT amplitude C-scans of mid-stringer impact damage (type I3)

4.2.6.4 Shear Tie Impacts (Type 4)

Damage induced by hail impacts directly on the shear ties consisting mainly of substructure damage or delaminations in the built-up pad sections. Figure 118 shows that there were no interply skin delaminations associated with direct shear tie impacts. Visual inspections revealed that all three of these impacts cracked the shear tie located beneath the impact location (see figure 108). All three of the shear tie impacts also produced visually detectable indications of damage on the outer surface. These visual indications were either paint scuffing, paint chipping, or paint cracking around the fasteners. Additional details regarding the cracked shear ties and visual indications are provided in appendix D.

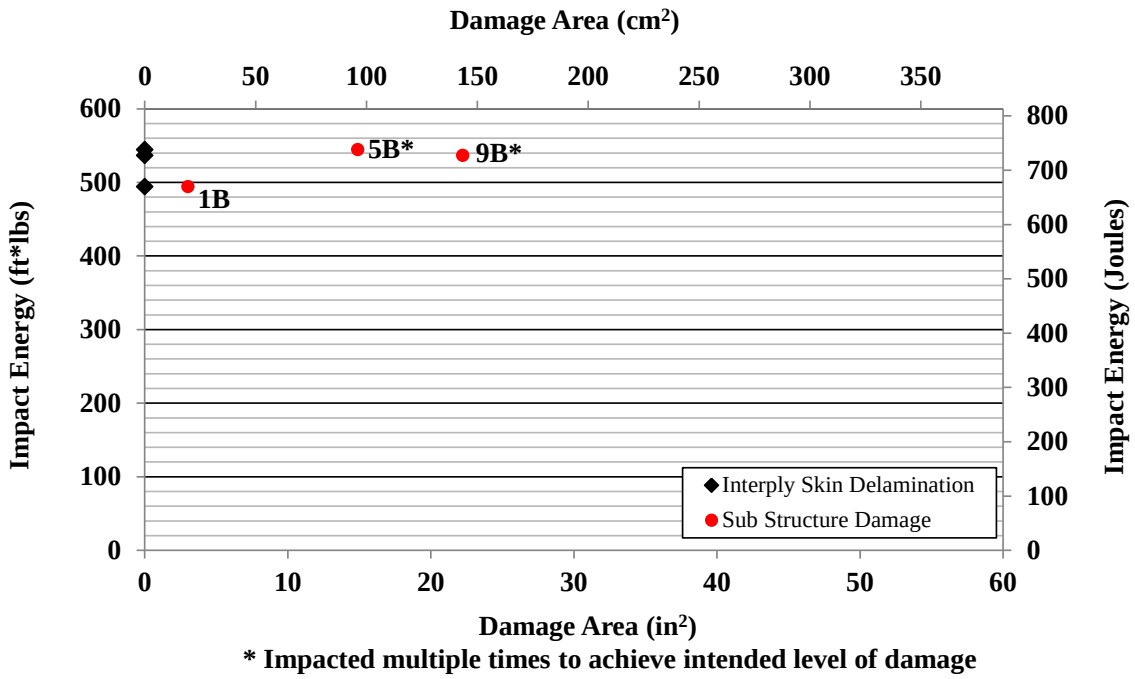

Figure 118. Substructure and skin delamination damage area created by simulated hail, shear tie impacts (type I4)

UT amplitude C-scans for direct shear tie impacts are shown in figure 119. Shear tie damage poses three unique NDI challenges: 1) the shear ties are fastened to the skin, not bonded or co-cured, so the UT signal cannot penetrate into the shear tie to detect damage, 2) the shear tie built-up pad section is typically delaminated during the impact event; therefore, any damage beneath this interface damage would not be detectable, and 3) the share ties are bent at a 90° angle and damage in the shear tie manifests itself as cracking in the radius of bend, which is not in contact with the backside of the panel. It may be possible to detect this damage if there is sealant or another type of UT coupling medium between the shear tie and the built-up pad section or adhesive.

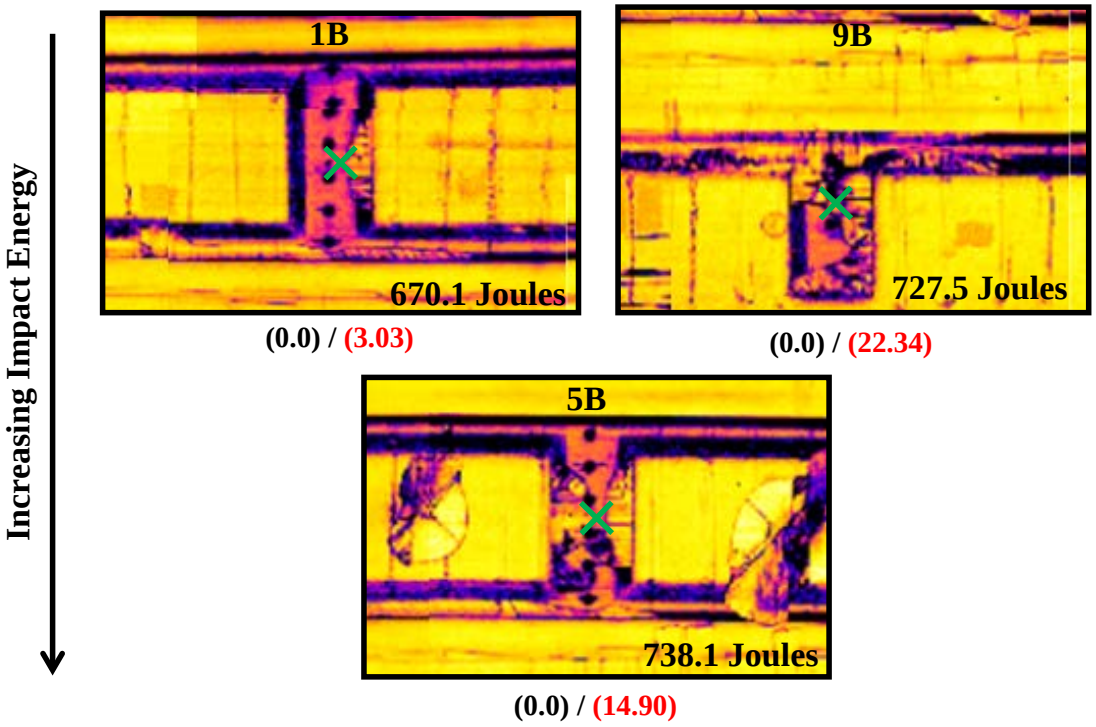

Figure 119. UT amplitude C-scans of shear tie impact damage (type I4)

4.2.7 Damage Associated With Hard Spherical Tip Impact

For hard-tip spherical impact tests, local loss of UT signal at the impact location primarily indicated crushed fibers near the surface and was typically accompanied by a visual dent at the impact site. Furthermore, damage created by the solid spherical tip was localized in that it never initiated damage away from the impact location. Also, because the damage created by the hard tip was significantly smaller than the simulated hail, it was not possible to separate the area of substructure damage from the interply skin delamination area.

Damage created by mid-bay skin impacts with the 2″ diameter spherical tip included near-surface fiber crushing and some interply skin delamination. The damage area versus the impact energy for these impacts is shown in figure 120. About half of the impacts were conducted on skins that were stiffened by a single stringer on one side (outboard impacts). This resulted in decreased stiffness of the overall outboard skin; damage from impacts in these regions created less damage than mid-bay skin impacts inboard of stringers two and four. This phenomenon is shown in the plots in figure 120 and can be attributed to slightly different boundary conditions between the impacts.

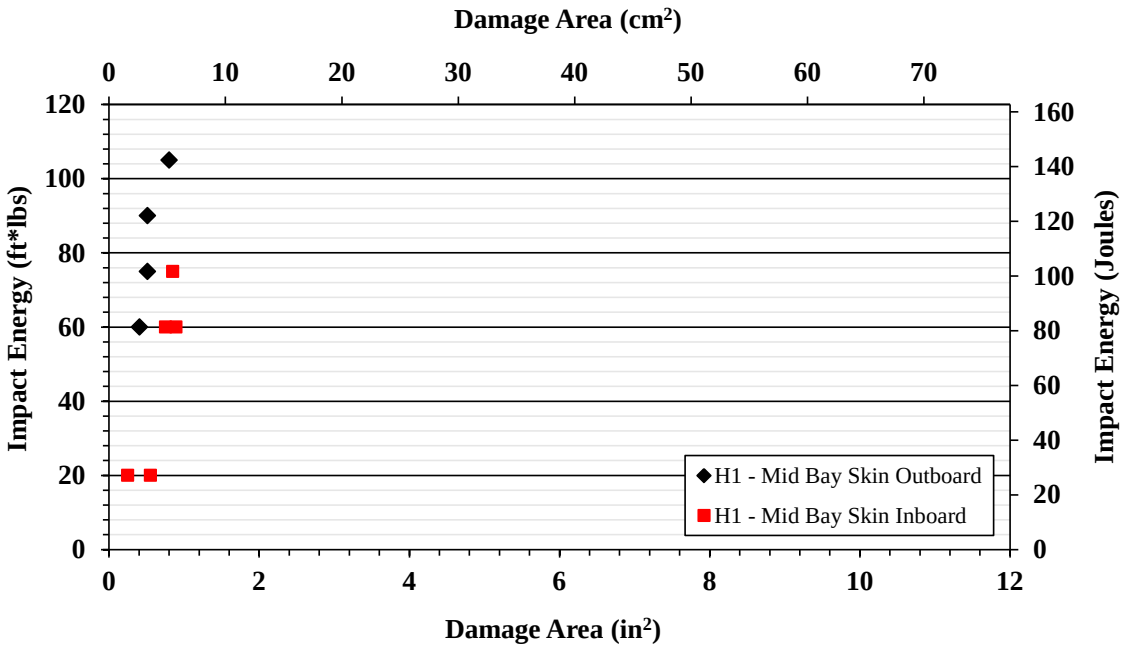

Figure 120. Damage area created by 2″ diameter spherical tip mid-bay skin impacts (type H1)

One way to mitigate the dependency of boundary conditions and plot the impact damage data more consistently would be to plot impact force versus damage area as opposed to impact energy versus damage area. The damage area is more dependent on the impact force than it is on impact energy. For a given impact energy, the force imparted on the structure is dependent on the stiffness at the location being impacted. The higher the stiffness, the higher the force induced. This measurement would be possible by integrating a force transducer onto the tip of the impactor.

The damage area produced by the 2″ diameter, hard spherical impact tip at the three different stringer flange impact locations is shown in figure 121. The plot is not divided into substructure damage and skin delamination damage because, unlike hail impact damage, it was not possible to determine the amount of damage in the skin and substructure separately. Instead, the plot displays the damage area as it relates to each stringer flange impact location (2a, 2b, and 2c). In general, the damage area increases with impact energy. Two obvious deviations from this are the two 2b impacts (red squares) that produced zero damage. This may not actually be the case. These two impacts created very small visual dents, but the C-scan images used to determine damage area did not indicate any damage. This may have been due to a masking effect caused by the stringer flange obscuring the very small level of damage.

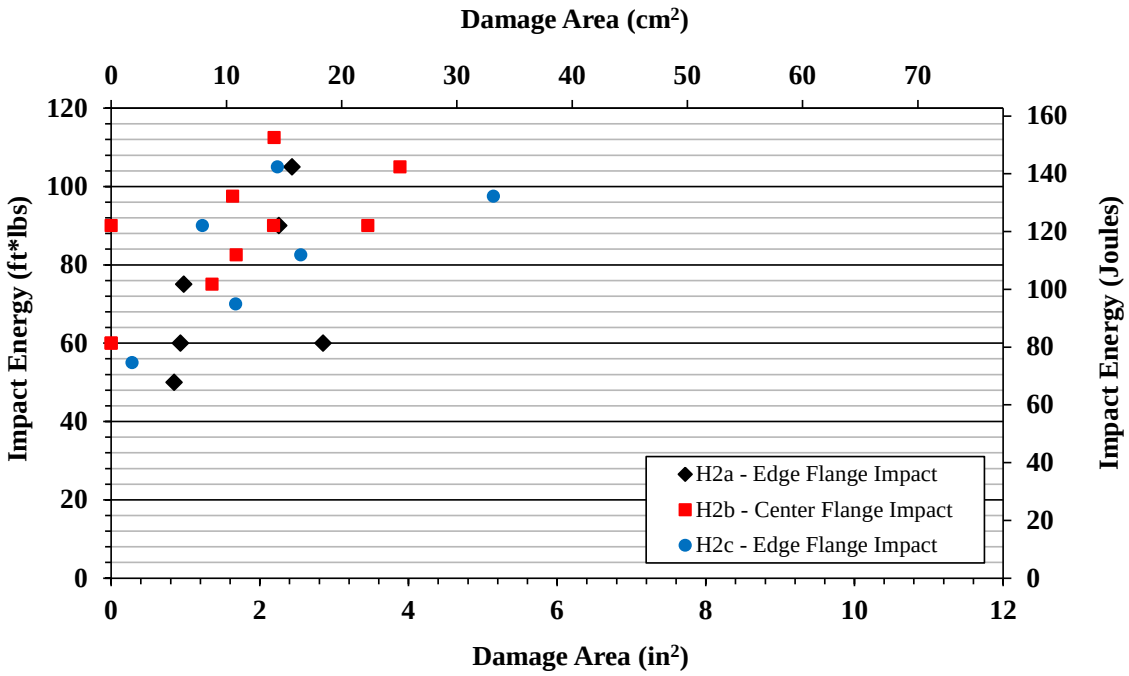

Figure 121. Damage area created by 2″ diameter spherical tip stringer flange impacts (type H2)

Figure 122 plots the mid-stringer impact (between stringer flanges – H3) damage area versus impact energy. These impacts created near-surface fiber crushing and some interply delaminations in the skin. No substructure disbonds were observed as a result of these impacts. This particular impact location had the most consistent boundary conditions and, therefore, resulted in the best trending data.

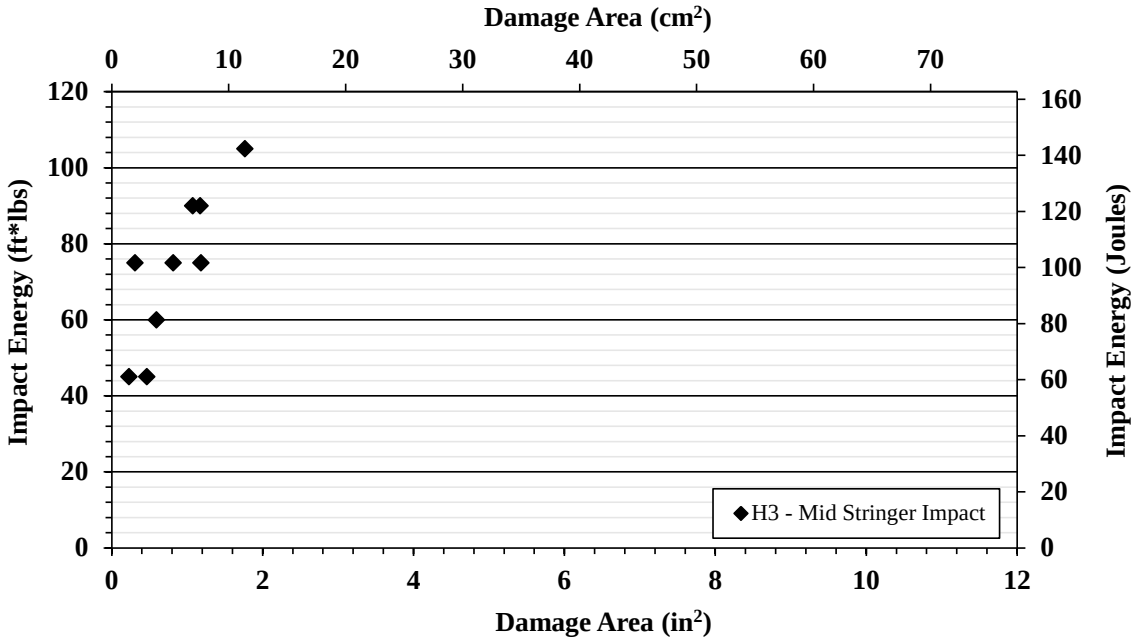

Figure 122. Damage area created by 2″ diameter spherical tip mid-stringer impacts (type H3)

Damage area from the three shear tie impact tests (H4) are displayed in figure 123. The two impacts that created approximately 4 in.^{2} and 10 in.^{2} of damage were located at the edge of the shear tie. The high shear stresses developed during the impact caused the tapered built-up section to delaminate from the skin. The inspection results from the shear tie edge impact and shear tie center impact clearly show the difference in damage level (see impacts 8, 19, and 23 in appendix E).

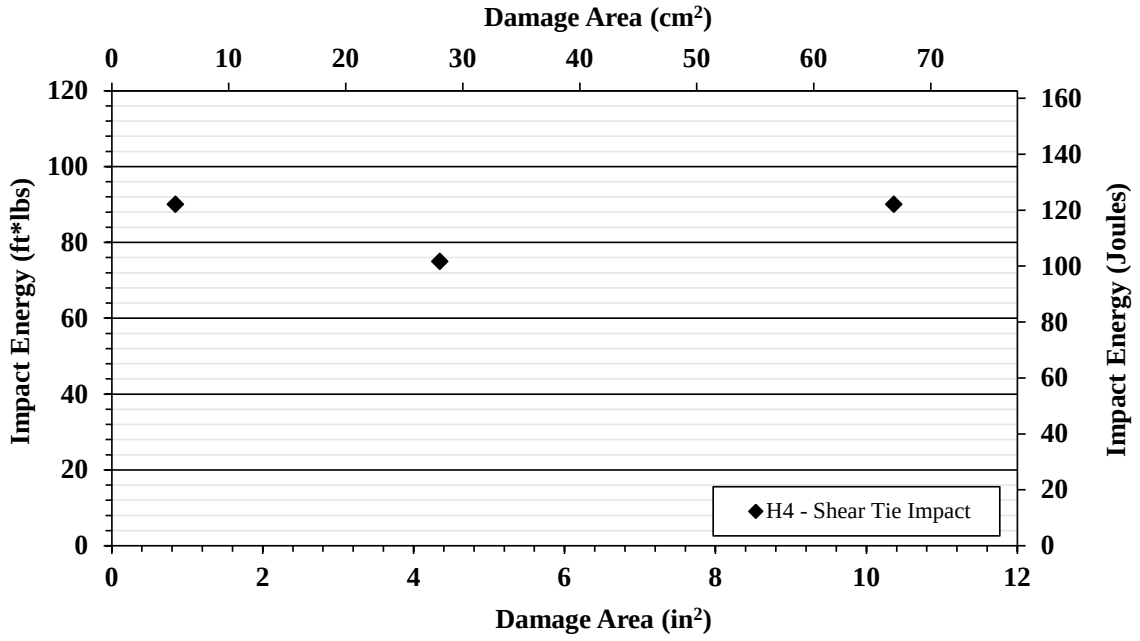

Figure 123. Damage area created by 2″ diameter spherical tip shear tie impacts (type H4)

The UT amplitude C-scan results from the top of bay 1 on panel A are shown on the right side of figure 124. Most of the impact damage is seen as a dark spot on the scan. This is because of the significant decrease in amplitude caused by the near surface fiber crushing. The UT signal does not make it past the first couple of carbon layers and the back wall signal is not detected under the set gate. The blue box in the figure indicates damage that induced an interply delamination in the skin. The red circle indicates a damage area where the near surface fibers were crushed.

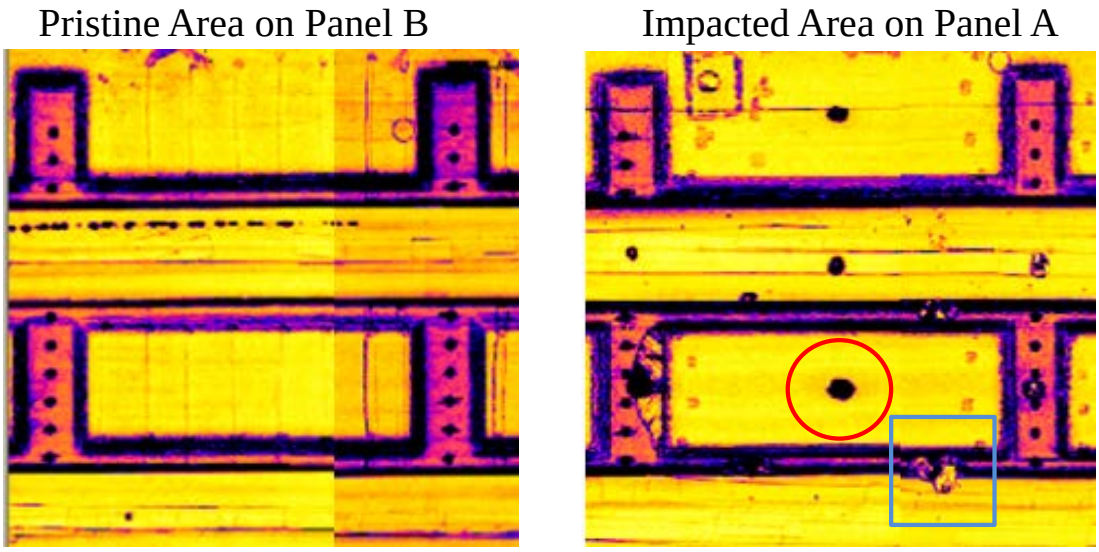

Figure 124. Example of spherical tip impact damage on panel A

It is clear from the NDI results that the damage associated with SHI is much more severe than damage created by the hard, non-crushable impact tip. Although impact energies for the hard impacts were much lower than the simulated hail, higher hardened impact energies would still produce localized damage until penetration of the panel occurred.

5. FUTURE WORK

To better understand the damage initiated using hard, spherical-tip-type impacts, a force transducer could be added to the drop spear impact test setup. Because of the various boundary conditions involved in testing complex, full-scale structures, it is desirable to plot maximum impact force versus the damage area. Further, additional tip diameters and varying tip stiffness (conformable tips) could be studied to determine the effect of impact tip diameter and contact pressure on carbon aircraft fuselage structure. Similarly, low-velocity, hydraulic-actuated blunt impacts simulating ground vehicles bumping the fuselage of an aircraft are of interest. These tests could be performed using protective rubber bumper devices with low velocity and large displacements.

To fully investigate the capabilities of modern NDI technologies, the two panels impact-tested in this study could be used to assess additional NDI techniques. The panels provide a realistic platform for NDI developers to test and validate their NDI technologies.

6. CONCLUSIONS AND RECOMMENDATIONS

Impact damage can occur on aircraft structures from a variety of different objects. They can range from low-velocity, high-mass impacts caused by baggage handling vehicles and dropped equipment during maintenance to high-velocity, lightweight hail impacts and runway debris. Impact damage does not always manifest itself with a surface visible demarcation such as a mar, dent, crack, or scuff. Large interply delamination and substructure disbonding below the level of visual detection can occur as a result of impact damage. Currently, there is no scheduled nondestructive inspection (NDI) required on solid laminates unless an impact is suspected or other unusual environment is encountered. When this occurs, damage assessment must take place through means of NDI to determine if the damage is above or below the allowable damage limit. With increased use of advanced composite materials in commercial transport category aircraft, new technologies for damage detection are emerging. The ability of existing and newer technologies to detect various modes of composite impact damage needs to be assessed on a wide range of damage severity, including detection sensitivity, deployment, and ease of use.

To assess the inspection techniques applied in this study, an impact damage database was assembled for displaying the inspection results obtained from the flat plate panel specimens. Inspection results from each method applied to each panel can be visually compared side-by-side by using the database. Insights into each NDI technique's unique ability to detect and characterize hail impact damage were assessed and discussed in section 4.1.5.

Simulated hail and hard, spherical tip drop weight impact tests were conducted on full-scale carbon fuselage panels. Simulated hail impact (SHI) on the panels at velocities of up to 390 ft. per second (118 m/sec) left little to no surface visual indication of impact or damage, except at direct shear tie impacts. The SHI located at the middle of the bays was capable of inducing extensive interply delamination and subsurface damage with no visual indication from the surface of the panel. Moreover, hail impacts directed at the stringer flange and shear tie induced only substructure disbands, but not interply delaminations, in the 16-ply skin. Particular notes of interest during ice impact testing were:

- When a mid-bay impact occurred, there was no set energy threshold that, when surpassed, initiated substructure delamination away from the impact site. Sometimes it happened, sometimes it did not
- Impacts conducted at locations over stringer flanges initiated damage at lower levels than impacts over unsupported skin impacts
- Higher impact energy was required to initiate damage at the mid-stringer location than at mid-bay and direct stringer flange impacts

Conventional hand-deployed PE-UT inspection methods were used to determine the extent of damage during impact testing. It was shown to be an effective method for locating and characterizing impact damage near the impact area. Substructure damage on stringer flanges away from the impact location was often not detected. This was due to inspections not being far enough away from the impact site to find all of the damage. The additional damage area was subsequently revealed in full-panel, two-dimensional C-scan inspections.

The impact damage created with the 2″ diameter spherical, steel impact tip left localized and often visually detectable damage. A majority of the damage was limited to the 16-ply skin of the panel, but stringer flange and shear tie edge impacts were capable of disbonding substructure. Because of the small size of this damage and its near-surface nature, it was difficult to characterize. Visual dents were observed on almost all of these impacts, even in cases where very little change in UT A-scans was observed. Moreover, damage initiated from these impacts never induced damage away from the impact site.

When the panel impact tests were completed, the MAUS V scanning system was used to inspect each panel with UT and resonance modes. Once the panels had been fully scanned with the MAUS V scanner and the damage accurately mapped out on the panels, additional damage characterization (determination of depth of damage) was accomplished using A-scan signal assessments in combination with C-scan analysis. Information gathered during the post-impact assessment was assembled and entered into an impact database (see appendix D for the ice impacts and appendix E for the hard tip impacts).

It was observed that ultrasonic time of flight (TOF) C-scans and a combination of resonance phase and amplitude C-scans are capable of detecting substructure disbonds with higher sensitivity than ultrasonic amplitude alone. The difference between ultrasonic amplitude and TOF modes was that it was easier to visually observe the differences in color contrast corresponding to substructure disbonds in the TOF C-scan images versus those in the amplitude scans.

With resonance testing, changes to the transducer resonant frequency are caused by defects in the material being inspected or variations in material thickness. These changes in the resonant frequency are subsequently detected as differences in phase and amplitude. Because resonance testing is sensitive to slight changes in material stiffness, small areas where the substructure became disbonded from the skin resulted in detectable changes in the transducer resonant frequency and were reliably detected. This NDI method also accurately detected interply delaminations in the skin.

In addition to the inspections performed, there were four different methods used to deploy FO strain sensing to the two panels. These included 1) embedding the fiber in the skin of the panel, 2) vertically bonding the fiber to the backside of the panel over the skins and stringers, 3) bonding the fiber parallel to the stringers, avoiding the flange-to-skin interface, and 4) bonding the fibers vertically over the backside of the skins only (not over the stringer flanges). Embedding the fiber in the skin must be performed in the factory when the laminate is being laid up. To minimize microbending on the FO, it should be laid parallel to, and on either side of, the carbon material. This could, for example, be done in the mid-plane of a quasi-isotropic layup—and, in the case of the panels used in this study, the -45° direction. Also, a larger diameter FO with a high numerical aperture is desired to minimize microbending. Care needs to be taken not to embed the fiber where fastener holes may be drilled; further, special consideration should be taken to protect the FO when egressing the fiber from the structure. With additional testing, this could prove to be a promising impact-detection method.

When the fiber was continuously bonded to the entire backside of panel B over the stringers and skins, significant fiber breakage occurred at many locations because of stringer flange disbonding.

To detect hard tip impacts, it was determined that avoiding the stringer flange-to-skin transition area prevented the fiber from being sheared when the flange disbonded from the skin. Impact damage generated by the 2″ diameter steel tip left a permanent dent in the panel that was detectable with the FO method in 15 of the 25 interrogated tests. Two critical observations were made when FO was used to detect impact damage: first, the impact damage had to be in close proximity to the FO to transfer strain to the fiber; second, the strain developed in the fiber could not be significantly high, approaching breakage of the fiber. If this did occur, other sections of fiber unrelated to the damage area showed high levels of strain or false detections.

Bonding the FO to the backside of the panel was a time-consuming and tedious operation. A more advanced method of deploying fiber to the surface of the structure needs to be developed to use FO for damage detection on real structures. A possible solution to this would be to embed the FO in the desired pattern in a sheet-type carrier material that bonds to the structure of interest. The material would need to be robust and mechanically protective as well as have a high strain transfer. If the FO were embedded in this pre-manufactured sheet, the exact position of the FO would be known and damage localization could be conducted. Multiple patches could be spliced together, allowing for wide-area damage detection.

7. REFERENCES

1. Dorworth, L.C., Gardiner, G.L., and Mellema, G.M., *Essentials of Advanced Composite Fabricatio and Repair*. Newcastle, Washington: Aviation Supplies & Academics, Inc., 2009.

2. *Polymer Matrix Composites: Guidelines for Characterization of Structural Materials*, Vol. 1, SAE International, 2012.

3. Papakonstantinou, C.G., Balaguru, B., and Lyon, R.E., "Comparative Study of High Temperature Composites,' *Composites Part B: Engineering*, Vol. 32, pp. 637–649, December 2001.

4. *Polymer Matrix Composites: Materials Properties*, Vol. 2, SAE International, 2012.

5. Fuller, L.G., "Production and Characterization of Movel Shaped Fibers for Fluid Sorption and Transport," Clemson University, Clemson, South Carolina, 2009.

6. Eom, S.-Y., Pyo, D.-W., and Ryu, S.-K., "Characterization of Differently Shaped Carbon Fiber Composites Prepared From Naphtha Cracking Bottom Oil," *Korean Journal of Chemical Engineering*, Vol. 27, 2010.

7. Hosur, M.V., Murthy, C.R.L., Ramamurthy, T.S., and Shet, A.,"Estimation of Impact-Induced Damage in CFRR Laminates Through Ultrasonic Imaging," *NDT & E International*, Vol. 31, pp. 359–374, October, 1998.

8. Kolesnikov, B.Y. and Herbeck, L., "Carbon Fiber Composite Airplane Fuselage: Concept and Analysis," ILA International Conference, Berlin, 2004, p. 2.

9. Myxter, J., "American Airlines Cancels 296 More Flights Due to Hail-Damaged Planes," 2012.

10. Johanson, M., "Dallas Tornadoes 2012: DFW Airport Planes Damaged, Hundreds of Fights Canceled," *International Business Times*, 2012.

11. Gringorten, I.I., "Hailstone Extremes for Design," DTIC Document, 1971.

12. Field, P., Hand, W., Cappelluti, G., and McMillan, A., "Hail Threat Standardisation," Research project EASA, Vol. 5, 2008.

13. Aktas, M., Atas, C., Icten, B., and Karakuzu, R., "An Experimental Investigation of the Impact Response of Composite Laminates," *Composite Structures*, Vol. 87, pp. 307–313, 2009.

14. Aymerich, F. and Meili, S., "Ultrasonic Evaluation of Matrix Damage in Impacted Composite Laminates," *Composites Part B: Engineering*, Vol. 31, January, 2000, pp. 1–6.

15. Kim, H., Welch, D.A., and Kedward, K.T., "Experimental Investigation of High Velocity Ice Impacts on Woven Carbon/Epoxy Composite Panels," *Composites Part A: Applied Science and Manufacturing*, Vol. 34, pp. 25–41, January, 2003.

16. Rhymer, J., Kim, H., and Roach, D., "The Damage Resistance of Quasi-Isotropic Carbon/Epoxy Composite Tape Laminates Impacted by High Velocity Ice," *Composites Part A: Applied Science and Manufacturing*, Vol. 43, pp. 1134–1144, July, 2012.

17. FAA Report. (2011). Damage Tolerance and Fatigue Evaluation of Structure, (25.571-1D).

18. Herzberg, I. and Qi, B., "An Engineering Approach for Predicting Residual Strength of Carbon/Epoxy Laminates After Impact and Hygrothermal Cycling," *Composite Structures*, December 1999, pp. 483–490.

19. *Polymer Matrix Composites: Materials Usage, Design and Analysis*, Vol. 3, 2012.

20. Roach, D. and Neidigk, S., "Industry Survey of Structural Health Monitoring Technology and Usage," 2012.

21. Armstrong, K.B. and Barrnett, R.T., *Care and Repair of Advanced Composites*, SAE International, 1998.

22. Roach, D., "Assessing Conventional and Advanced NDI for Composite Aircraft," *High Performance Composites*, Vol. 16, p. 72, 2008.

23. Peters, J.J., Nielsen, Z.A., and Hsu, D.K.,"Comparison of Local Stiffness of Composite Honeycomb Sandwich Structures Measured by Tap Test and Mechanical Test," *AIP Conference Proceedings*, 2001, p. 1031.

24. Roach, D., Rackow, K., and FAA Center, "Improving In-Service Inspection of Composite Structures–It's a Game of CATT and MAUS," U.S. Department of Defense/National Aeronautics and Space Administration/Federal Aviation Administration Aging Aircraft Conference, Georgia, 2003.

25. Malglaive, F. and Albert, R., "Reverse Geometry X-ray Imaging," *Insight-Non-Destructive Testing and Condition Monitoring*, Vol. 51, 2009, pp. 66–68.

26. Schmidt, K.F., Goitia, R.M., Ellingson, W.A., and Green, W., "Correlation of Scanning Microwave Interferometry and Digital X-ray Images for Damage Detection in Ceramic Composite Armor," AIP Conference Proceedings, 2012, p. 1129.

27. Shur, M., "Terahertz Sensing Technology," 2006, p. 27.

28. Davis, W. and Lasser, B., "Real-Time Ultrasonic Imaging Using CCD Camera Techniques," *Nondestructive Characterization of Materials*, pp. 135–140, 2003.

29. Newman, J.W., "Aerospace NDT With Advanced Laser Shearography," 17th World Conference on Nondestructive Testing, pp. 25–28, 2008.

30. Toughiry, M., "Examination of the Nondestructive Evaluation of Composite Gas Cylinders," U.S. Department of Transportation, NTIAC/A7621-18: CRC-CD8, Vol. 1, 2002.

31. Hsu, D.K., Barnard, D.J., Peters, J.J., and Dayal, V., "Physical Basis of Tap Test as a Quantitative Imaging Tool for Composite Structures on Aircraft," AIP Conference Proceedings, p. 1857, 2000.

32. Peters, J., Barnard, D., and Hsu, D., "Development of a Fieldable Air-Coupled Ultrasonic Inspection System," AIP Conference Proceedings, p. 1368, 2004.

33. La Delfa, G., Urso-Miano, V., and Gibson, A., "Characterisation and Modelling of Structural Integrity of Carbon Fibre Wing Box Laminate Subject to Fire," *Plastics, Rubber and Composites,* Vol. 38, pp. 9–10, 2009.

34. Schroeder, J., Ahmed, T., Chaudhry, B., and Shepard, S., "Non-Destructive Testing of Structural Composites and Adhesively Bonded Composite Joints: Pulsed Thermography," *Composites Part A: Applied Science and Manufacturing,* Vol. 33, pp. 1511–1517, 2002.

35. Georgeson, G.E., Hansen, J.M., Kollgaard, J.R., Lea, S.W., and Bopp, J.R., "Damage Detection Device and Method," ed: Google Patents, 2004.

36. Udd, E., Winz, M., and Krege, S., "Failure Mechanisms of Fiber Optic Sensors Placed in Composite Materials," Proceedings of SPIE, pp. 409–416, 2005.

37. Davol, K., Udd, E., Kreger, S., Kunzler, M., and Laylor, M., "Monitoring of Advanced Composite Weave Structures Using Multi-Axis Fiber Grating Strain Sensors," Proceedings of SPIE, p. 128, 2003.

38. Gupta, N., Augustin, M.J., Sathya, S., et al., "Flight Data From an Airworthy Structural Health Monitoring System for an Unmanned Air Vehicle Using Integrally Embedded Fiber Optic Sensors," *Structural Health Monitoring,* Vol. 1, pp. 463–470, 2011.

39. Murayama, H., Igawa, H., Omichi, K., and Machijima, Y., "Distributed Sensing With OFDR and Its Application to Structrual Health Monitoring," SPIE 21st International Conference on Optical Fiber Sensors, 2011.

40. Duncan, R., Childers, B., Gifford, D., Pettit, D., Hickson, A., and Brown, T., "Distributed Sensing Technique for Test Article Damage Detection and Monitoring," SPIE Smart Structures and Materials, 2003.

41. Kreger, S.T., Gifford, D.K., Froggatt, M.E., Soller, B.J., and Wolfe, M.S., "High Resolution Distributed Strain or Temperature Measurements in Single- and Multi-Mode Fiber Using Swept-Wavelength Interferometry," p. ThE42, 2006.

42. Liehr, S., Wendt, M., and Krebber, K., "Distributed Strain Measurements in Perfluoinated Polymer Optical Fibers Using Optical Frequency Domain Reflectometry," *Measurement Science Technology,* Vol. 21, 2009.

43. Scheerer, M., Bockenheimer, C., Dantele, A., et al., "Development and Testing of an Ultrasonic Phased Array System Based on Piezo Actuators and Fiber Optic Sensors," *Structural Health Monitoring*, Landcaster, PA, pp. 447–454, 2011.

44. Saito, N., Yari, T., Nagai, K., and Emomoto, K., "Damage Detection Method for CFRP Bolted Joints Using Embedded BOCDA Optical Fiber Sensor," *Structural Helath Monitoring*, Vol. 1, pp. 455–462, 2011.

45. *Technical Order 33B-1-1: Nondestructive Inspection Methods, Basic Theory*, US Air Force, 2007.

46. Calder, C. and Wilcox, W., "Noncontact Material Testing Using Laser Energy Deposition and Interferometry," *Materials Evaluation*, Vol. 38, pp. 86–91, 1980.

47. Dubois, M., Drake, T.E., and Osterkamp, M.A., "Low-Cost Ultrasonic Inspection of Composites for Aerospace Applications With LaserUT Technology," *Journal of The Japanese Society for Non-Destructive Inspection*, Vol. 57, pp. 11–18, 2008.

48. Fiedler, C., Ducharme, T., and Kwan, J., "The Laser Ultrasonic Inspection System (LUIS) at the Sacramento Air Logistics Center," *Review of Progress in Quantitative Nondestructive Evaluation*, Springer, pp. 515–522, 1997.

49. Thomas, R., Favro, L., Han, X., and Ouyang, Z., "Thermal Methods Used in Composite Inspection," *Comprehensive Composite Materials*, Vol. 5, pp. 427–446, 2000.

50. Favro, L., Han, X., and Thomas, R., "Quantitative Thermal-Wave Measurement of Defects in Composite Aircraft Structures," *Society for the Advancement of Material and Process Engineering, Evolving and Revolutionary Technologies for the New Millenium*, Vol. 44, pp. 845–851, 1999.

51. Distributed Temperature and Strain Measurements," available at http://lunainc.com/products/fiber-sensing-solutions/distributed-temperature-and-strain-measurements.https://lunainc.com/obr4600ts

52. Tong, L. and. Soutis, C., *Recent Advances in Structural Joints and Repairs for Composite Materials*, Elsevier, 2003.